2mi4

THE UNIVERSITY OF KANSAS CENTER FOR RESEARCH, INC.

2385 Irving Hill Rd.— Campus West   Lawrence, Kansas 66044

AN ANALYTICAL INVESTIGATION OF
WING-JET INTERACTION
C. Edward Lan

AN ANALYTICAL INVESTIGATION OF WING-JET INTERACTION

by

C. Edward Lan

CRINC-FRL 74-001

April, 1974

The Flight Research Laboratory
Department of Aerospace Engineering
The University of Kansas
Lawrence, Kansas 66045

TABLE OF CONTENTS

AN ANALYTICAL INVESTIGATION OF WING-JET INTERACTION

by C. Edward Lan

The University of Kansas

SUMMARY

The aerodynamic interaction between the wing and an inviscid jet
with Mach number nonuniformity is formulated by using a two-vortex-
sheet model for the jet. One of the vortex sheets accounts for the
induced jet flow and the other the induced outer flow. No additional
source distribution is needed for the jet at an angle of attack. The
above problem is solved by satisfying the jet and wing tangency and the
jet pressure-continuity conditions and using a "quasi vortex lattice
method" for computing the induced flow field. The latter method is
derived through theoretical consideration by properly accounting for
singularities present in the equations and possesses the same simplicity
and generality as the conventional vortex lattice method but has a better
rate of numerical convergence. The resulting system of algebraic equa-
tions is solved by Purcell's vector method. The numerical formulation
is first applied to the wing-slipstream interaction problem. Results
for one centered-jet configuration are compared with those predicted by
some existing theories. The present method is shown to have the same
accuracy as Rethorst's. Good results have also been obtained in lift,
induced drag and pitching moment coefficients when compared with available
experiments. If the slipstream Mach number is taken to be greater than
the free stream value, the loading is shown to be increased, but the incre-

ment is much less than expected from Prandtl-Glauert transformation applied locally. Explanation is given for this characteristic. The method is finally applied to the upper-surface-blowing STOL configuration. The agreement of the present prediction with measurement by Phelps, et al in lift increment is good. Various characteristics of the aerodynamic interaction have been pointed out and discussed.

1. Introduction

In the design of early subsonic turbojet aircraft, the interference effects of airframe and engines were not regarded as major problems. However, with the advent of high bypass ratio turbofan engines, significant interference effects have been recognized. In fact, the integration of the propulsion system with the airframe has been regarded as one of the major causes which create the discrepancy in the predicted performance with the delivered one. Schumacher and Trent [1] analyzed the performance of some existing fighters and found that the increased engine size is definitely to reduce the cruise efficiency. Attempt has been made recently through wind-tunnel testing with propulsion simulator to identify the complex mechanisms of airframe/engine interference [2,3,4]. Measurements of two-dimensional pressure distributions due to jet effects for the conventional underwing engine installation were made at high subsonic Mach numbers [5]. It was found that the jet affects only the lower surface pressure distribution and that the jet effect can not be adequately simulated by an equivalent solid body. Bagley further suggested that in order to satisfy the ground clearance requirement for large turbofan engines, the engines may be installed above the wing [6]. He found in the experiment on two-dimensional wings with the jet pipe flattened to a rectangular shape near the exit that both lift and lift-dependent drag are increased for the above-wing engine installation. Similar engine

configurations for the purpose of STOL operations have also been tested at NASA Langley Research Center [7]. In these latter engine installations, it is obvious that accounting of the jet interaction becomes a necessity in predicting the wing aerodynamic characteristics.

In general, the jet effects at low speeds may be divided into (1) the entrainment effect with external fluid being sucked into the jet, (2) the displacement effect, the external streamlines being displaced due to the presence of the jet, and (3) the interaction effect, in which the jet flow that is affected by the wing flow field influences in turn the wing flow. No general analytical methods of incorporating these effects in the aerodynamic computation are available. Early analytical or semi-empirical techniques to assess the gross jet effects on the performance of aircraft are discussed in Refs. [8] and [9]. More recently, Mendenhall and his co-workers investigated the STOL wing characteristics with externally-blown jet-augmented flaps [10]. They postulated that the jet effects can be accounted for by a vortex ring distribution on the jet boundary. The jet boundary assumed by them is in fact the boundary at which the longitudinal velocities of the jet and the external stream are equal, as has been defined and used in the turbulent jet theory. The variation of the vortex ring strengths downstream was obtained by assuming that the product of the strength and the ring circumference remains constant. The result was that the conservation of jet momentum was violated. In addition, no interference effect, as defined above, has been included. A more rigorous approach in evaluating the interaction effect was employed by Shollenberger [11 a & b].

The location and strength of flow singularities were determined through iteration. However, the jet was assumed to be inviscid and incompressible. It is not known how important the jet distortion effects are on the wing loading.

Historically, interest in the interaction of two flows with diffenent total energy levels has been centered on the problem of propeller-wing interaction. To gain some insight on the analytical techniques used in this problem, it is appropriate to review some of the developments. Koning [12] explained in great detail in 1935 how the slipstream boundary conditions of flow tangency and pressure continuity can be satisfied by introducing additional flow singularities. Ferrari extended the formulation to the compressible flow through Prandtl-Glauert equation and in the spirit of the classical lifting line theory [13]. Since then, efforts have been directed toward the refinement of the theory by using the Weissinger-type lifting surface method. A main feature of these efforts is the employment of the image technique to find the additional flow singularities necessary to satisfy the slipstream boundary conditions. A representative of this type of work is Rethorst's paper [14] which is concerned with a circular slipstream. Jameson [15] extended Rethorst's method to treat slipstreams of rectangular cross sections. Ribner and Ellis [16] departed from the tradition of the image technique by presenting a formulation applicable to undeflected multi-slipstream configurations by using surface doublet distributions on the slipstreams. Even though the formulation is general enough for lifting-surface type computation,

computer implementation of the general case was not successful. Later,
a "multiple lifting line approximation" was employed [17], in which both
the wing and the slipstream were divided into streamwise segments. In
each segment, a lifting line or lifting ring was placed at the quarter
chord. However, the boundary conditions were satisfied only at the
three-quarter chord of the rearmost segment. The relative values of
the strengths of lifting lines or lifting rings were determined by
matching the upwash. No accurate pressure distribution is obtainable
by their program. Levinsky and others [18] extended the theory of
Ribner and Ellis [16] to the case with deflected slipstreams. They
represented the slipstreams by ring vortices and multipole distribu-
tion on the slipstream axis. The slipstream boundary conditions are
satisfied in the far field in the linearized approximation through the
use of surface distribution of discrete horseshoe vortices. The wing
aerodynamic characteristics were computed by the discrete-type Weissinger's
method. All wing and slipstream trailing vortices were assumed straight
and inclined downward in the extended slipstream direction. No inter-
ference between slipstreams was assumed. Again, the wing pressure
distribution was not predicted. More recently, Kleinstein and Liu [19]
showed that the incorporation of more accurate airfoil data in the
lifting line theory for the wing-propeller interaction is important.
A systematic procedure through the method of matched asymptotic expan-
sions for the interaction of wing and multipropellers was later presented
for high aspect-ratio wings [20].

From the above review of literatures in the propeller-wing interaction, it is clear that the available methods, except Ref.[11b], are not adequate for predicting the wing pressure distribution and the spanwise induced drag distribution for arbitrary planforms without restrictions on aspect ratios and sweep angles. In addition, no method to account for the differences in the jet and external Mach numbers seems available. In the present investigation, the following improvements over the existing techniques will be made: (1) A quasi vortex lattice model for the wing will be used. This is a quasi continuous vortex model and represents an improvement over the conventional vortex lattice method. The wing pressure distribution and the spanwise induced drag distribution can be computed for arbitrary wing planforms. (2) The differences in the jet and external Mach numbers are accounted for through the use of two vortex sheets on the jet boundary. (3) The jet surface boundary conditions are satisfied everywhere on the jet surface, not just in the wing region as done in Ref.[17]. The restrictions are: (1) The boundary conditions are satisfied only in the linearized approximation. Thus, the jet boundary conditions are satisfied on the jet surface and the tangency and pressure conditions are linearized. (2) The wing thickness is not included. (3) The Prandtl-Glauert equation is used.

2. List of Symbols

$\vec{a}$ = $(x_1-x)\hat{i} + (y_1-y)\hat{j} + (z_1-z)\hat{k}$, m(ft)

$\vec{a}'$ = $(x_1-x)\hat{i} + \beta(y_1-y)\hat{j} + \beta(z_1-z)\hat{k}$, m(ft)

A aspect ratio

A_j jet cross-sectional area, $m^2(ft^2)$

b span, m(ft)

$\vec{b}$ = $(x_2-x)\hat{i} + (y_2-y)\hat{j} + (z_2-z)\hat{k}$, m(ft)

$\vec{b}'$ = $(x_2-x)\hat{i} + \beta(y_2-y)\hat{j} + \beta(z_2-z)\hat{k}$, m(ft)

c local chord length, m(ft)

$\bar{c}$ reference chord length, m(ft)

C leading edge suction parameter. See Eqs. (4.25), (4.26)

c_{di} sectional induced drag coefficient

C_{Di} total induced drag coefficient

C_{Dr} drag coefficient due to Coanda effect

c_{ℓ} sectional lift coefficient

$\bar{c}_{\ell}$ sectional lift coefficient based on average dynamic pressure; is equal to $2\,c_{\ell}\mu^2/(1 + \mu^2)$

C_L total lift coefficient

C_{Lr} lift coefficient due to Coanda effect

c_m sectional pitching moment coefficient about the y-axis

C_m total pitching moment coefficient about the y-axis

C_p pressure coefficient

c_t sectional leading-edge thrust coefficient

C_T total leading-edge thrust; or propeller thrust coefficient equal to thrust divided by the disc area and the free stream dynamic pressure

C_μ jet thrust coefficient, $T_r/q_o S$

D   diameter of slipstream

D_r drag due to Coanda effect, N(lb)

$\hat{e}$ unit tangential vector

$\vec{G}_\ell$ a vector defined by Eq. (4.34)

h   distance of the jet lower surface to the wing surface, m(ft)

J   propeller advance ratio

$\vec{\ell}$ $= (x_2-x_1)\hat{i} + (y_2-y_1)\hat{j} + (z_2-z_1)\hat{k}$, m(ft)

$\vec{\ell}'$ $= (x_2-x_1)i + \beta(y_2-y_1)j + \beta(z_2-z_1)k$, m(ft)

L   total lift, N(lb)

L_r lift due to Coanda effect, N(lb)

M   Mach number

$\vec{M}_\ell$ a vector defined by Eq. (4.33)

$\hat{n}$ unit normal vector

[N]   normal velocity influence coefficient matrix

N   number of chordwise integration points

p   static pressure, N/m^2 (lb/ft^2)

$\vec{q}$ induced velocity vector, m/sec (ft/sec)

q   dynamic pressure, N/m^2 (lb/ft^2)

$\vec{R}$ $= x\hat{i} + y\hat{j} + z\hat{k}$, m(ft)

R_β^2 $= (x-x')^2 + \beta^2(y-y')^2 + \beta^2(z-z')^2$, m^2(ft)

R_j radius of slipstream, m(ft)

s   streamwise coordinate, m(ft)

[S]   tangential velocity influence coefficient matrix

S_w,S   wing area, $m^2 (ft^2)$

T $= \rho_o/\rho_j$

T_c propeller thrust coefficient based on q_s. See Eq. (5.12)

T_r jet thrust, N(lb)

t, t_j jet thickness, m(ft)

$\vec{U}$ free stream velocity vector, m/sec (ft/sec)

u nondimensional perturbed velocity in the x- direction

$\vec{V}$ unperturbed velocity vector, m/sec (ft/sec)

v perturbed velocity vector, m/sec (ft/sec)

V_θ slipstream rotational velocity, m/sec (ft/sec)

w nondimensional perturbed velocity in the z- direction

x, y, z wing-fixed rectangular coordinates with positive x- axis along the axis of symmetry pointing downstream, positive y-axis pointing to the right and positive z- axis pointing upward, m(ft)

$z_c(x)$ camber, m(ft)

α angle of attack, deg.

$\beta \;=\; (1-M^2)^{\frac{1}{2}}$

δ_{12}, δ_{21} diffraction coefficient. See Appendix B

δ_f flap deflection, deg

γ nondimensional vortex density

Γ discrete vortex strength

ξ nondimensional streamwise coordinate. See Eq. (4.36)

$\lambda_{12}, \lambda_{21}$ reflection coefficient. See Appendix B

Λ sweep angle, deg

$\mu \;=\; V_o/V_s$ or V_o/V_j

$\mu' \;=\; (\vec{U} \cdot \hat{e}_s)/(\vec{V}_s \cdot \hat{e}_s)$

ϕ dimensional perturbation velocity potential, m^2/sec (ft^2/sec)

$\bar{\phi}$ nondimensional perturbation velocity potential. See Eqs. (4.1), (4.2)

ρ density, kg/m^3 ($slugs/ft^3$)

ψ nondimensional additional perturbation velocity potential. See Eqs. (4.8), (4.9)

σ Brenckmann's slipstream strength parameter equal to $2\bar{T}_c$

θ angular coordinate. See Eq. (4.36)

Subscripts

1   first endpoint of a vortex element

2   second endpoint of a vortex element

a   additional

cp   center of pressure

j   jet flow

ℓ leading edge

t   trailing edge

o   outer flow

s   slipstream or jet region

st   strip theory

w   wing

3. Boundary Conditions

The base flow, or the flow field before the wing is introduced,
includes in general the uniform free stream, the jet flow and the jet
entrained flow due to turbulent mixing. In order to simplify the
analysis, the jet entrained flow will be ignored in the present analysis.
As the wing is introduced into the base flow, perturbations of the flow
field occur. The calculation of these perturbations represent one
of the main objectives in the present investigation.

The perturbed flow field must be calculated by satisfying the
boundary conditions. The boundary conditions on the jet surface
require that the surface be a stream surface and the pressure there
be continuous. The stream surface condition is satisfied if the
slopes of streamlines on both sides of the jet surface are the same,
i.e.

$$\frac{\hat{n} \cdot (\vec{U} + \vec{v}_o)}{\hat{e}_s \cdot (\vec{U} + \vec{v}_o)} = \frac{\hat{n} \cdot (\vec{V}_s + \vec{v}_j)}{\hat{e}_s \cdot (\vec{V}_s + \vec{v}_j)} \qquad (3.1)$$

where $\hat{e}_s$ is a unit vector tangent to the jet path axis and $\hat{n}$ is a
unit normal vector at the boundary of the jet cross section normal
to the jet path. See Figure 3.1. $\vec{U}$ is the freestream vector. $\vec{V}_s$
is the jet flow velocity vector and $\vec{v}_o$ and $\vec{v}_j$ are the perturbed velo-
cities outside and inside the jet, respectively.
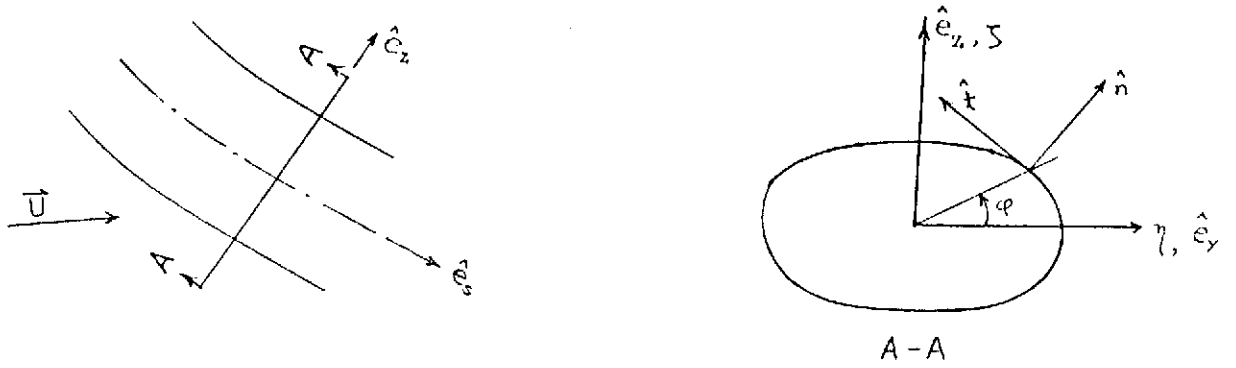
Figure (3.1) Definition of Jet Coordinate System

The pressure continuity condition can be found by using the

Bernoulli's equation:

$$\frac{a^2}{\gamma-1} + \frac{1}{2}|\vec{U}_T|^2 = \frac{a_{ref}^2}{\gamma-1} + \frac{1}{2}|\vec{V}_{ref}|^2 \tag{3.2}$$

Using the isentropic condition:

$$a^2 = \frac{\gamma p}{\rho} = a_{ref}^2 \left(\frac{p}{p_{ref}}\right)^{\frac{\gamma-1}{\gamma}} \tag{3.3}$$

Eq. (3.2) can be reduced to

$$\left(\frac{p}{p_{ref}}\right)^{\frac{\gamma-1}{\gamma}} = 1 + \frac{\gamma-1}{2}\frac{1}{a_{ref}^2}\left[|\vec{V}_{ref}|^2 - |\vec{U}_T|^2\right]$$

or,

$$p = p_{ref}\left\{1 + \frac{\gamma-1}{2}\frac{1}{a_{ref}^2}\left[|\vec{V}_{ref}|^2 - |\vec{U}_T|^2\right]\right\}^{\frac{\gamma}{\gamma-1}} \tag{3.4}$$

For the outer flow, let $p_{ref} = p_o$, the pressure of the outer flow at

the jet exit and $\vec{V}_{ref} = \vec{U}$. Then $\vec{U}_T = \vec{U} + \vec{v}_o$. For the jet flow, let

$p_{ref} = p_j$, the jet pressure at the jet exit, and $\vec{V}_{ref} = \vec{V}_s$, $\vec{U}_T = \vec{V}_s + \vec{v}_j$

Since $p_o = p_j$, the continuity of the static pressure on the jet surface

implies that

$$\left\{1 + \frac{\gamma_j-1}{2}\frac{\rho_j}{\gamma_j p_j}\left[|\vec{V}_s|^2 - |\vec{V}_s + \vec{v}_j|^2\right]\right\}^{\frac{\gamma_j}{\gamma_j-1}} =$$
$$\left\{1 + \frac{\gamma-1}{2}\frac{\rho_o}{\gamma p_o}\left[|\vec{U}|^2 - |\vec{U} + \vec{v}_o|^2\right]\right\}^{\frac{\gamma}{\gamma-1}} \tag{3.5}$$

If it is further assumed that $\gamma = \gamma_j$, Eq. (3.5) can be reduced to

$$\rho_j\left[|\vec{V}_s|^2 - |\vec{V}_s + \vec{v}_j|^2\right] = \rho_o\left[|\vec{U}|^2 - |\vec{U} + \vec{v}_o|^2\right]$$

or,

$$\rho_j\left[\vec{V}_s - (\vec{V}_s + \vec{v}_j)\right]\cdot\left[\vec{V}_s + (\vec{V}_s + \vec{v}_j)\right] =$$
$$\rho_o\left[\vec{U} - (\vec{U} + \vec{v}_o)\right]\cdot\left[\vec{U} + (\vec{U} + \vec{v}_o)\right] \tag{3.6}$$

Since the velocity difference across the surface can be represented

by a vorticity distribution having the strength equal to the magnitude

of the velocity difference and a direction normal to the velocity dif-

ference, Eq. (3.6) can be interpreted as the continuity of Joukowsky

force across the jet surface. Eq. (3.6) can also be recast to the

following form:

$$\varsigma_j \left[\vec{V_s} + \frac{\vec{v_j}}{2} \right] \cdot \vec{v_j} = \varsigma_o \left[\vec{U} + \frac{\vec{v_o}}{2} \right] \cdot \vec{v_o} \qquad (3.7)$$

To simplify Eqs. (3.1)   and (3.7) , let

$$\vec{v_j} = (\vec{U} \cdot \hat{e}_z)\hat{e}_z + \nabla \phi_s \qquad (3.8)$$

$$\vec{v_o} = \nabla \phi_o \qquad (3.9)$$

Substitution of these relations into Eq. (3.1)   gives

$$[\vec{U} \cdot \hat{n} + \nabla \phi_o \cdot \hat{n}][\vec{V_s} \cdot \hat{e}_s + \hat{e}_s \cdot \nabla \phi_s] =$$
$$[\vec{U} \cdot \hat{e}_s + \hat{e}_s \cdot \nabla \phi_o][\vec{V_s} \cdot \hat{n} + (\vec{U} \cdot \hat{e}_z)(\hat{e}_z \cdot \hat{n}) + \hat{n} \cdot \nabla \phi_s]$$

For the purpose of linearizing the last equation, it is assumed that

$$\hat{e}_s \cdot \nabla \phi_s \ll \vec{V_s} \cdot \hat{e}_s \qquad (3.10)$$

$$\hat{e}_s \cdot \nabla \phi_o \ll \vec{U} \cdot \hat{e}_s \qquad (3.11)$$

It follows that

$$(\vec{V_s} \cdot \hat{e}_s)(\vec{U} \cdot \hat{n}) - (\vec{U} \cdot \hat{e}_s)[\vec{V_s} \cdot \hat{n} + (\vec{U} \cdot \hat{e}_z)(\hat{n} \cdot \hat{e}_z)] + (\vec{V_s} \cdot \hat{e}_s)(\hat{n} \cdot \nabla \phi_o)$$
$$\cong (\vec{U} \cdot \hat{e}_s)(\hat{n} \cdot \nabla \phi_s) \qquad (3.12)$$

Let

$$\mu' = \frac{\vec{U} \cdot \hat{e}_s}{\vec{V_s} \cdot \hat{e}_s} \qquad (3.13)$$

Then

$$\vec{U} \cdot \hat{n} (1 - \mu') - \mu' \vec{V_s} \cdot \hat{n} + \frac{\partial \phi_o}{\partial n} \cong \mu' \frac{\partial \phi_s}{\partial n} \qquad (3.14)$$

where $(\vec{U} \cdot \hat{e}_z)(\hat{n} \cdot \hat{e}_z) = \vec{U} \cdot \hat{n}$ has been used. Eq. (3.14)   is exactly the

same as Eq. (8) of Ref. (18), Part I, if $\vec{V_s} \cdot \hat{n} = 0$.

Similarly, Eq. (3.7)   can be written

$$\varsigma_j \left[\vec{V_s} + \frac{1}{2}(\vec{U} \cdot \hat{e}_z)\hat{e}_z + \frac{1}{2} \nabla \phi_s \right] \cdot \left[(\vec{U} \cdot \hat{e}_z)\hat{e}_z + \nabla \phi_s \right] =$$
$$\varsigma_o \left[\vec{U} + \frac{1}{2} \nabla \phi_o \right] \cdot \nabla \phi_o$$

or,

$$\varsigma_j \left[(\vec{U} \cdot \hat{e}_z)(\vec{V_s} \cdot \hat{e}_z) + \frac{1}{2}(\vec{U} \cdot \hat{e}_z)^2 + (\vec{U} \cdot \hat{e}_z)\nabla \phi_s \cdot \hat{e}_z + \vec{V_s} \cdot \nabla \phi_s \right] \cong$$
$$\varsigma_o (\vec{U} \cdot \nabla \phi_o)$$

Noting that $\vec{V}_s \cdot \nabla \phi_s = (\vec{V}_s \cdot \hat{e}_s) \hat{e}_s \cdot \nabla \phi_s + (\vec{V}_s \cdot \hat{n}) \hat{n} \cdot \nabla \phi_s$, etc., it is found that

$$\mathcal{S}_j (\vec{V}_s \cdot \hat{e}_s) \frac{\partial \phi_s}{\partial s} + \mathcal{S}_j (\vec{V}_s \cdot \hat{n}) \frac{\partial \phi_s}{\partial n} \cong \mathcal{S}_\circ (\vec{U} \cdot \hat{e}_s) \frac{\partial \phi_\circ}{\partial s} + \mathcal{S}_\circ (\vec{U} \cdot \hat{n}) \frac{\partial \phi_\circ}{\partial n} -$$

$$\mathcal{S}_j \left[(\vec{U} \cdot \hat{e}_z)(\vec{V}_s \cdot \hat{e}_z) + \frac{1}{2}(\vec{U} \cdot \hat{e}_z)^2 + (\vec{U} \cdot \hat{e}_z) \nabla \phi_s \cdot \hat{e}_z \right] \qquad (3.15)$$

For small jet deflections, $\vec{U} \cdot \hat{e}_z$, $\vec{U} \cdot \hat{n}$, $\vec{V}_s \cdot \hat{e}_z$ and $\vec{V}_s \cdot \hat{n}$ may be assumed to be of the same order as the perturbations. In this special case, Eq.(3.15) can be simplified to

$$\mathcal{S}_j (\vec{V}_s \cdot \hat{e}_s) \frac{\partial \phi_s}{\partial s} \cong \mathcal{S}_c (\vec{U} \cdot \hat{e}_s) \frac{\partial \phi_c}{\partial s} \qquad (3.16)$$

The wing boundary conditions will now be considered. Assume that the wing surface can be described by the following relation:

$$h(x, y, z) = z_c - f(x, y) \qquad = 0 \qquad (3.17)$$

The unit normal vector is then

$$\hat{n}_w = \frac{\nabla h}{|\nabla h|} = \frac{-\frac{\partial f}{\partial x} \hat{i} - \frac{\partial f}{\partial y} \hat{j} + \hat{k}}{|\nabla h|} \qquad (3.18)$$

The tangency condition requires that

$$\vec{U}_T \cdot \hat{n}_w = 0 \qquad (3.19)$$

If the wing is not immersed in the jet, Eq.(3.19) can be written

$$(\vec{U} + \vec{v}_\circ) \cdot \left(-\frac{\partial f}{\partial x} \hat{i} - \frac{\partial f}{\partial y} \hat{j} + \hat{k} \right) = 0$$

Since both $\vec{U} \cdot \hat{j}\, \partial f / \partial y$ and $\vec{v}_e \cdot \hat{j}\, \partial f / \partial y$ are small, they may be neglected. Keeping only the first-order terms, it is found that

$$\frac{\partial \phi_o}{\partial z} = (\vec{U} \cdot \hat{i})\frac{\partial f}{\partial x} - \vec{U} \cdot \hat{k}$$

$$= (\vec{U} \cdot \hat{i})\frac{\partial z_c}{\partial x} - \vec{U} \cdot \hat{k} \qquad \text{(outside the jet)} . \qquad (3.20)$$

If the wing is inside the jet, the boundary condition Eq.(3.19) becomes

$$(\vec{V}_s + \vec{v}_j) \cdot \left(-\frac{\partial f}{\partial x}\hat{i} - \frac{\partial f}{\partial y}\hat{j} + \hat{k} \right) = 0 .$$

From Eq.(3.8), it can be shown that

$$\left[\vec{V}_s + (\vec{U} \cdot \hat{e}_z)\hat{e}_z + \nabla \phi_s \right] \cdot \left(-\frac{\partial f}{\partial x}\hat{i} - \frac{\partial f}{\partial y}\hat{j} + \hat{k} \right) = 0 .$$

Or, approximately,

$$\frac{\partial \phi_s}{\partial z} = (\vec{V}_s \cdot \hat{i})\frac{\partial f}{\partial x} - \vec{U} \cdot \hat{e}_z (\hat{e}_z \cdot \hat{k}) - \vec{V}_s \cdot \hat{k}$$

$$= (\vec{V}_s \cdot \hat{i})\frac{\partial z_c}{\partial x} - \vec{U} \cdot \hat{e}_z (\hat{e}_z \cdot \hat{k}) - \vec{V}_s \cdot \hat{k} \qquad (3.21)$$
$$\text{(inside the jet)}$$

4. Method of Flow Singularities

Due to the presence of the wing, disturbances are created not only in the external flow, but also in the jet flow, which in turn affect the wing flow. Employing the technical terms associated with wave propagation, the interaction may be explained as the reflection and diffraction at the jet surface of the wing disturbances. The reflected disturbances in turn influence the wing flow and the diffracted ones perturb the jet flow. This principle is explained in more detail and applied to a two-dimensional idealized case in Appendix B. It is found in Appendix B that reflected disturbances account for most of the effects of wing-jet interaction for moderate or large jet thickness. In general, it may be stated that reflection of disturbances from the jet surface into the jet region will decrease the loading of that region from the uniform-flow value at the corresponding jet velocity. The contrary is true for the outer flow region. For the three-dimensional case with different Mach numbers inside and outside the jet, quantitative prediction of these additional disturbances may be found by introducing two sheets of jet surface vortices, one being applicable in the outer region with M_0 and one applicable in the jet region with M_j, in such a way that boundary conditions Eqs.(3.14) and (3.16) are satisfied. The latter can be done in accordance with Koning's method of introducing additional singularities.

It is convenient to introduce nondimensional perturbation potentials $\bar{\phi}_o$ and $\bar{\phi}_s$ such that

$$\phi_o = (\vec{U} \cdot \hat{e}_s)\, \bar{\phi}_o \qquad (4.1)$$

$$\phi_s = (\vec{V}_s \cdot \hat{e}_s)\, \bar{\phi}_s \qquad (4.2)$$

Eqs.(3.14), (3.16), (3.20) and (3.21) become

$$\frac{\partial \bar{\phi}_s}{\partial n} = \frac{\partial \bar{\phi}_o}{\partial n} + \frac{\bar{\phi}_o}{\vec{U} \cdot \hat{e}_s}\frac{\partial (\vec{U} \cdot \hat{e}_s)}{\partial n} + \frac{\vec{U} \cdot \hat{n}\,(1-\mu')}{\vec{U} \cdot \hat{e}_s} \qquad (4.3)$$

$$\frac{\partial \bar{\phi}_s}{\partial s} = T(\mu')^2\frac{\partial \bar{\phi}_o}{\partial s} + T\mu'\bar{\phi}_o\frac{1}{\vec{V}_s \cdot \hat{e}_s}\frac{\partial}{\partial s}(\vec{U} \cdot \hat{e}_s) \qquad (4.4)$$

$$\frac{\partial \bar{\phi}_o}{\partial z} = \frac{\vec{U} \cdot \hat{i}}{\vec{U} \cdot \hat{e}_s}\frac{\partial z_c}{\partial x} - \frac{\vec{U} \cdot \hat{k}}{\vec{U} \cdot \hat{e}_s} \qquad \text{(on wing surface)} \qquad (4.5)$$

$$\frac{\partial \bar{\phi}_s}{\partial z} = \frac{\vec{V}_s \cdot \hat{i}}{\vec{V}_s \cdot \hat{e}_s}\frac{\partial z_c}{\partial x} - \frac{(\vec{U} \cdot \hat{e}_z)(\hat{e}_z \cdot \hat{k})}{\vec{V}_s \cdot \hat{e}_s} - \frac{\vec{V}_s \cdot \hat{k}}{\vec{V}_s \cdot \hat{e}_s} \qquad (4.6)$$
$$\text{(on wing surface)}$$

where
$$T = S_c / S_j \qquad (4.7)$$

In both Eqs.(4.3) and (4.4), it has been assumed that $\vec{V}_s \cdot \hat{e}_s$ is constant and $\vec{V}_s \cdot \hat{n} = 0$. If it is further assumed that $\partial(\vec{U} \cdot \hat{e}_s)/\partial n$ and $\partial(\vec{U} \cdot \hat{e}_s)/\partial s$ are small so that the corresponding terms are of the second order, then Eqs.(4.3) and (4.4) can be simplified to be

$$\frac{\partial \bar{\phi}_s}{\partial n} = \frac{\partial \bar{\phi}_o}{\partial n} + \frac{\vec{U} \cdot \hat{n}\,(1-\mu')}{\vec{U} \cdot \hat{e}_s} \qquad (4.3a)$$

$$\frac{\partial \bar{\phi}_s}{\partial s} = T(\mu')^2\frac{\partial \bar{\phi}_o}{\partial s} \qquad (4.4a)$$

Let $\phi_{wo}(M_o)$ and $\phi_{ws}(M_j)$ be the nondimensional potential functions for the wing alone cases in the uniform flow with the corresponding Mach

numbers of the outer flow and the jet flow, respectively. Let

$$\bar{\phi}_o = \phi_{wo}(M_o) + \psi_o(M_o) \tag{4.8}$$

$$\bar{\phi}_s = \phi_{ws}(M_j) + \psi_s(M_j) \tag{4.9}$$

It follows that ψ_u and ψ_s are the additional perturbation potentials

for regions outside and inside the jet, respectively. Using Eqs.(4.8)

and (4.9), the above boundary conditions become

On jet surface
$$\frac{\partial \psi_s}{\partial n} - \frac{\partial \psi_u}{\partial n} = - \frac{\partial \phi_{ws}}{\partial n}(M_j) + \frac{\partial \phi_{wo}}{\partial n}(M_o) + \frac{\vec{U} \cdot \hat{n}(1 - \mu')}{\vec{U} \cdot \hat{e}_s} \tag{4.10}$$

$$\frac{\partial \psi_s}{\partial s} - T(\mu')^2 \frac{\partial \psi_u}{\partial s} = - \frac{\partial \phi_{ws}}{\partial s}(M_j) + T(\mu')^2 \frac{\partial \phi_{wo}}{\partial s}(M_o) \tag{4.11}$$

On wing surface
$$\frac{\partial \psi_u}{\partial z} = \frac{\vec{U} \cdot \hat{i}}{\vec{U} \cdot \hat{e}_s} \frac{\partial z_c}{\partial x} - \frac{\vec{U} \cdot \hat{k}}{\vec{U} \cdot \hat{e}_s} - \frac{\partial \phi_{wo}}{\partial z} \tag{4.12}$$

$$\frac{\partial \psi_s}{\partial z} = \frac{\vec{V}_s \cdot \hat{i}}{\vec{V}_s \cdot \hat{e}_s} \frac{\partial z_c}{\partial x} - \frac{(\vec{U} \cdot \hat{e}_z)(\hat{e}_z \cdot \hat{k})}{\vec{V}_s \cdot \hat{e}_s} - \frac{\vec{V}_s \cdot \hat{k}}{\vec{V}_s \cdot \hat{e}_s} - \frac{\partial \phi_{ws}}{\partial z} \tag{4.13}$$

In applications, Eqs.(4.10)-(4.13) can be reduced to different forms

for different problems.

At this point, a two-vortex-sheet model for the jet surface will

be introduced. The reasons for introducing two vortex sheets, instead

of one, are discussed below.

(1) If Ribner's formulation [16] was followed, a single vortex

sheet and a source sheet would have been introduced to account for

the jumps in tangential velocities Eq.(4.11) and in normal velocities

Eq.(4.10), respectively. However, theoretically, these flow singulari-

ties should be associated with the mean flow field which depends on

the unknown flow singularities. Thus, additional linearization as-
sumption must be made to the effect that the mean flow field can be
approximated by the unperturbed one. Furthermore, an additional
different type of integral for the source distribution must be handled.
The main advantage of Ribner's formulation is that the number of equa-
tions can be reduced by one. On the other hand, the present formu-
lation will solve the problem defined in Eqs.(4.10)-(4.13) without
additional linearization assumption. Besides, no source integral has
to be introduced, because the jet and the outer perturbed flow fields
will be solved separately by using the vortex distribution and the
solutions matched according to Eqs.(4.10) and (4.11) at the jet surface.
This is the same technique used by Rethorst [14]. The disadvantage
is that the number of unknowns to be determined would be increased.
This disadvantage can be minimized by using an efficient technique for
solving the simultaneous equations (4.10)-(4.13), to be discussed
later in this section.

(2) If $M_o \neq M_j$, then no existing methods are applicable. It is
because if a flow singularity is introduced at a certain position on
the jet surface, it will induce different normal and tangential velo-
cities at all other points on the jet surface as they are approached
from inside and outside the jet region. Therefore, the source and vor-
tex distributions are interdependent. The number of unknowns can not
be reduced. In this case, the present formulation is advantageous,
because it is not necessary to introduce the source distribution.

The present method can also be extended to the case where $M_j > 1$ and $M_0 < 1$.

Now define $[S_{JW}]$ as the s-influence matrix for the jet due to the wing, i.e., the matrix elements being the s-perturbed velocities on the jet due to unit vortex distribution on the wing. Similar definitions are applicable to the matrices $[N_{JW}]$, $[N_{WW}]$, $[N_{WJ}]$, etc. where N denotes the normal components. Using "γ" with appropriate subscripts to denote the unknown vortex strength, additional perturbed velocities on the jet surface can be written as

$$\left\{\frac{\partial \psi_o}{\partial n}\right\} = \left[N_{JW}^{(o)}\right]\left\{\gamma_{wa}^{(o)}\right\} + \left[N_{JJ}^{(o)}\right]\left\{\gamma_{oj}\right\} \tag{4.14}$$

$$\left\{\frac{\partial \psi_s}{\partial n}\right\} = \left[N_{JW}^{(j)}\right]\left\{\gamma_{wa}^{(j)}\right\} + \left[N_{JJ}^{(j)}\right]\left\{\gamma_{jj}\right\} \tag{4.15}$$

$$\left\{\frac{\partial \psi_o}{\partial s}\right\} = \left[S_{JW}^{(o)}\right]\left\{\gamma_{wa}^{(o)}\right\} + \left[S_{JJ}^{(o)}\right]\left\{\gamma_{oj}\right\} \tag{4.16}$$

$$\left\{\frac{\partial \psi_s}{\partial s}\right\} = \left[S_{JW}^{(j)}\right]\left\{\gamma_{wa}^{(j)}\right\} + \left[S_{JJ}^{(j)}\right]\left\{\gamma_{jj}\right\} \tag{4.17}$$

where the subscripts and superscripts "o" and "j" denote, respectively, the outer and the jet regions. $\gamma_{wa}^{(o)}$ and $\gamma_{wa}^{(j)}$ are the additional wing vortex strengths on the wing surface outside and inside the jet, respectively. γ_{oj} and γ_{jj} are the vortex strengths on the jet surface for the outer flow and the jet flow, respectively. In Eqs. (4.12) and (4.13), $\partial \psi_o / \partial z$ and $\partial \psi_s / \partial z$ can be expressed as special forms of Eqs. (4.14) and (4.15).

If Eqs.(4.14)-(4.17) are introduced into Eqs.(4.10)-(4.13),

these latter equations become

On jet surface

$$
[N_{Jw}^{(i)}]\{\gamma_{wa}^{(i)}\} - [N_{Jw}^{(o)}]\{\gamma_{wa}^{(o)}\} + [N_{JJ}^{(i)}]\{\gamma_{jj}\} - [N_{JJ}^{(o)}]\{\gamma_{oj}\} =
$$

$$
\left\{ - \frac{\partial\phi_{ws}}{\partial n} + \frac{\partial\phi_{vo}}{\partial n} + \frac{\vec{U}\cdot\hat{n}\,(1-\mu')}{\vec{U}\cdot\hat{e}_s} \right\} \tag{4.18}
$$

$$
[S_{Jw}^{(i)}]\{\gamma_{wa}^{(i)}\} + [S_{JJ}^{(i)}]\{\gamma_{jj}\} - [T(\mu')^2][S_{Jw}^{(o)}]\{\gamma_{wa}^{(o)}\} -
$$

$$
[T(\mu')^2][S_{JJ}^{(o)}]\{\gamma_{oj}\} = \left\{ - \frac{\partial\phi_{ws}}{\partial s} + T(\mu')^2\frac{\partial\phi_{wc}}{\partial s} \right\} \tag{4.19}
$$

On wing surface

$$
[N_{ww}^{(o)}]\{\gamma_{wa}^{(o)}\} + [N_{wJ}^{(o)}]\{\gamma_{oj}\} = \left\{ \frac{\vec{U}\cdot\hat{i}}{\vec{U}\cdot\hat{e}_s}\frac{\partial z_c}{\partial x} - \frac{\vec{U}\cdot\hat{k}}{\vec{U}\cdot\hat{e}_s} - \frac{\partial\phi_{wc}}{\partial z} \right\} \tag{4.20}
$$

$$
[N_{ww}^{(i)}]\{\gamma_{wa}^{(i)}\} + [N_{wJ}^{(i)}]\{\gamma_{jj}\} = \left\{ \frac{\vec{V}_s\cdot\hat{i}}{\vec{V}_s\cdot\hat{e}_s}\frac{\partial z_c}{\partial x} - \frac{(\vec{U}\cdot\hat{e}_z)(\hat{e}_z\cdot\hat{k})}{\vec{V}_s\cdot\hat{e}_s} - \right.
$$

$$
\left. \frac{\vec{V}_s\cdot\hat{k}}{\vec{V}_s\cdot\hat{e}_s} - \frac{\partial\phi_{ws}}{\partial z} \right\} \tag{4.21}
$$

where the symbol $\lceil\ \rfloor$ represents a diagonal matrix. The system of

Eqs.(4.18)-(4.21) can be solved either by eliminating some of the

unknowns first and then inverting the resulting matrix equation, or

by writing them as an augmented matrix equation for solution. The

latter approach is used here to avoid great number of matrix opera-

tions and great storage problems. For this purpose, Purcell's method

of solution [21] is used, because it requires only $(N_m + 1)^2/4$ com-

puter memory locations for the operation, where N_m is the matrix size,

and much less computing time as compared with some standard direct

matrix inversion methods.

4.6

F

The resulting wing vortex distribution is assumed to be on the camber surface. Noting that the resulting pressure force is normal to the camber surface, the sectional lift and induced drag coefficients can then be obtained by resolving the pressure force in the proper direction and integrating over the local chord. If c_t is the sectional leading-edge thrust coefficient, then

$$c_\ell = \frac{2}{\rho_i V_o c} \int_0^c \rho_o V_o (\vec{U} \cdot \hat{e}_s)\, \gamma_w^{(o)}(x) \cos(\alpha - \delta(x))\, dx + c_t \sin(\alpha - \delta_{LE})$$

$$= \frac{2 \cos\alpha}{c} \int_0^c \gamma_w^{(o)}(x) \cos(\alpha - \delta(x))\, dx + c_t \sin(\alpha - \delta_{LE}) \qquad (4.22a)$$

$$\text{(outside the jet)}$$

$$c_\ell = \frac{2}{\rho_o V_o^2 c} \int_c^c \rho_j V_s (\vec{V}_s \cdot \hat{e}_s)\, \gamma_w^{(i)}(x) \cos(\alpha - \delta(x))\, dx + c_t \sin(\alpha - \delta_{LE})$$

$$= \frac{2}{T \mu^2 c} \int_c^c \gamma_w^{(i)}(x) \cos(\alpha - \delta(x))\, dx + c_t \sin(\alpha - \delta_{LE}) \qquad (4.22b)$$

$$\text{(inside the jet)}$$

where $\delta(x)$ is the angle between the tangent to the camber and the x-axis and δ_{LE} is the same angle at the leading edge. Similarly,

$$c_d = \frac{2 \cos\alpha}{c} \int_0^c \gamma_w^{(o)}(x) \sin(\alpha - \delta(x))\, dx - c_t \cos(\alpha - \delta_{LE}) \qquad (4.23a)$$

$$\text{(outside the jet)}$$

$$c_d = \frac{2}{T \mu^2 c} \int_c^c \gamma_w^{(i)}(x) \sin(\alpha - \delta(x))\, dx - c_t \cos(\alpha - \delta_{LE}) \qquad (4.23b)$$

$$\text{(inside the jet)}$$

In the above expressions, $\gamma_w = \gamma_{wu} + \gamma_{wa}$, where γ_{wu} is the wing vortex strength in the uniform flow. The sectional leading-edge thrust coefficient c_t is computed by exactly the same manner as in a quasi vortex

lattice method in the thin wing theory (see Appendix C). According to Eq.(47) of Appendix C, it is known that

$$c_t = \frac{\pi}{2} \frac{1}{\cos \Lambda_\ell} \sqrt{1 - M^2 \cos^2 \Lambda_\ell} \; C^2 \qquad (4.24)$$

where C is the leading edge suction parameter. The expression for C can be derived from Eqs.(4.20) or (4.21) and similar equations for the uniform flow case. As an example, consider the portion of the wing in the outer flow. If the induced downwash at the ith leading-edge control point in the uniform flow is written as $[N_{WW}]_i \{ \gamma_{wu}^{(o)} \}$, then according to Eq.(46) of Appendix C,

$$N C_1 \sqrt{\tan^2 \Lambda_\ell + \beta^2} = [N_{ww}]_i \{ \gamma_{wu}^{(o)} \} - \{ \frac{\partial \phi_{wv}}{\partial z} \}_i \qquad (4.25)$$

Similarly, for the additional flow, it can be shown from Eq.(4.20) that

$$N C_2 \sqrt{\tan^2 \Lambda_\ell + \beta^2} = [N_{ww}^{(o)}]_i \{ \gamma_{wa}^{(o)} \} + [N_{wj}^{(o)}]_i \{ \gamma_{oj} \} -$$
$$\{ \frac{\vec{U} \cdot \hat{i}}{\vec{U} \cdot \vec{e}_s} \frac{\partial z_c}{\partial x} - \frac{\vec{U} \cdot \hat{k}}{\vec{U} \cdot \vec{e}_s} - (\frac{\partial \phi_{wv}}{\partial z})_i \} \qquad (4.26)$$

where $(\partial \phi_{wv}/\partial z)_i$ is equal to $\partial z_c/\partial x - \alpha$ in the linear wing theory. With C_1 and C_2 computed, C is then equal to the sum of C_1 and C_2, because $\gamma_w = \gamma_{wu} + \gamma_{wa}$.

The sectional pitching moment coefficient about the y-axis can be found from Eqs.(4.27):

$$c_m \cong \frac{2 \cos \alpha}{\bar{c} \, c} \int_0^c \gamma_w^{(o)}(x) \; x \cos(\alpha - \delta(x)) \, dx \qquad (4.27a)$$

(outside the jet)

$$C_m \cong \frac{2}{T\mu^2 \bar{c} c} \int_0^c \gamma_w^{(j)}(x) \, x \, \cos(\alpha - \delta(x)) \, dx \qquad (4.27b)$$

(inside the jet)

In Eqs.(4.27), the small contribution of the drag force to C_m has been ignored. The over-all aerodyanmic characteristics of the wing are determined by spanwise integration of the sectional characteristics. For details, see Appendix C.

To find the influence matrices in Eqs.(4.14)-(4.17), it is assumed that the continuous wing and jet vortex sheets are replaced by step-wise-constant vortex distributions in the spanwise or the circumferential direction. The induced velocity vector due to a "bounded" vortex element of strength $\gamma \, dx_s$ at any location has been found to be (see Appendix A)

$$d\vec{q}_1(\vec{R}) = \frac{\beta^2 \gamma \, dx_s}{4\pi} \frac{\vec{a} \times \vec{\ell}}{|\vec{a}' \times \vec{\ell}'|^2} \left\{ \frac{\vec{b}'}{|\vec{b}'|} - \frac{\vec{a}'}{|\vec{a}'|} \right\} \cdot \vec{\ell}' \qquad (4.28)$$

where x_s measures the downstream distance on the vortex surface, and

$$\vec{a} = (x_1 - x)\hat{i} + (y_1 - y)\hat{j} + (z_1 - z)\hat{k}$$

$$\vec{b} = (x_2 - x)\hat{i} + (y_2 - y)\hat{j} + (z_2 - z)\hat{k}$$

$$\vec{a}' = (x_1 - x)\hat{i} + \beta(y_1 - y)\hat{j} + \beta(z_1 - z)\hat{k}$$

$$\vec{b}' = (x_2 - x)\hat{i} + \beta(y_2 - y)\hat{j} + \beta(z_2 - z)\hat{k} \qquad (4.29)$$

$$\vec{\ell} = (x_2 - x_1)\hat{i} + (y_2 - y_1)\hat{j} + (z_2 - z_1)\hat{k}$$

$$\vec{\ell}' = (x_2 - x_1)\hat{i} + \beta(y_2 - y_1)\hat{j} + \beta(z_2 - z_1)\hat{k}$$

$$\vec{R} = x\hat{i} + y\hat{j} + z\hat{k}$$

The vortex element geometry is shown in Fig. (4.1). Integration

of Eq.(4.28) gives the total induced velocity:

Figure 4.1 Vortex Segment Geometry

$$\vec{q}_1(\vec{R}) = \frac{\beta^2}{4\pi} \int \gamma(x_s) \frac{\vec{a} \times \vec{\ell}}{|\vec{a}' \times \vec{\ell}'|^2} \left\{ \frac{\vec{b}'}{|\vec{b}'|} - \frac{\vec{a}'}{|\vec{a}'|} \right\} \cdot \vec{\ell}' \, dx_s \qquad (4.30)$$

where the integration limits are chosen to cover the whole vortex

sheet.

The induced velocity due to the associated trailing vortices

is, for one side of the strip, (See Appendix A)

$$\vec{q}_2(\vec{R}) = \frac{\beta^2}{4\pi} \int \gamma(x_s) \, dx_s \int_{x_s}^{\infty} \frac{(\vec{R}_1 - \vec{R}) \times d\vec{\ell}}{R_\beta^3} \qquad (4.31)$$

where

$$\vec{R}_1 - \vec{R} = (x' - x)\hat{\imath} + (y' - y)\hat{\jmath} + (z' - z)\hat{k}$$

$$R_\beta^2 = (x - x')^2 + \beta^2(y - y')^2 + \beta^2(z - z')^2 \qquad (4.32)$$

$$d\vec{\ell} = dx'\hat{\imath} + dy'\hat{\jmath} + dz'\hat{k}$$

Let

$$\vec{M}_\ell(x_s, x) = \frac{\vec{a} \times \vec{\ell}}{|\vec{a}' \times \vec{\ell}'|^2} \left\{ \frac{\vec{b}'}{|\vec{b}'|} - \frac{\vec{a}'}{|\vec{a}'|} \right\} \cdot \vec{\ell}' \qquad (4.33)$$

$$\vec{G}_\ell(x_s, x) = \int_{x_s}^{\infty} \frac{(\vec{R}_1 - \vec{R}) \times d\vec{\ell}}{R_\beta^3} \qquad (4.34)$$

Other arguments in $\vec{M}_\ell$ and $\vec{G}_\ell$ have been omitted for simplicity. The

subscript ℓ denotes the spanwise or circumferential strip. The integral

in Eq. (4.30) can be reduced to a finite sum by the quadrature method

to be discussed below. (See Appendix C)

The integration interval is first transformed into $[0, 1]$ through the relation

$$x - x_\ell = (x_t - x_\ell)\, \xi \qquad\qquad (4.35)$$

where x_ℓ is the lower limit and x_t the upper limit. The results are then transformed into the θ-variable by

$$\xi = \tfrac{1}{2}(1 - \cos\theta) \qquad\qquad (4.36)$$

Hence,

$$\vec{q}_1(\vec{R}) = \frac{\beta^2}{4\pi}\int_{x_\ell}^{x_t} \gamma(x_s)\,\vec{M}_\ell(x_s, x)\,dx_s = \frac{\beta^2(x_t - x_\ell)}{8\pi}\int_0^\pi \gamma(\theta)\,\vec{M}_\ell(\theta, x)\sin\theta\,d\theta$$

This last equation is reduced to a finite sum by applying the mid-point modified trapezoidal rule [22]:

$$\vec{q}_1(\vec{R}_i) = \frac{\beta^2(x_t - x_\ell)}{8\pi}\,\frac{\pi}{N}\sum_{k=1}^{N}\gamma(\theta_k)\,\vec{M}_\ell(\theta_k, x_i)\sin\theta_k$$

$$= \frac{\beta^2(x_t - x_\ell)}{8N}\sum_{k=1}^{N}\gamma(\theta_k)\,\vec{M}_\ell(\theta_k, x_i)\sin\theta_k \qquad\qquad (4.37)$$

where

$$\theta_k = \frac{2k-1}{2N}\,\pi\ , \qquad k = 1, 2, \cdots, N \qquad\qquad (4.38)$$

$$x_i = x_\ell + \frac{(x_t - x_\ell)}{2}[1 - \cos\theta_i] \qquad\qquad (4.39)$$

$$\theta_i = \frac{i\pi}{N}\ , \qquad i = 1, \cdots, N \qquad\qquad (4.40)$$

The integration points in Eq. (4.38) are specified by the modified trapezoidal rule, while the control points in Eq. (4.40) are dictated by the requirement of eliminating the Cauchy singularity contained in $\vec{M}_\ell$. Similarly, Eq. (4.31) can be reduced to

$$\vec{q}_2(\vec{R}_i) = \frac{\beta^2(x_t - x_\ell)}{8N}\sum_{k=1}^{N}\gamma(\theta_k)\,\vec{G}_\ell(\theta_k, x_i)\sin\theta_k \qquad\qquad (4.41)$$

The above integration technique has been shown in Appendix C to work well in thin wing theory where γ is known to possess a square root singularity at $x = x_\ell$. This is due to the fact that the square root singularity has been cancelled by $\sin\theta$, so that there is no difficulty in applying the trapezoidal rule. When the integration

4.11

interval is infinite, as is the case when the slipstream is assumed
to be infinite, γ is expected to decay in a certain way. Hence, a
correct and efficient quadrature method to reduce the integration to
a finite sum should be such that both the decaying nature and the
Cauchy singularity in the integrand are accounted for simultaneously.
Of course, such a scheme can be found by first removing the Cauchy
singularity and then applying an appropriate quadrature method.
However, it is expected that the consideration of infinite region is
unnecessary in applications. Only that part of the jet surface which
is close to the wing has to be considered.

From Eqs. (4.37) and (4.41), the total induced velocity at i due
to a vortex strip is

$$\vec{v}_i = \vec{q}_1 + \vec{q}_2$$

$$= \frac{\beta^2 (x_k - x_\ell)}{8N} \sum_{k=1}^{N} \gamma_k \sin \theta_k \left[\vec{M}_\ell (\theta_k, x_i) + \vec{G}_\ell (\theta_k, x_i) \right] \qquad (4.42)$$

It follows that the normal velocity induced at i due to a unit vortex
at k, or the (i,k) element of the influence matrix [N], can be written
as

$$N_{ik} = \frac{\beta^2 (x_k - x_i)}{8N} \sin \theta_k \left[\vec{M}_\ell (\theta_k, x_i) \cdot \hat{n}_i + \vec{G}_\ell (\theta_k, x_i) \cdot \hat{n}_i \right] \qquad (4.43)$$

where $\hat{n}_i$ is the unit normal vector at i. Similarly,

$$S_{ik} = \frac{\beta^2 (x_k - x_\ell)}{8N} \sin \theta_k \left[\vec{M}_\ell (\theta_k, x_i) \cdot \hat{e}_{si} + \vec{G}_\ell (\theta_k, x_i) \cdot \hat{e}_{si} \right] \qquad (4.44)$$

The expressions for $\vec{M}_\ell$ and $\vec{G}_\ell$ are given in detail in Appendix D. It
should be noted that if the influencing vortex is on the jet surface,
8 should be replaced by 4 in Eqs. (4.43) and (4.44).

5. Applications to Wing-Propeller Interactions

5.1 Introduction

As reviewed in the Introduction of Section 1, currently available methods in this area involve one or more assumptions in the formulation in addition to the linearization of the problem. For the purposes of presenting the objectives of the present applications, these assumptions will be further discussed below. (1) Except Shollenberger, all existing methods used the Weissinger's lifting line method or its variants for the wing representation. The distributions of sectional induced drag and pitching moment have not been obtained. (2) Ribner and Ellis [17] formulated the jet pressure condition in terms of velocity potentials directly by integrating the pressure condition expressed in terms of tangential velocities. Further, they satisfied the pressure condition by using a doublet sheet associated with an unperturbed flow field. Their results for the lift increment are comparable to those obtained by the slender body theory but are too low compared with Brenckmann's experiments [23]. It is not known whether this is due to the inherent limitation of the linearized potential flow theory or due to the computational techniques. (3) No existing techniques are capable of accounting for different jet Mach number from the freestream one, even in the linearized theory. Therefore, the high thrust condition where the jet Mach number may not be negligible can not be treated.

With the defficiencies of the existing techniques in mind, the objectives of the present formulation with applications to the wing-

propeller interactions are as follows. (1) The linearized problem

is to be solved as accurately as possible in order to determine whether

the linearized potential flow theory is adequate for this type of

problems. (2) Using the best available lifting surface technique,

the c_ℓ, c_d and c_m distributions can be determined and compared with

available wind-tunnel data. In this way, if the linearized potential

flow theory is to be used, the problem areas to be further studied

can be identified. (3) Using the present lifting-surface technique,

the importance of different Mach numbers inside and outside the slip-

stream can be assessed.

5.2 Mathematical Formulation

The slipstream cross section will be assumed to be circular with

constant diameter, and extended upstream as far as practical and down-

stream to infinity, with its unperturbed velocity being constant and

the same everywhere. Theoretically, the flow field ahead of the pro-

peller due to the propeller alone can be approximated as that produced

by a uniform sink distribution over the propeller disk [13]. Since

this flow field is nonuniform and is regarded as part of the base flow,

not the perturbed flow, the perturbation due to the introduction of the

wing is difficult to compute, because the governing partial differential

equation would be one with variable coefficients. On the other hand,

since the nonuniform flow inside the slipstream has been approximated

by a uniform one which may be computed by the momentum theory, it is

not well justified to use a more complicated model for the flow ahead

of the propeller. Therefore, the classical assumption of infinite

silpstream is retained here.

The right hand sides of the boundary conditions Eqs.(4.10)-(4.13)

can be simplified for the following two cases:

<u>Case 1.</u> Slipstream not at an angle of attack.

In practice, this may be the case where the propeller is not

directly attached to the wing, a configuration which has been used

in some experiments. See Figure 5.1. Apparently, $\vec{U} \cdot \hat{n} = 0$, $\vec{U} \cdot \hat{k} = V_o \sin \alpha$,
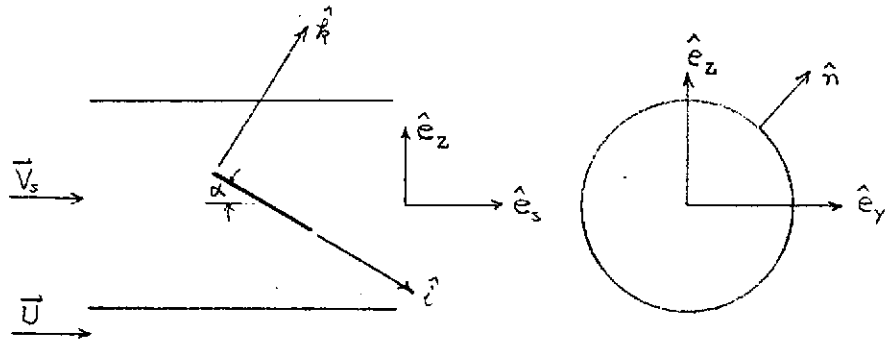
Figure 5.1 Slipstream Geometry for Case 1

$\vec{U} \cdot \hat{\imath} = V_o \cos \alpha$, $\vec{V_s} \cdot \hat{k} = V_\theta + V_s \sin \alpha$ and $\vec{V_s} \cdot \hat{\imath} = V_s \cos \alpha$, where V_θ is

the rotational component of the propeller flow. It follows that Eqs.

(4.10)-(4.13) can be written as

On slipstream $\left\{ \begin{array}{l} \dfrac{\partial \psi_s}{\partial n} - \dfrac{\partial \psi_o}{\partial n} = - \dfrac{\partial \phi_{ws}}{\partial n}(M_s) + \dfrac{\partial \phi_{wo}}{\partial n}(M_o) \qquad (5.1) \\[3ex] \dfrac{\partial \psi_s}{\partial s} - T(\mu')^2 \dfrac{\partial \psi_o}{\partial s} = - \dfrac{\partial \phi_{ws}}{\partial s}(M_s) + T(\mu')^2 \dfrac{\partial \phi_{wo}}{\partial s}(M_o) \qquad (5.2) \end{array} \right.$

surface

$$\frac{\partial \psi_o}{\partial Z} = \cos\alpha \, \frac{\partial Z_c}{\partial X} - \sin\alpha - \frac{\partial \phi_{wo}}{\partial Z}(M_o) \qquad (5.3)$$

On wing
surface
(outside the slipstream)

$$\frac{\partial \psi_s}{\partial Z} = \cos\alpha \, \frac{\partial Z_c}{\partial X} - \sin\alpha - \frac{V_\theta}{V_s} - \frac{\partial \phi_{ws}}{\partial Z_s}(M_s) \qquad (5.4)$$

(inside the slipstream)

where $\mu' = \vec{U}\cdot\hat{e}_s / \vec{V}_s\cdot\hat{e}_s = V_o/V_s = \mu$ and M_s is the slipstream Mach number. If both ϕ_{wo} and ϕ_{ws} are determined under the wing boundary condition:

$$\frac{\partial \phi_w}{\partial Z}(x, Y, o) = \cos\alpha \, \frac{\partial Z_c}{\partial X} - \sin\alpha \quad , \qquad (5.5)$$

then Eqs.(5.3) and (5.4) become

On wing
surface

$$\frac{\partial \psi_o}{\partial Z} = 0 \qquad (5.3a)$$

$$\frac{\partial \psi_s}{\partial Z} = -\frac{V_\theta}{V_s} \quad . \qquad (5.4a)$$

Note that the right hand side of Eq.(5.1) will be zero only if $M_o = M_s$.

Case 2. Slipstream at an angle of attack.

This is the more realistic configuration where the propeller is fixed relative to the wing so that the slipstream will rotate with the wing. See Figure 5.2. In this case, it can be shown that

$$\hat{n} = \hat{j}\cos\theta + \hat{k}\,\sin\theta \qquad (5.6a)$$

$$\vec{U} = V_o \cos\alpha \, \hat{i} + V_o \sin\alpha \, \hat{k} \qquad (5.6b)$$

$$\mu' = \vec{U}\cdot\hat{e}_s / \vec{V}_s\cdot\hat{e}_s = \mu\cos\alpha \qquad (5.6c)$$
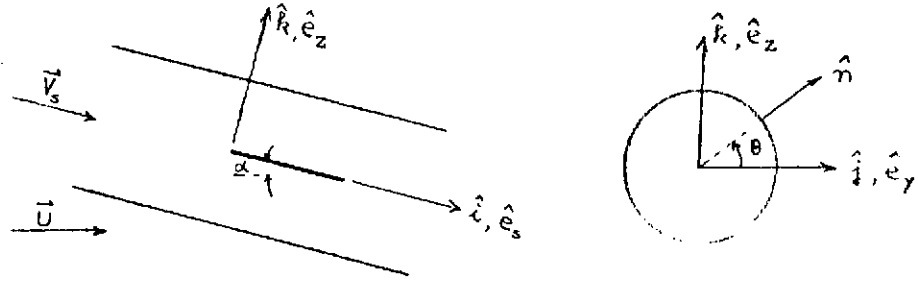
Figure 5.2   Slipstream Geometry for Case 2

Therefore, Eqs. (4.10)-(4.13) become

On slipstream surface

$$\frac{\partial \psi_s}{\partial n} - \frac{\partial \psi_0}{\partial n} = -\frac{\partial \phi_{ws}}{\partial n}(M_s) + \frac{\partial \phi_{w0}}{\partial n}(M_0) + \tan \alpha \sin \theta (1 - \mu') \qquad (5.7)$$

$$\frac{\partial \psi_s}{\partial s} - T (\mu')^2 \frac{\partial \psi_0}{\partial s} = -\frac{\partial \phi_{ws}}{\partial s}(M_s) + T (\mu')^2 \frac{\partial \phi_{w0}}{\partial s}(M_0) \qquad (5.8)$$

On wing surface

$$\frac{\partial \psi_0}{\partial Z} = \frac{\partial Z_c}{\partial x} - \tan \alpha - \frac{\partial \phi_{wc}}{\partial Z} \qquad (5.9)$$
$$\text{(outside the slipstream)}$$

$$\frac{\partial \psi_s}{\partial Z} = \frac{\partial Z_c}{\partial x} - \mu \sin \alpha - \frac{V_\theta}{V_s} - \frac{\partial \phi_{ws}}{\partial Z} \qquad (5.10)$$
$$\text{(inside the slipstream)}$$

Now, if the wing boundary condition in the uniform flow is taken to be:

$$\frac{\partial \phi_w}{\partial Z}(x, Y, 0) = \frac{\partial Z_c}{\partial x} - \tan \alpha \quad, \qquad (5.11)$$

Eqs. (5.9) and (5.10) become

$$\frac{\partial \psi_0}{\partial Z} = 0 \qquad (5.9a)$$

$$\frac{\partial \psi_s}{\partial z} = \tan \alpha - \mu \sin \alpha - \frac{V_\theta}{V_s} \tag{5.10a}$$

Notice that Eqs. (5.5) and (5.11) have the same form if α is small.
Also notice the difference in wing boundary conditions inside the
slipstream for the above two cases as defined by Eqs. (5.4a) and (5.10a).
The solution techniques described in Section 4 are used to solve the
above problems.

5.3 Numerical Results and Discussion

Case 1. Slipstream not at an angle of attack

Some of the important existing methods are applicable only to
this case. See, for example, Res. [14] and [17]. To check out the
present program, a wing of A = 5.25 with a centered jet of μ = 0.735
as used by Rethorst [14] will be employed for comparison. No slip-
stream rotation has been assumed. Instead of extending the slipstream
to infinity both upstream and downstream, the present results were
obtained by extending the slipstream 30 chord lengths upstream from
the wing leading edge and 10 chord lengths downstream from the trail-
ing edge for the purpose of satisfying the slipstream boundary condi-
tions. This slipstream extent was determined through numerical experi-
mentation to ensure that the results will change as little as possible.
Symmetry with respect to the x-z and x-y planes has been accounted
for to reduce the number of unknowns. Only 8 circumferential vortex

strips on the slipstream surface were used, as it was found that by
increasing the circumferential vortex strips to 12, the results changed
by only 0.5%. α is assumed small so that $\cos \alpha \approx 1$ and $\sin \alpha \approx \alpha$.
The span loadings predicted by various methods are compared in Figure
5.3. The results by other theories are taken directly from Ref. [17],
except Shollenberger's which are obtained from Ref [11b]. It is seen
that the present method compares most favorably with Rethorst's method
[14]. It appears that both Ribner and Ellis, and Shollenberger pre-
dicted lower loading outside the slipstream as compared with the
present method.

Figure 5.4 shows the comparison with the lifting line theory of
Kleinstein and Liu for an elliptic wing of aspect ratio 6.5 with a
centered jet. The nonuniform effects on the sectional lift curve
slope have been included in this lifting line theory. Again, the slip-
stream rotation is assumed zero in the computation. The lift increment
inside the slipstream as predicted by Kleinstein and Liu is approxi-
mately 10% higher than that predicted by the present method.

Brenckmann's experimental results [23] for the span loading are
compared in Figures 5.5-5.6, where the sectional lift coefficient $\bar{c}_{\ell}$
is based on the average dynamic pressures. The experimental slip-
stream rotation [23] was used in the present program by curve-fitting
the measured results by a 4th-degree polynomial. However, the flow
rotation outside the slipstream was assumed zero. Since the wing
used in the measurement spanned the wind tunnel, in the present program
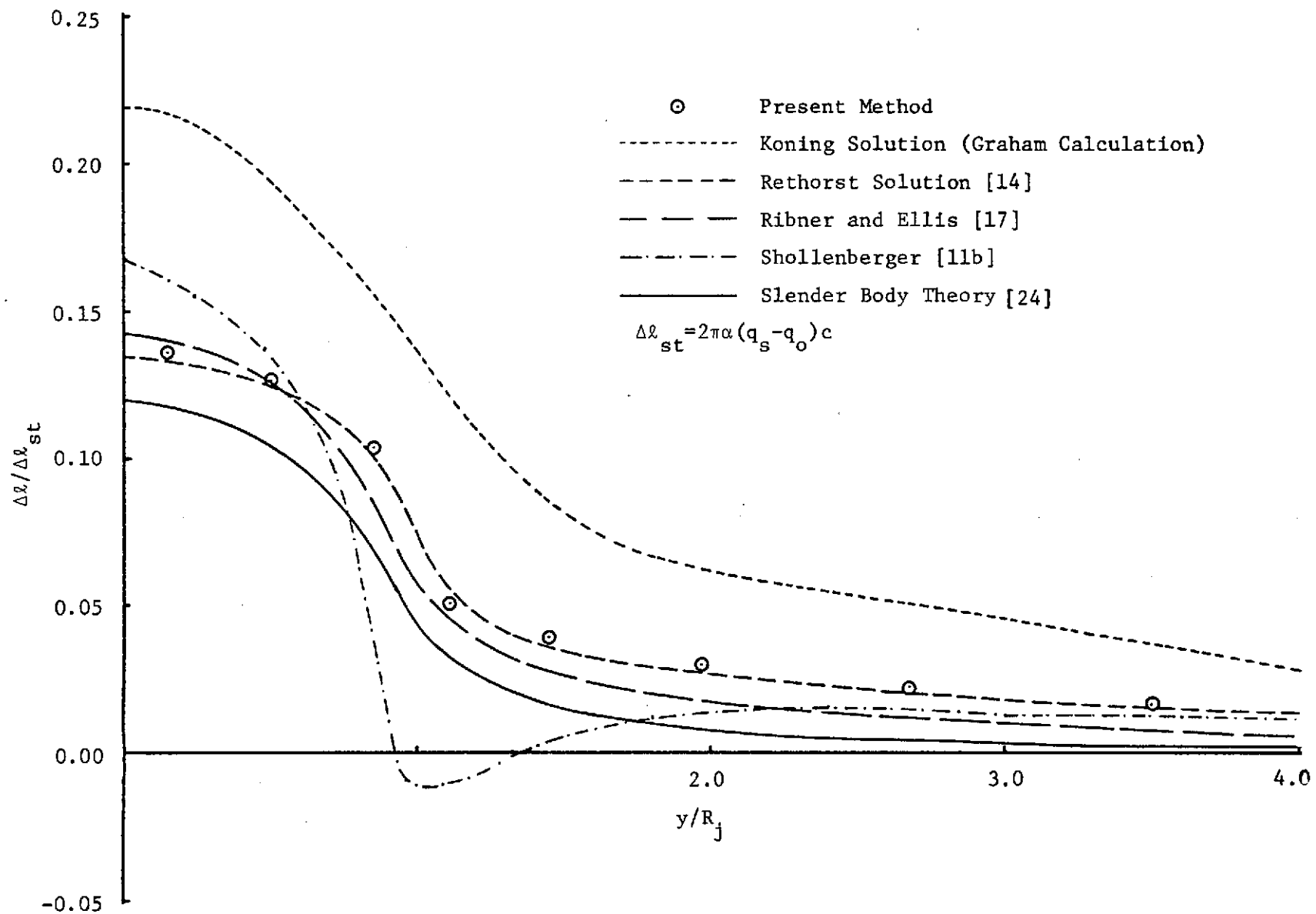
Figure 5.3 Comparison of Span Loadings Predicted by Several Theories. D/c=0.6,μ=0.735

⊙   Present Method

-------- Koning Solution (Graham Calculation)

— — — Rethorst Solution [14]

— — — Ribner and Ellis [17]

—·—·— Shollenberger [11b]

————— Slender Body Theory [24]

$$\Delta \ell_{st} = 2\pi\alpha(q_s - q_o)c$$

Vertical axis: $\Delta \ell / \Delta \ell_{st}$ with values 0.25, 0.20, 0.15, 0.10, 0.05, 0.00, -0.05

Horizontal axis: y/R_j with values 2.0, 3.0, 4.0
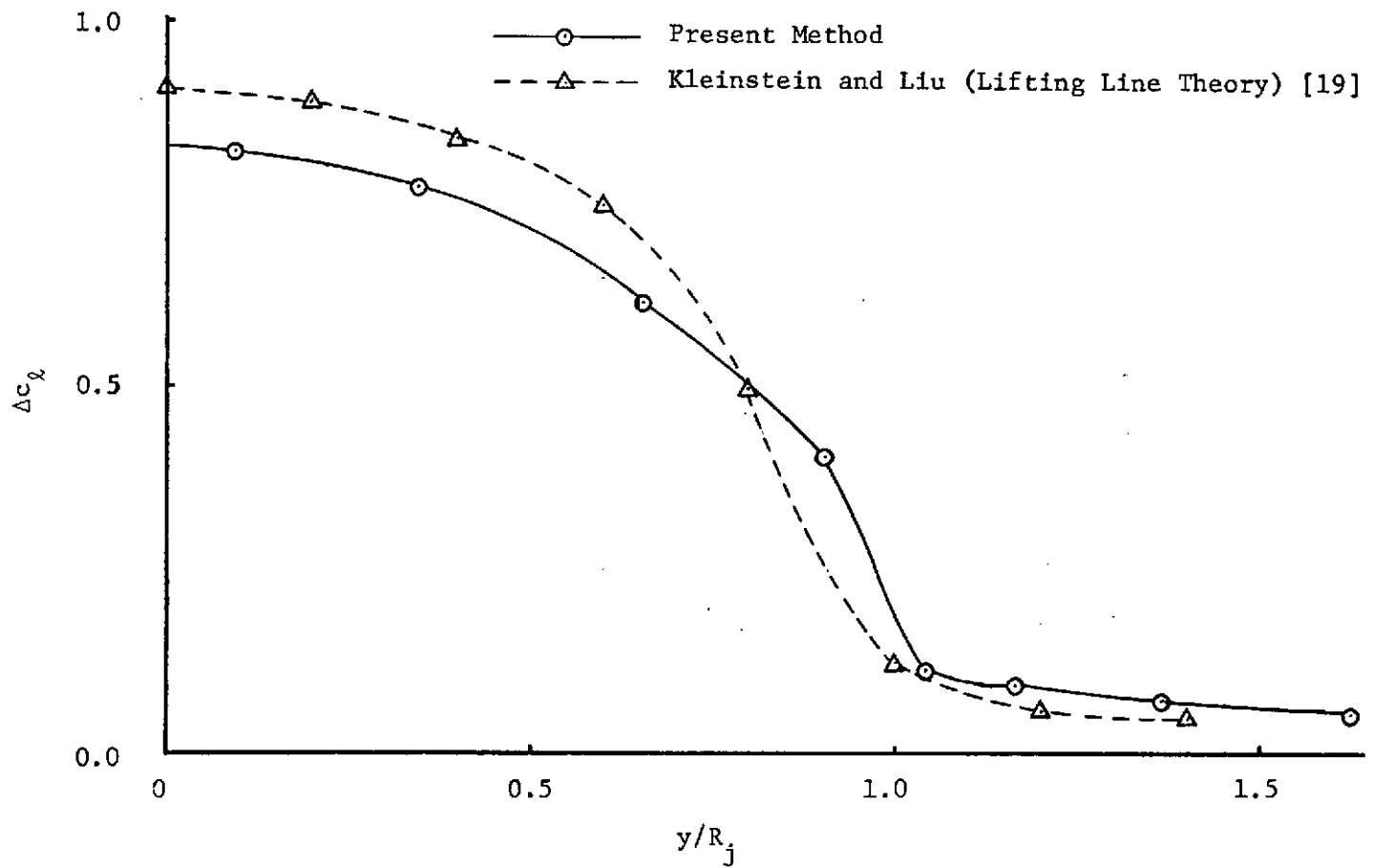
Figure 5.4 Comparison of Lift Increments Predicted by the Present Method and the Lifting Line Theory for an Elliptic Wing of A=6.5 at $\alpha = 5°$. $D/c_r = 1.46, \mu = 0.5$
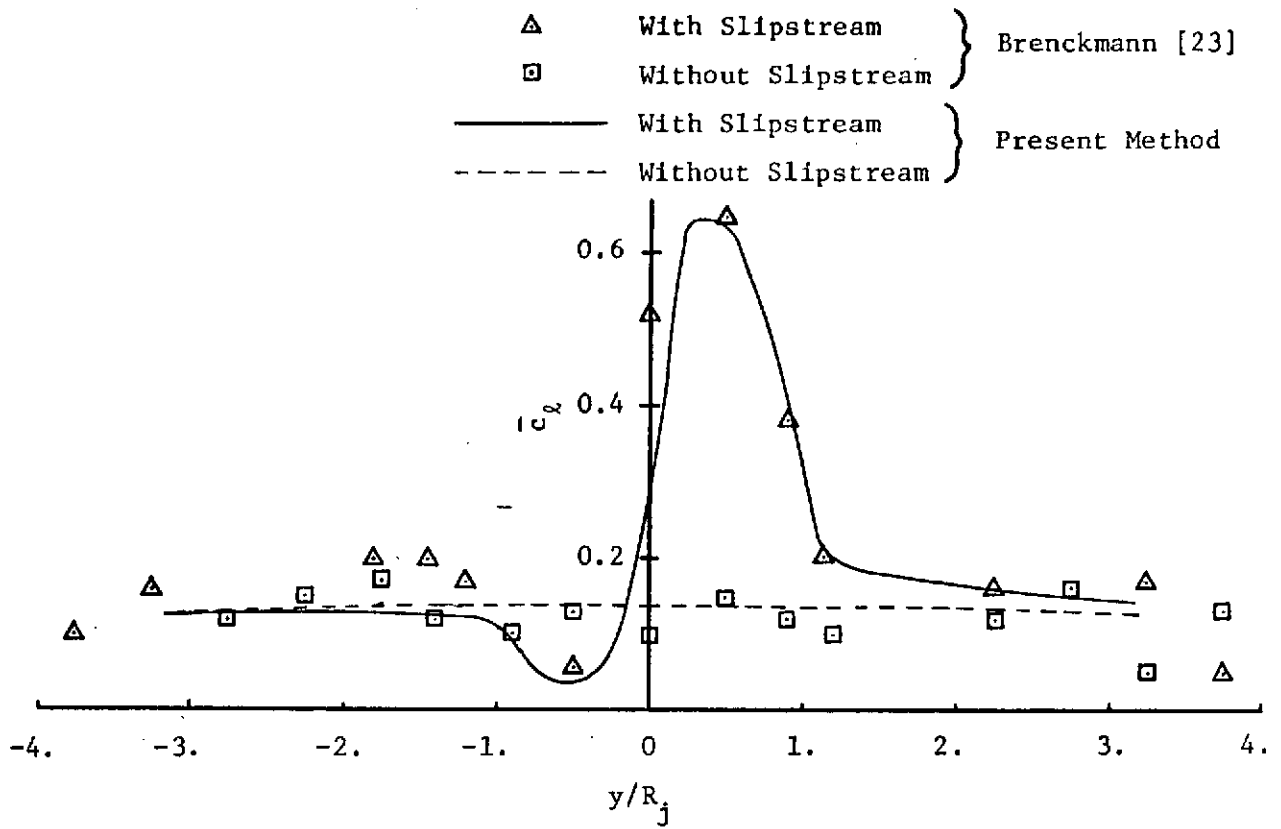
Figure 5.5 Comparison of Span Loadings by the Present Method and Experiment. $D/c=1.0, \mu =0.36927, \alpha =6.5°$
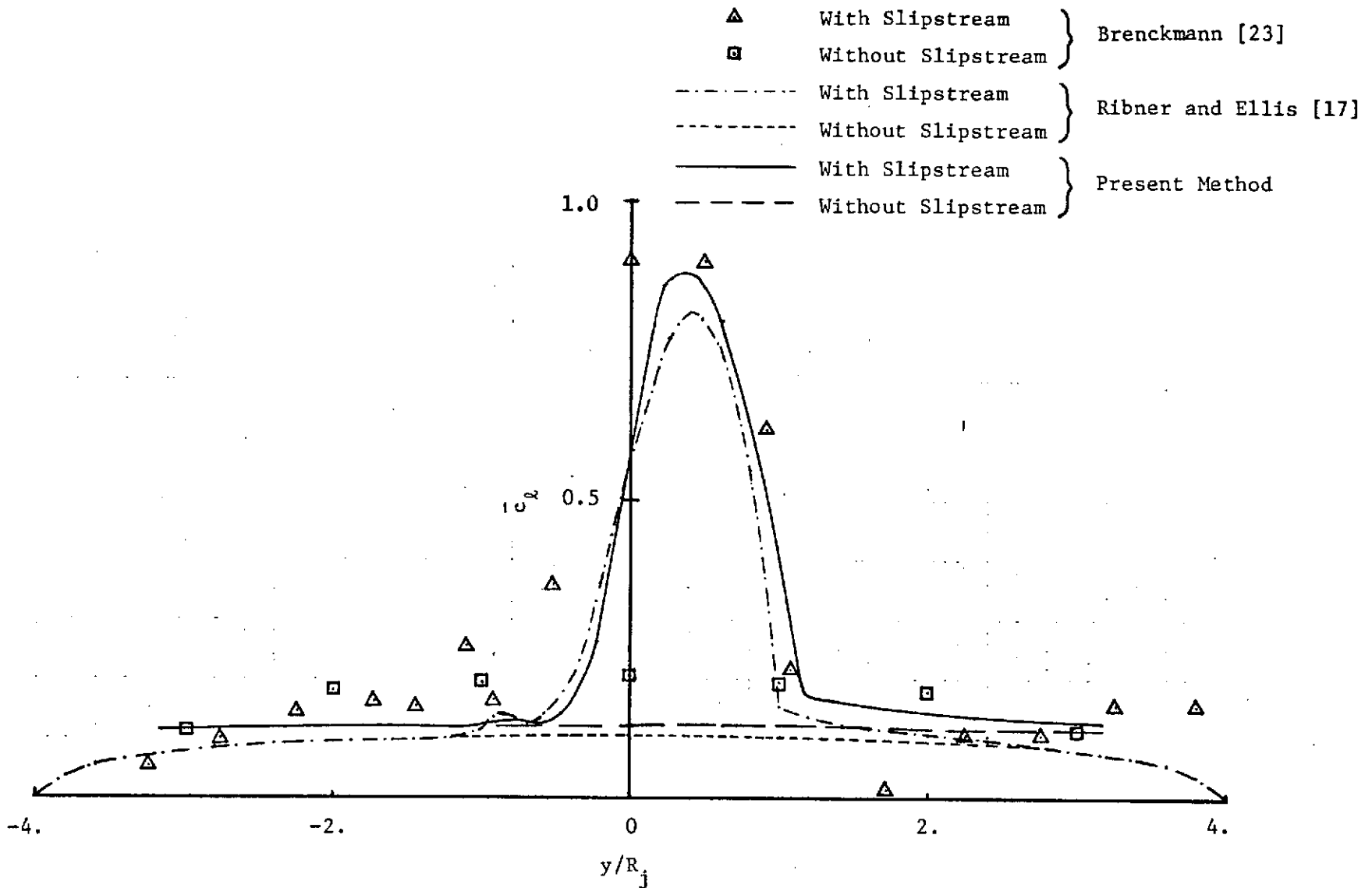
Figure 5.6 Comparison of Span Loadings by the Present Method and Experiment. D/c=1.0, μ =0.25265, α =11.5°

an appropriate aspect ratio (A = 6.25) was chosen so that the program
would predict correctly the sectional lift coefficient at the plane
of symmetry for the wing alone case at α = 6.5°. Again, 8 circum-
ferential vortex strips were used on the slipstream surface. By
increasing the circumferential strips to 10, the total lift coef-
ficient was found to change by only 0.6%. The slipstream extent within
which the slipstream boundary conditions are satisfied in the computa-
tion was dictated by requiring less than 1% of change in the total
lift coefficient for different slipstream lengths. In this way, the
slipstream was extended 2.5 D upstream of the wing leading edge and
5 D downstream of the trailing edge. In fact, the downstream extent
was later found not as important as the upstream one. From the com-
parison of the span loading, it can be seen that the agreement of the
present results with the experiment is good in the region subject to
the propeller upwash, but less satisfactory in the propeller downwash
region. The total lift increment is compared in Figure 5.7. The pre-
sent linear theory predicts the ratio $\Delta L/\Delta L_{ST}$ to be independent of α ,
while the experiments show that it is a function of α . The main reason
may be as follows. At α = 11.5°, experimental results indicated that
some portion of the wing in the uniform flow was subject to flow
separation. It follows that the lift coefficient in the uniform flow
would be much lower than that predicted by the present potantial flow
theory. On the other hand, due to the blowing effects of the slip-
stream, the potential flow results may be attained even at α = 11.5°.
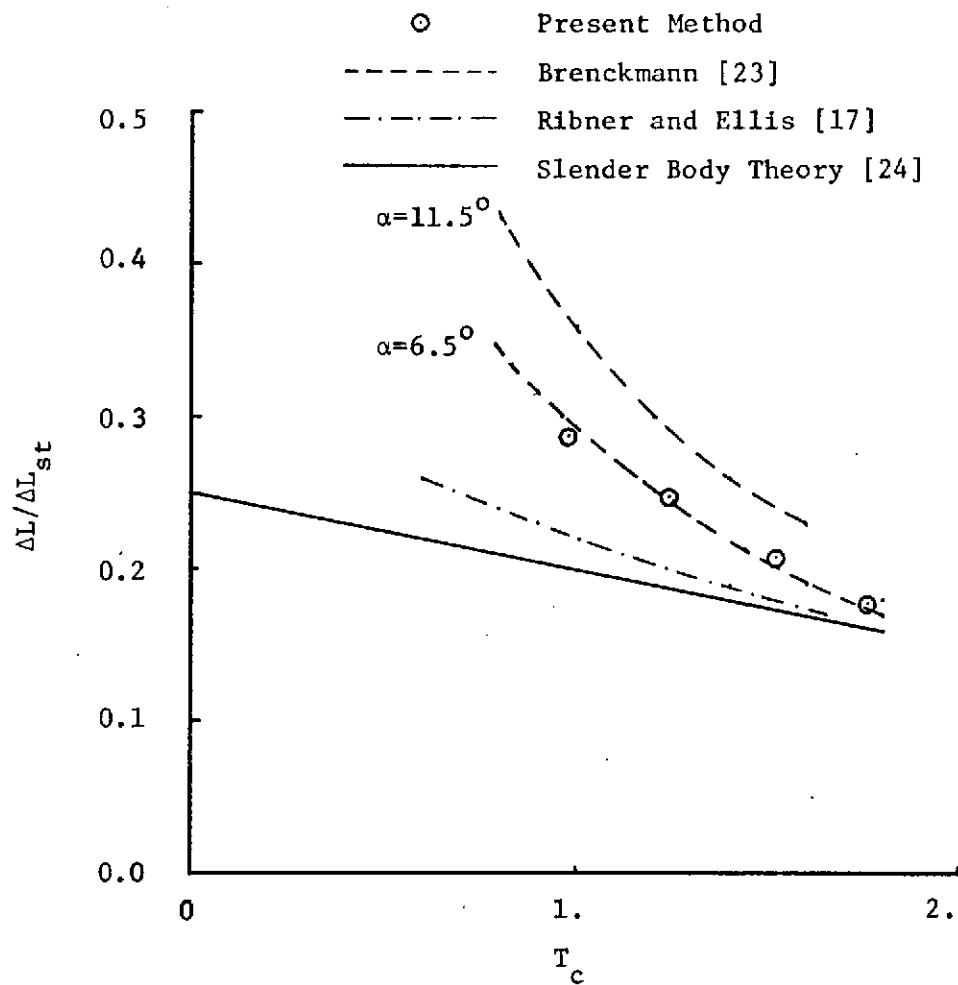
Figure 5.7 Comparison of Total Lift Increments Predicted
by Theories and Experiments. D/c=1.0

Therefore, ΔL in the present method would be too low, because a too large C_L of the wing alone case has been subtracted. The results of Ribner and Ellis are seen to be closer to those obtained by the slender body theory.

Case 2. Slipstream at an angle of attack

Even though this is the more realistic configuration in practice, no theoretical results for c_ℓ, c_d and c_m distributions are available for comparison. It may be mentioned that Levinsky et al [18] have accounted for the slipstream inclination in their model. However, they satisfied the slipstream boundary conditions in the Trefftz plane and the wing tangency condition at the wing three-quarter chord line, as did Ribner and Ellis in Ref.[16]. Ribner and Ellis have found later that this procedure produced inaccurate results [17]. In addition, no c_d and c_m distributions have been computed in Ref. [18]. Therefore, only comparison with experimental results will be made here.

Recently, Nishimura of National Aeronautical Establishment of Canada [25] measured detailed aerodynamic characteristics of some half models with propeller diameter-wing chord ratio of 4/3 and of NACA 4415 airfoil section. The propeller diameter-semispan ratio is 0.567 for the first wing to be compared. The measured pressure distribution was integrated to give the spanwise distribution of c_ℓ, c_d and c_m. Discrepancies exist in the integrated over-all charac-teristics (C_L, C_D and C_m) with the corrected balance measurements. The present comparison will be made with the pressure-integrated values.

To use the present method for comparison with experiments, two difficulties are encountered. (1) The actual slipstream dynamic pressure distribution is far from uniform. Brenckmann defined an equivalent dynamic pressure for data reduction [23]. However, since no actual slipstream dynamic pressure distribution has been reported in Ref. [25], an equivalent slipstream dymanic pressure can not be defined. In the following comparison, the slipstream dynamic pressure, and hence, the velocity ratio, is computed by the momentum theory as follows:

$$\left(\frac{q_c}{q_s}\right)^2 = 1 - T_c \qquad (5.12)$$

where T_c is the thrust coefficient based on q_s. (2) The slipstream rotational flow V_θ was not reported. Levinsky et al [18] proposed a semi-empirical formula for V_θ. However, this formula does not always produce correct shapes for the variation of the rotational angles, $\tan^{-1}(V_\theta/V_s)$, with radial distance as compared with some measurements, such as Ref. [23]. Since Brenckmann's measurements of rotational angles are available, they are assumed to be applicable to other configurations if $J \frac{V_\theta}{V_s} \frac{\Delta H}{q_c}$ is the same. Since $\Delta H \cong q_s^2 - q_c^2$, this criterion requires $J(1-\mu^2)/\mu$ to be the same. This criterion is obtained from the inviscid propeller theory with constant blade loading. For the present application with $T_c = 0.8$, J is found to be 0.316 [25]. From Eq. (5.12), μ can be computed as 0.44721. Therefore, $J(1-\mu^2)/\mu = 0.5653$. This same parameter is found to be 0.5667 for $\sigma = 0.76$ in Brenckmann's measurements. Therefore, Brenckmann's curve for $\tan^{-1}(V_\theta/V_s)$ at $\sigma = 0.76$

is used in the following computation.

The camber slope for NACA 4415 airfoil can be described analytically by the following relations [26]:

$$\frac{\partial z_c}{\partial x} = \left(0.8 - 2\frac{x}{c} \right)/4 \qquad , \qquad \frac{x}{c} \leq 0.4 \qquad (5.13a)$$

$$\frac{\partial z_c}{\partial x} = \left(0.8 - 2\frac{x}{c} \right)/9 \qquad , \qquad \frac{x}{c} \geq 0.4 \qquad (5.13b)$$

The slipstream extent to be included in the actual computation was again determined through numerical experimentation. In the following numerical examples, the slipstream extent is taken to be from 4 D ahead of the wing leading edge to 5 D behind the trailing edge. Since the experimental results are somewhat affected by the tunnel floor boundary layer and the nacelle, the following comparison is made only in terms of incremental changes. In addition, the center line of the slipstream is slightly below the wing plane in the experiment. This fact has been ignored in the computation. The interaction between slipstream surfaces have been included. However, the flow inside the slipstream on one side is not affected directly by its image region on the other side, but only indirectly through the outer flow. Figure 5.8 shows the spanwise distribution of Δc_ℓ, Δc_m and Δc_d. The agreement is reasonable good in view of the assumption made regarding the slipstream rotation. Δc_d is seen to be too high on the propeller-downwash side. This is due to the under-prediction of the leading edge thrust. Some typical chordwise pressure distributions in this region and in the upwash region are compared in Figure 5.9. It is
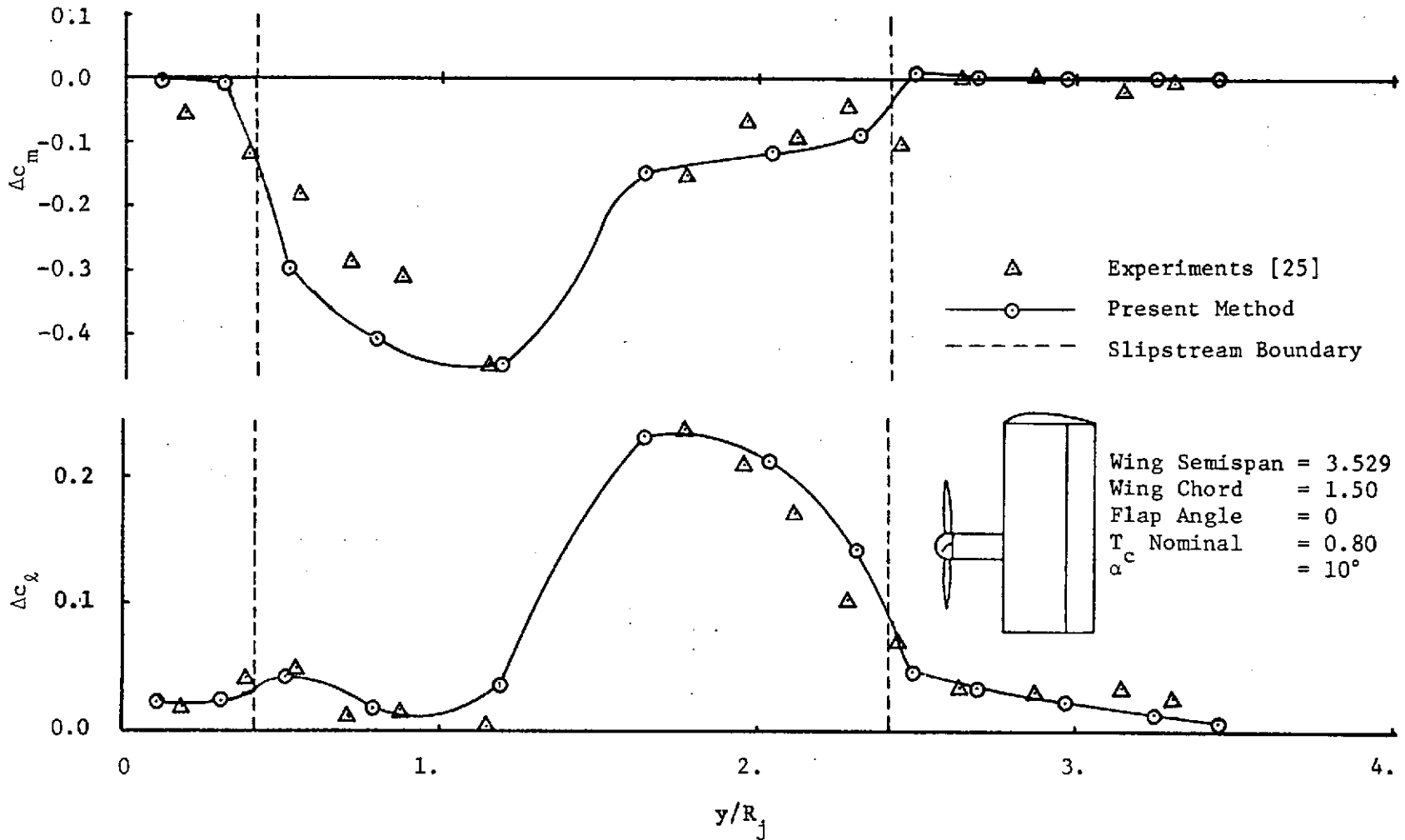
Figure 5.8 Comparison of Predicted Δc_ℓ, Δc_m and Δc_d with Experiments for a Rectangular Wing of A=4.705 at α=10°. D/c=4/3, μ=0.44721
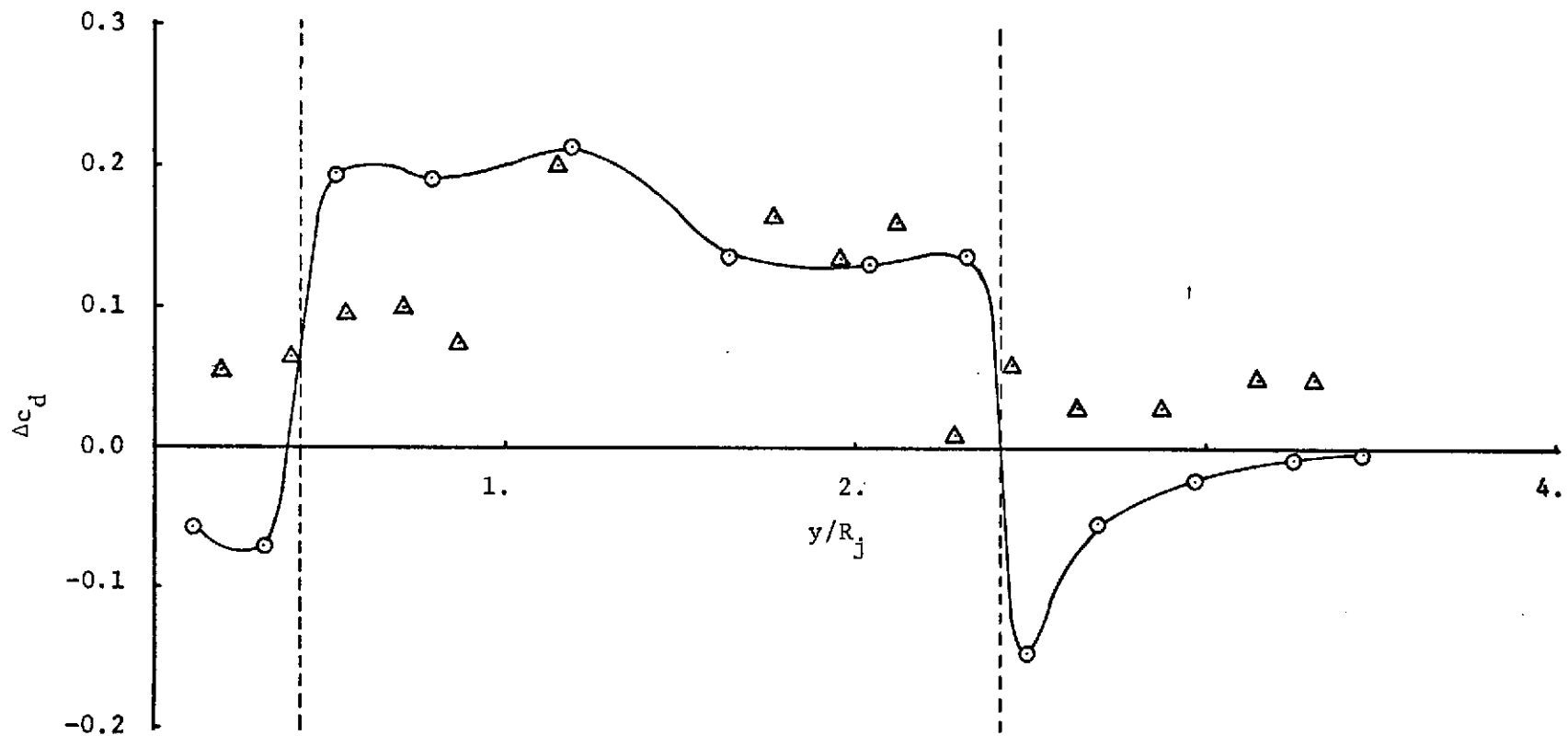
Figure 5.8 Concluded
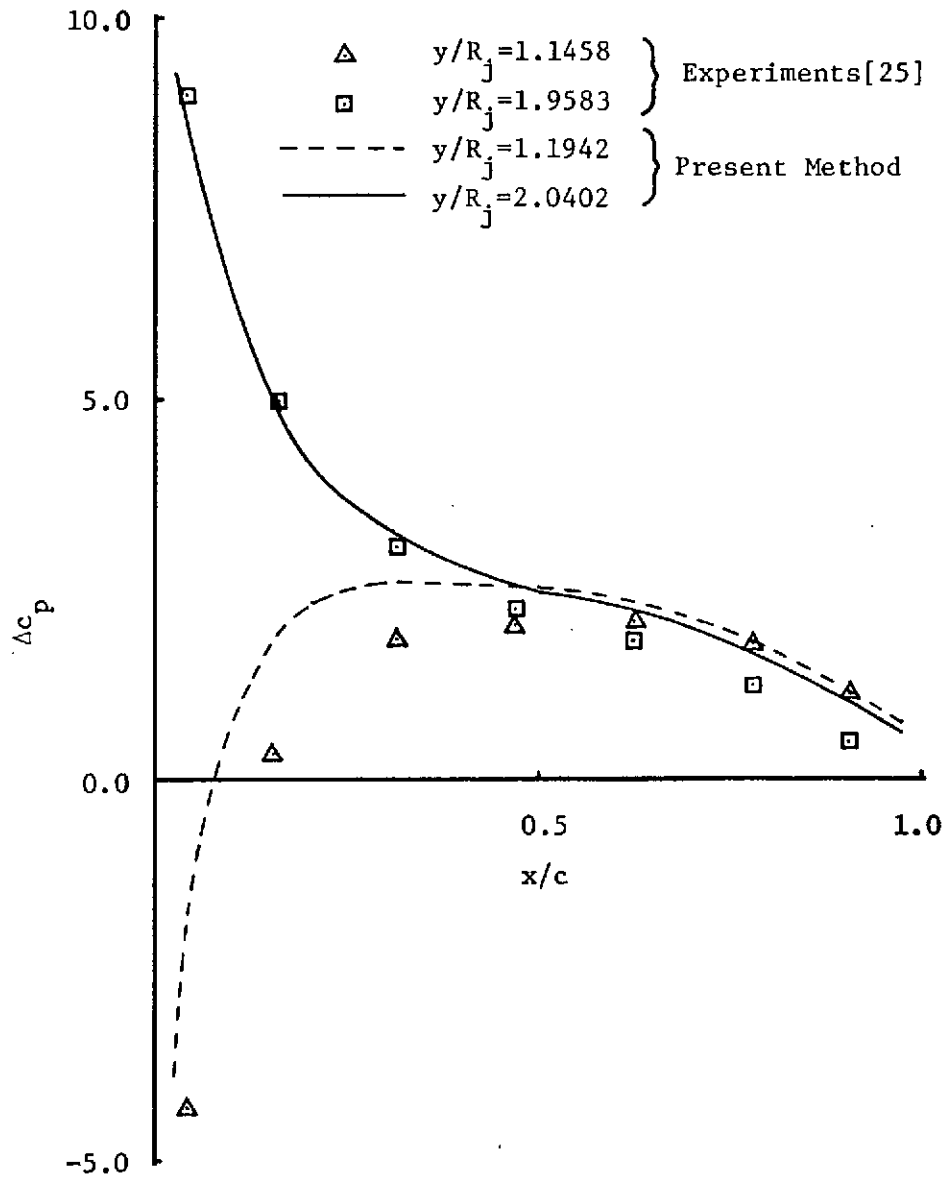
Figure 5.9 Comparison of Predicted Chordwise Pressure
Distributions with Experiments for a Rectangular
Wing of A=4.705 atα=10°. D/c=4/3, μ=0.44721

seen that the predicted pressure level near the leading edge in the
downwash region is too low. The negative loading near the leading edge
is primarily due to the leading-edge camber. When the propeller down-
wash was eliminated, the negative loading remained. However, with
the propeller downwash included but the region $x/c \leq 0.4$ in the pro-
peller downwash side replaced with uncambered section, the negative
loading disappeared. This negative loading tends to shift the center
of pressure backwards. The second feature of the theoretical
distribution which may be mentioned is concerned with the values near
any discontinuities in wing properties. The discontinuity in the
present case is at the slipstream surface. Near the discontinuity
outside the slipstream, Δc_d becomes negative. This is due to the
over-prediction of the leading edge thrust. Similar characteristics
of the c_d distribution occurs in wing theory in uniform flow for a
variable sweep wing [27]. The second wing compared is that of $A = 3.22$
and full-span flap deflection of $15°$. Most of the half span is covered
by the slipstream with the propeller diameter-semispan ratio being
0.83. The comparison of Δc_l and Δc_d is presented in Figure 5.10.
Δc_m has not been compared, because the experimental c_m distribution
is difficult to read from the crowded curves. The incremental over-
all aerodynamic characteristics are given in Table 5.1.

In the applications related to Table 5.1, 245 simultaneous equa-
tions have been solved with 34 K (decimal) memory and a total process-
ing time of 11 minutes on Honeywell 635. No tapes have been used.
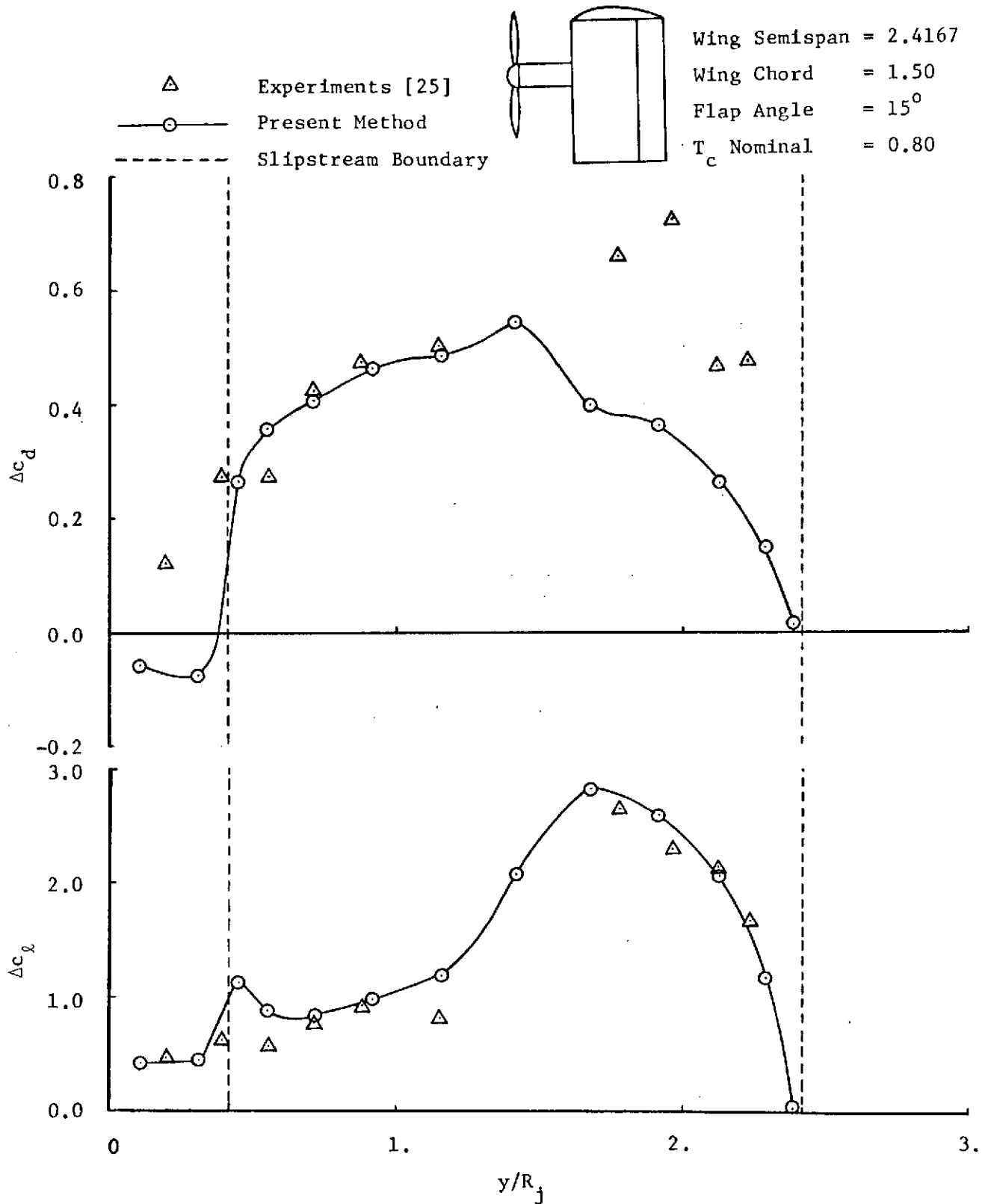
Figure 5.10 Comparison of Predicted Δc_ℓ and Δc_d with Experiments for a Rectangular Wing of A=3.22 at $\alpha=10^o$. D/c=4/3, $\mu=0.44721$

Table 5.1

Comparison of Predicted Aerodynamic Characteristics with Experiments with Wing-Slipstream Interaction

	A = 4.705		A = 3.22	
	Present	Experiment	Present	Experiment
ΔC_L	0.771	0.755	1.414	1.43
ΔC_D	0.0752	0.1	0.3044	0.39
ΔC_m	-0.1444	-0.14	-0.371	-0.425

Having established the accuracy of the present method in incompressible flow, it is of interest to see how the non-uniformity of Mach numbers would affect the predicted aerodynamic characteristics. For this purpose, the configuration used in Figure 5.8 will be used. The propeller thrust, and hence, the velocity ratio, is assumed constant while the freestream Mach number is increased from 0.1 to 0.3. The slipstream Mach number is taken to be proportional to the slipstream velocity. Let $c_\ell(M_o)$ be the predicted sectional lift coefficient when the Mach number is assumed to be M_0 everywhere and $c_\ell(M_s)$ the predicted sectional lift coefficient with Mach number non-uniformity. The percent increase, $[c_\ell(M_s) - c_\ell(M_o)]/c_\ell(M_o)$, is shown in Figure 5.11. It should be noted that if the Prandtl-Glauert transformation is used locally, then

$$c_\ell(M_s) = c_\ell(M_o) \sqrt{\frac{1 - M_o^2}{1 - M_s^2}}$$

$$\frac{c_\ell(M_s) - c_\ell(M_o)}{c_\ell(M_o)} = \sqrt{\frac{1 - M_o^2}{1 - M_s^2}} - 1 \tag{5.14}$$
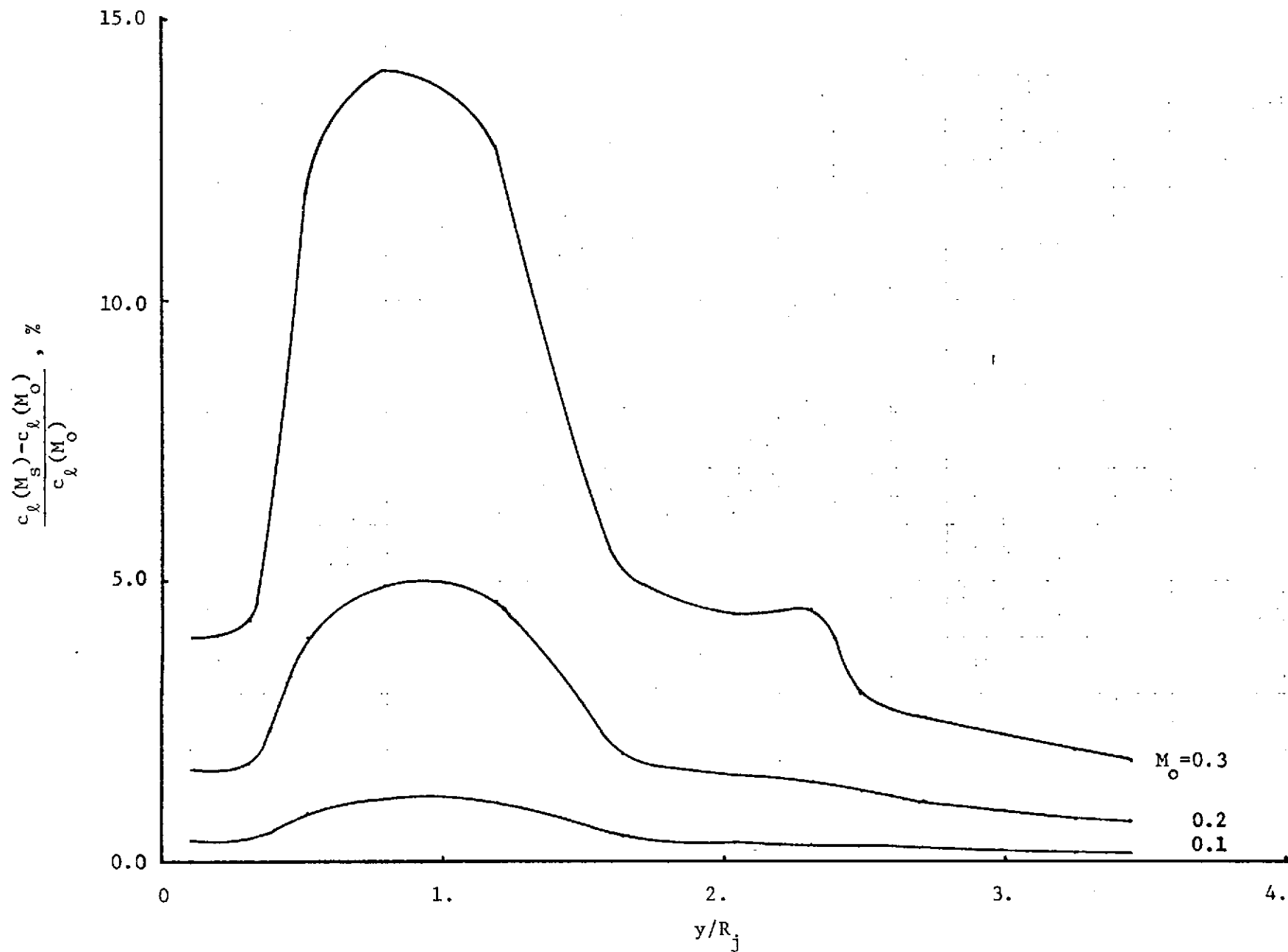
Figure 5.11 Effect of Mach Number Nonuniformity on the Span Loading for the
Configuration of Figure 5.8

Therefore, for M_o = 0.1, 0.2 and 0.3, Eq. (5.14) would give 2.1%,

9.5% and 28.6%, respectively. It is seen that the sectional lift

increment is much less than that predicted by the Prandtl-Glauert

transformation. This fact can be explained as follows. As the slip-

stream Mach number is increased, the sectional lift coefficient based

on q_s in the uniform flow with the corresponding M_s would also be

increased. However, the effect of the slipstream surface, which is

to reduce this uniform flow loading, is also increased. As discussed

in Appendix B, this slipstream surface effect can be approximately

explained by a reflection coefficient. In the two-dimensional flow

this reflection coefficient can be written in the present notation as

$$\lambda_{12} = -\frac{\dfrac{S_o V_o^2}{S_s V_s^2} - \dfrac{\beta_o}{\beta_s}}{\dfrac{S_o V_o^2}{S_s V_s^2} + \dfrac{\beta_o}{\beta_s}} \qquad (5.15a)$$

If $S_o = S_s$ and V_o/V_s = 0.44721, then λ_{21} = 0.667 if $M_o = M_s$. However,

if $M_o \neq M_s$, then λ_{21} = 0.672, 0.691, 0.731, respectively, for M_o = 0.1,

0.2 and 0.3. Increase in the positive reflection coefficient implies

increase in the reduction of loading inside the slipstream due to

the slipstream surface, as discussed in Appendix B. On the other

hand, the diffracted disturbances into the slipstream region from the

outer flow, which are to oppose the reflection effects, are also slightly

increased, with the values of the diffraction coefficient δ_{12} being

0.7479, 0.7563 and 0.7741 for M_o = 0.1, 0.2 and 0.3, respectively,

as compared with 0.7454 for $M_o = M_s$, where δ_{12} is defined as

$$\delta_{12} = \frac{2 \cdot \frac{V_s}{V_o}}{\frac{S_s V_s^2}{S_o V_o^2} + \frac{\beta_s}{\beta_o}} \qquad (5.15b)$$

However, because of the greater distance associated with wing vortices in the outer flow to the slipstream region, the diffracted disturbances in general have smaller effects than the reflected ones, as discussed in Appendix B. Even though Eqs.(5.15) is strictly applicable only in the two-dimensional flow, it can be applied qualitatively to the present three-dimensional case.

The percent increases in the total lift coefficient with a similar definition as given above are 0.52, 2.3 and 6.4, respectively, for M_o = 0.1, 0.2 and 0.3. Again, the increase in C_L due to nonuniformity in Mach numbers is less than expected if the Prandtl-Glauert transformation is used, even though 56.7% of the wing span is immersed in the slipstream.

5.4 Conclusions

Within the assumptions of the linear potential flow theory, the wing-slipstream interaction problem cannot be solved by introducing a single slipstream vortex sheet in an equivalent uniform flow field if the slipstream Mach number is different from the freestream value. Instead, the perturbed flow fields must be solved separately for the slipstream and the outer flow regions and then matched on the slipstream surface to satisfy the boundary conditions. For implementation

of this concept in the computer, two vortex sheets on the slipstream surface have been introduced, one for the slipstream region and the other for the outer flow. This method also renders the introduction of a source sheet unnecessary when the slipstream is at an angle of attack. Comparison with other analytical methods and experiments in incompressible flow showed that the present method is reasonably accurate in predicting the Δc_ℓ, Δc_d and Δc_m distributions. In comparison with experiments, some experimental distributions of slipstream rotational angles have been used in an approximate manner. It is recognized that for accurate prediction of aerodynamic characteristics, more accurate propeller rotational flow with both radial and axial variations is required, as the rotational flow changes the wing local angle of attack. However, for general applications, such precise characteristics of propeller rotational flow have yet to be established by either theoretical or empirical means.

It was also found that nonuniformity in Mach numbers (with higher slipstream Mach number) increased the loading only slightly and to a magnitude much less than that which would have been predicted if the Prandtl-Glauert transformation was applied.

6. Upper-Surface-Blowing Jet—Wing Interaction

6.1 Introduction

The current theory of a thin, jet-flapped wing was first formulated by Spence for a thin airfoil [41,42]. Spence's theory has since been extended to the three-dimensional wing with thin trailing-edge jet flaps. With the jet blowing over the flap, Spence assumed that the thin jet on the flap is "merely to prevent separation, and the pressure distribution is not modified in any other way" [42]. This assumption is reasonable if the jet has zero thickness. However, in the upper-surface blowing STOL configurations of current interest [7, 43], the jet sheet over the wing and flap is expected to be thick because of the use of high-bypass-ratio turbofan engines. The theory of thin trailing-edge jet flaps is not capable of predicting the high induced lift measured in some experiments (See "Discussions" below). This is because the thick jet over the wing surface changes the induced flow in much the same way as the solid ground would do to the wing flow. In other words, the jet which has higher dynamic pressure than the outer flow acts as a soft body which reflects the disturbances back to the wing to induce higher lift. Therefore, ignoring the thick jet effect becomes unrealistic in this application.

In the following, a linear theory for a thick, jet-flapped wing will be formulated, following the general theory of wing-jet interaction presented in Section 4. With this theory, the aerodynamic characteristics of wings of arbitrary aspect ratios with jet interaction can be predicted.

The effects of jet thickness, jet chordwise, spanwise or vertical location, Mach number nonuniformity and jet temperature have been included. The effects of jet deflection are accounted for in a similar manner as has been done by Spence [41]. The basic assumptions are (1) linear and inviscid theory, (2) no jet entrainment, (3) constant jet thickness and velocity and (4) no wing thickness and nacelle.

6.2 Mathematical Formulation

In the present formulation, the jet is assumed to be of rectangular shape located at an arbitrary vertical distance from the wing surface. Therefore, the wing is assumed to be completely in the outer flow even if the jet lower surface may be on the wing upper surface. According to Eqs. (4.10)-(4.12), the boundary conditions to be satisfied for the additional vortex strengths are

$$\frac{\partial \psi_o}{\partial n} - \frac{\partial \psi_s}{\partial n} = -\frac{\vec{U}\cdot\hat{n}(1-\mu')}{\vec{U}\cdot\hat{e}_s} + \frac{\partial \phi_{ws}}{\partial n}(M_j) + \frac{\partial \phi_{wo}}{\partial n}(M_o) \qquad (6.1)$$

$$\frac{\partial \psi_s}{\partial s} - T(\mu')^2 \frac{\partial \psi_o}{\partial s} = -\frac{\partial \phi_{ws}}{\partial s} + T(\mu')^2 \frac{\partial \phi_{wo}}{\partial s} \qquad (6.2)$$

$$\frac{\partial \psi_o}{\partial z} = 0 \qquad \text{(on wing surface)} \qquad (6.3)$$

Again, using the vortex sheets for the jet surface, Eqs. (6.1)-(6.3) can be written in terms of the influence coefficient matrices as follows:

6.2

$$[N_{JW}^{(o)}]\{\gamma_{wa}^{(c)}\} + [N_{JJ}^{(o)}]\{\gamma_{cj}\} - [N_{JJ}^{(i)}]\{\gamma_{ij}\} =$$

On jet
surface
$$\left\{-\frac{\vec{U}\cdot\hat{n}\,(1-\mu')}{\vec{U}\cdot\hat{e}_s} + \frac{\partial\phi_{ws}}{\partial n}(M_j) - \frac{\partial\phi_{wo}}{\partial n}(M_o)\right\} \qquad (6.4)$$

$$[S_{JJ}^{(i)}]\{\gamma_{ij}\} - T(\mu')^2[S_{JW}^{(o)}]\{\gamma_{wa}^{(c)}\} - T(\mu')^2[S_{JJ}^{(o)}]\{\gamma_{cj}\} =$$

$$\left\{-\frac{\partial\phi_{ws}}{\partial s} + T(\mu')^2\frac{\partial\phi_{wo}}{\partial s}\right\} \qquad (6.5)$$

$$[N_{WW}^{(c)}]\{\gamma_{wa}^{(c)}\} + [N_{WJ}^{(c)}]\{\gamma_{cj}\} = \{0\} \qquad (6.6)$$
(on wing surface)

Eqs.(6.4)-(6.6) are written in the form of an augmented matrix

equation and solved in the manner as discussed in Section 4. Some special

features of techniques used in solving Eqs.(6.4)-(6.6) are discussed

below.

(1) That part of the jet which is directly on the wing surface is

assumed to be subjected only to the free stream angle of attack, dis-

regarding whether there is flap deflection or not. The jet deflection

due to Coanda effect will be discussed later and does not change $\vec{U}\cdot\hat{n}$

term in Eq.(6.4). Therefore, the first term on the right hand side of

Eq.(6.4) can be written as, for the jet control points not on the sidewalls,

$$-\frac{\vec{U}\cdot\hat{n}\,(1-\mu')}{\vec{U}\cdot\hat{e}_s} = -[\pm\,(1-\mu')\tan\alpha] \qquad (6.7)$$

where the upper sign is for the upper jet surface. On the other hand,

for the jet sheet behind the trailing edge when the jet is deflected

because of flap deflection, the jet will be subjected to varying angle

of attack due to the continuous changing of the jet sheet curvature.

This curvature distribution is unknown and must be solved simultaneously with the vortex strengths. To avoid iteration, Spence's method [41] can be adopted here in the following way. Since the jet flow is irrotational, it is true that (See Figure 6.1)

$$V_1 \left(R - \tfrac{1}{2} t_j \right) = V_2 \left(R + \tfrac{1}{2} t_j \right) \tag{6.8a}$$

or

$$V_1 - V_2 = \frac{\overline{V_j} \, t_j}{R} \tag{6.8b}$$

where $V_j = (v_1 + v_2)/2$. Note that both v_1 and v_2 are dimensional total jet velocities. Introducing the nondimensional perturbed velocity potential as given by Eq.(4.2), it is seen that

$$V_1 = V_j + \left(\frac{\partial \phi_s}{\partial s} \right)_1 = V_j + V_j \left(\frac{\partial \overline{\phi_s}}{\partial s} \right)_1$$

$$V_2 = V_j + V_j \left(\frac{\partial \overline{\phi_s}}{\partial s} \right)_2$$

and hence,

$$\left(\frac{\partial \overline{\phi_s}}{\partial s} \right)_1 - \left(\frac{\partial \overline{\phi_s}}{\partial s} \right)_2 = \frac{t_j}{R} \tag{6.9}$$
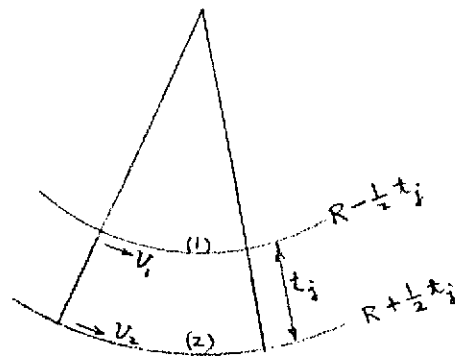
Figure 1.   Geometry Illustrating Irrotationality of a Deformed Jet

Since Eq.(6.2) can be written as

$$\frac{\partial \bar{\phi_s}}{\partial s} = T(\mu')^2 \frac{\partial \bar{\phi_o}}{\partial s} \tag{6.2a}$$

by applying Eq.(6.2a) to the upper and lower surfaces of the jet element, it can be shown that Eq.(6.9) is reduced to

$$T(\mu')^2\left[\left(\frac{\partial \bar{\phi_t}}{\partial s}\right)_1 - \left(\frac{\partial \bar{\phi_t}}{\partial s}\right)_2\right] = \frac{t_j}{R} \tag{6.10}$$

Eq.(10) is seen to be consistent with Spence's results when the thin jet assumption is made. In other words, if $(\partial \bar{\phi_t}/\partial s)_1 - (\partial \bar{\phi_t}/\partial s)_2 = \bar{\gamma_j}$, then the jet vortex strength would be $\bar{\gamma_j} = t_j S_j V_j^2 / R S_\nu V_e^2$, consistent with Eq.(26) of Ref.(41). Assuming that $\bar{\phi}_o = \phi_{wo}(M_o) + \psi_e(M_\nu)$ as has been done in Eq.(4.8), Eq.(6.10) can be reduced to

$$\frac{t_j}{R} = T(\mu')^2\left[\left(\frac{\partial \psi_e}{\partial s}\right)_1 - \left(\frac{\partial \psi_e}{\partial s}\right)_2 + \left(\frac{\partial \phi_{wo}}{\partial s}\right)_1 - \left(\frac{\partial \phi_{wo}}{\partial s}\right)_2\right] \tag{6.11}$$

For convenience, the right hand side of Eq.(6.11) will be denoted by $f(x)$:

$$f(x) = T(\mu')^2\left[\left(\frac{\partial \psi_e}{\partial s}\right)_1 - \left(\frac{\partial \psi_e}{\partial s}\right)_2 + \left(\frac{\partial \phi_{wo}}{\partial s}\right)_1 - \left(\frac{\partial \phi_{wo}}{\partial s}\right)_2\right] \tag{6.12}$$

For small jet deflection, $1/R \cong d^2z/dx^2$. It follows that

$$t_j \frac{d^2z}{dx^2} = f(x)$$

$$\frac{dz}{dx}(T.E.) = -\tan \delta_f \tag{6.13}$$

where δ_f is the flap angle. Eq.(6.13) can be integrated to find the jet slope $\frac{dz}{dx}$ at an arbitrary point. Once $\frac{dz}{dx}$ is obtained, $\hat{n}$ becomes

$$\hat{n} = -\hat{i}\frac{dz}{dx} + \hat{k} \tag{6.14}$$

and

$$\frac{\vec{U} \cdot \hat{n} \, (1-\mu')}{\vec{U} \cdot \hat{e}_s} = \left(\mp \frac{dz}{dx} \pm \tan \alpha \right)(1-\mu') \tag{6.15}$$

where the upper sign is for the upper surface. Notice that $f(x)$ in Eq.(6.12), and hence $\frac{dz}{dx}$, depends on the unknown jet vortices $\{\gamma_{oj}\}$. These terms can be incorporated to the left hand side of Eq.(6.4) before the solution is attempted.

To integrate Eq.(6.13), two methods have been used. The first is the point-slope formula which is the following:

$$\left(\frac{dz}{dx}\right)_{n+1} = \left(\frac{dz}{dx}\right)_n + (\Delta x)_n \left(\frac{d^2z}{dx^2}\right)_n \quad , \quad n=1,2,\cdots \tag{6.16}$$

$$\left(\frac{dz}{dx}\right)_1 = -\tan \delta_f$$

The second method is as follows: Let

$$x = x_t + \frac{c_j}{2}(1 - \cos \theta) \tag{6.17}$$

where c_j is the jet length from the wing trailing edge to be included in the analysis. Then

$$t_j \frac{d^2z}{dx^2} = t_j \frac{d}{d\theta}\left(\frac{dz}{dx}\right)\frac{d\theta}{dx} = f(x),$$

or,

$$t_j \frac{d}{d\theta}\left(\frac{dz}{dx}\right) = \frac{c_j}{2} \sin \theta \, f(x)$$

It follows that

$$t_j \left(\frac{dz}{dx}\right)_i = -t_j \tan \delta_f + \int_0^{\theta_i} \frac{c_j}{2} \sin \theta \, f(x(\theta)) \, d\theta$$

$$\cong -t_j \tan \delta_f + \frac{(\Delta\theta)c_j}{2}\left[\sum_{h=1}^{i-1} \sin \theta_h f(x(\theta_h)) + \frac{1}{2}\sin\theta_i f(x(\theta_i)) \right] \tag{6.18}$$

6.6

where the conventional trapezoidal rule has been used. θ_k's in Eq.(6.18) are seen to be exactly the angles used in defining the jet control points. The second method has been found to be more efficient than the first one.

(2) With the jet on the wing surface, the evaluation of the u-induced velocity, and therefore [S] matrices and $\partial \phi_{w_0}/\partial s$, $\partial \phi_{w_j}/\partial s$ in Eq.(6.5), must be handled carefully. To illustrate this point, consider the expression for u(x,z) for the 2-D case in incompressible flow:

$$u(x,z) = \frac{z}{2\pi} \int_0^1 \frac{\gamma(x')\,dx'}{(x-x')^2+z^2} \qquad (6.19)$$

Observe that for 0<x<1 the integrand in Eq.(6.19) has a second order singularity as z approaches zero while the whole integral will be multiplied by z. As has been checked numerically, Eq.(6.19) can be integrated accurately by the integration technique discussed in Appendix C, if z and the number of integration points are not too small. Since in the present integration technique, just like the conventional VLM, the number of integration points is equal to the number of unknowns to be solved, increasing the number of integration points becomes numerically unrealistic. On the other hand, as has been illustrated in Appendix C, the present technique is quite efficient in treating integrals with Cauchy singularity. Therefore, the best numerical technique under the present circumstances is to rewrite Eq.(6.19) as

$$u(x,z) = \frac{z}{2\pi} \int_0^1 \frac{\gamma(x')-\gamma(x)}{(x-x')^2+z^2}\,dx' + \frac{z}{2\pi}\gamma(x)\int_0^1 \frac{dx'}{(x-x')^2+z^2}$$

$$\cong \frac{z}{4\pi}\frac{\pi}{N}\sum_{k=1}^{N}\frac{\gamma(\theta_k)-\gamma(x)}{(x-x_k)^2+z^2}\sin\theta_k + \frac{z}{2\pi}\gamma(x)\int_0^1\frac{dx'}{(x-x')^2+z^2} \qquad (6.20)$$

The last integral in Eq.(6.20) can be integrated in a close form:

$$\frac{z\,\gamma(x)}{2\pi}\int_0^1 \frac{dx'}{(x-x')^2+z^2} = \frac{\gamma(x)}{2\pi}\left[\tan^{-1}\frac{1-x}{z} + \tan^{-1}\frac{x}{z}\right] \qquad (6.21)$$

Eqs.(6.21) and (6.20) show that u(x,z) becomes γ(x)/2 if z = 0. However, in the three-dimensional case, the corresponding integral is too tedious, if not impossible, to integrate. Therefore, the following numerical method of integration has been selected. The integral in Eq.(6.21) can be integrated accurately by the method illustrated in Appendix C by increasing the number of integration points without changing the number of control points in such a way that the integration points are always interdigitated with the control points (so that they never coincide). Intuitively the number of integration points N can not be arbitrary, instead should be a certain multiple of the number of control points M. The specific relation between the two can be derived as follows. As shown in Appendix C,

$$\frac{T_N'(\cos\theta)}{T_N(\cos\theta)} = \sum_{k=1}^{N} \frac{1}{\cos\theta - \cos\theta_k} \qquad (6.22)$$

where θ_k's are roots of $T_N(\cos\theta_k) = \cos N\theta_k = 0$. If θ is chosen so that $T_N'(\cos\theta) = 0$, then θ and θ_k will never be the same, because the zeros of $T_N(\cos\theta)$ and $T_N''(\cos\theta)$ never coincide. Since $T_N''(\cos\theta) = N\sin N\theta/\sin\theta$ (See Appendix C), it follows that θ should be such that

$$\sin N\theta = 0 \qquad (6.23)$$

By trigonemetric relations, Eq.(6.23) can be written as

$$2\sin\frac{N\theta}{2}\cos\frac{N\theta}{2} = 2\cos\frac{N\theta}{2}\left(2\sin\frac{N\theta}{4}\cos\frac{N\theta}{4}\right) = \cdots = 0 \qquad (6.24)$$

Thus, Eq.(6.23) can be satisfied if $\sin \frac{N\theta}{2^p} = 0$ where p is any integer.
It follows that θ for interdigitation should be such that

$$\frac{N\theta_i}{2^p} = i\pi \tag{6.25}$$

Let $N/2^p = M$, the number of control points. Therefore, the control
points are given by $\theta_i = i\pi/M$, the same as has been found in Appendix C.
With M as the number of control points, the number of integration points
(N) for interdigitation is, therefore,

$$N = 2^p M \tag{6.26}$$

and

$$\int_0^1 \frac{dx'}{(x-x')^2 + z^2} = \frac{1}{2} \int_0^\pi \frac{\sin\theta' \, d\theta'}{(x-x')^2 + z^2} \simeq \frac{1}{2} \frac{\pi}{N} \sum_{k=1}^{N} \frac{\sin\theta_k}{(x-x_k)^2 + z^2} \tag{6.27}$$

As has been checked numerically, the error in numerically integrating
the integral in Eq.(6.21) is less than 1% for p = 3 (i.e., N = 8M),
z = 0.05 and $2 \leq M \leq 5$.

For the three-dimensional case, the above technique is used only
for the integration strip with the control point directly below or above
it. All the other integration strips are reduced to a finite sum by
the method described in Section 4. For the particular strip under con-
sideration, the u-induced velocity, Δu, due to this strip of vortex
distribution is written as

$$\begin{aligned}
\Delta u &= \frac{\beta^2}{4\pi} \int_{x_\ell}^{x_k} \gamma(x') \, \vec{M}_\ell \cdot \hat{\imath} \, dx' \\
&= \frac{\beta^2}{4\pi} \int_{x_\ell}^{x_k} [\gamma(x') - \gamma(x)] \vec{M}_\ell \cdot \hat{\imath} \, dx' + \frac{\beta^2 \gamma(x)}{4\pi} \int_{x_\ell}^{x_k} \vec{M}_\ell \cdot \hat{\imath} \, dx' \\
&\simeq \frac{\beta^2}{4\pi} \frac{c}{2} \frac{\pi}{M} \sum_{k=1}^{M} [\gamma(x_k) - \gamma(x)] \vec{M}_\ell \cdot \hat{\imath} \sin\theta_k \; + \\
&\qquad \frac{\beta^2}{4\pi} \gamma(x) \frac{c}{2} \frac{\pi}{N} \sum_{k=1}^{N} \vec{M}_\ell \cdot \hat{\imath} \sin\theta_k \tag{6.28}
\end{aligned}$$

6.9

The expression for $\vec{M}_\ell \cdot \hat{i}$ is given in Appendix D. For unswept bound vortex distribution, the integral $\int_{x_\ell}^{x_t} \vec{M}_\ell \cdot \hat{i} \; dx'$ can be easily integrated in a closed form. This provides another check case for the accuracy of the present numerical technique. This is done in Appendix E. It may be mentioned that the increase in computing time due to the refinement in computing the u-induced velocity is minimal, but the increase in accuracy is considerable.

(3) When the jet is on the wing surface, some of the jet control points coincide with the wing control points. At these particular jet control points, the sum of the first two terms of Eq.(6.4) would be zero because of Eq.(6.6), i.e.,

$$[N_{Jw}^{(o)}] \{ \gamma_{wa}^{(o)} \} + [N_{JJ}^{(o)}] \{ \gamma_{cj} \} = 0$$

Therefore, if the system of equations is solved by regarding $\{\gamma_{wa}^{(o)}\}$, $\{\gamma_{oj}\}$, $\{\gamma_{jj}\}$ as the unknown vector in that order and process Eq.(6.6) first and then Eqs.(6.4) and (6.5), as has been done in Section 5 for wing-slipstream interaction, difficulty would occur in the solution method. As a simple example, consider the following system of equations:

$$x + 2y = 0 \tag{6.29a}$$

$$x + 2y + z = 1 \tag{6.29b}$$

$$x + y + z = 2 \tag{6.29c}$$

If x and y are to be solved first from Eqs.(6.29a) and (6.29b) in terms of z to be substituted into Eq.(6.29c), great difficulty would be encountered. On the other hand, if z is regarded as the first component of the unknown

solution vector and solve it first, the difficulty would disappear.

Using this concept, the unknowns in Eqs.(6.4)-(6.6) are now solved in

the following order: $\{\gamma_{jj}\}$, $\{\gamma_{oj}\}$ and $\{\gamma_{wa}^{(o)}\}$. Eq.(6.5) is processed first

and then Eqs.(6.4) and (6.6). It appears that this order is also natural

in that the u-induced velocity due to unit vortex strength for the jet

behind the trailing edge is required in computing dz/dx for the trailing

jet when the jet deflection is present (See Eq.(6.11)). This information

can be stored on tape to be used in Eq.(6.4).

6.3 Numerical Results and Discussions

Since no applicable experimental results are available for comparing

detailed aerodynamic characteristics, the computer program was slightly

modified to treat the conventional jet flap with thin and stiff jet

assumptions. By stiff jet, it is meant that $V_j/V_o \rightarrow \infty$ but $V_j^2 t_j$ is finite,

where t_j is the jet thickness. It follows that $\mu = 0$ and the jet flow

is unperturbable. This implies that $\partial\Psi_s/\partial n = 0$ in Eq.(6.1). Furthermore,

Eq.(6.10) gives

$$\left(\frac{\partial\bar{\phi}_o}{\partial s}\right)_1 - \left(\frac{\partial\bar{\phi}_o}{\partial s}\right)_2 = \frac{t_j}{R}\frac{1}{T\mu'^2} \simeq \frac{\rho_j V_j^2 t_j}{\rho_o V_o^2 R} = \frac{c_\mu(y)c}{2}\frac{1}{R} \tag{6.30}$$

where $c_\mu(y)$ is the sectional jet momentum coefficient. To avoid difficulty

with the presence of the jet sidewall vortices, the jet thickness was

assumed to be 5% of the chord length. Das' theory and experiments [44]

were chosen for comparison. To investigate the numerical convergence,

various lengths of the trailing jet sheet were used until a maximum value
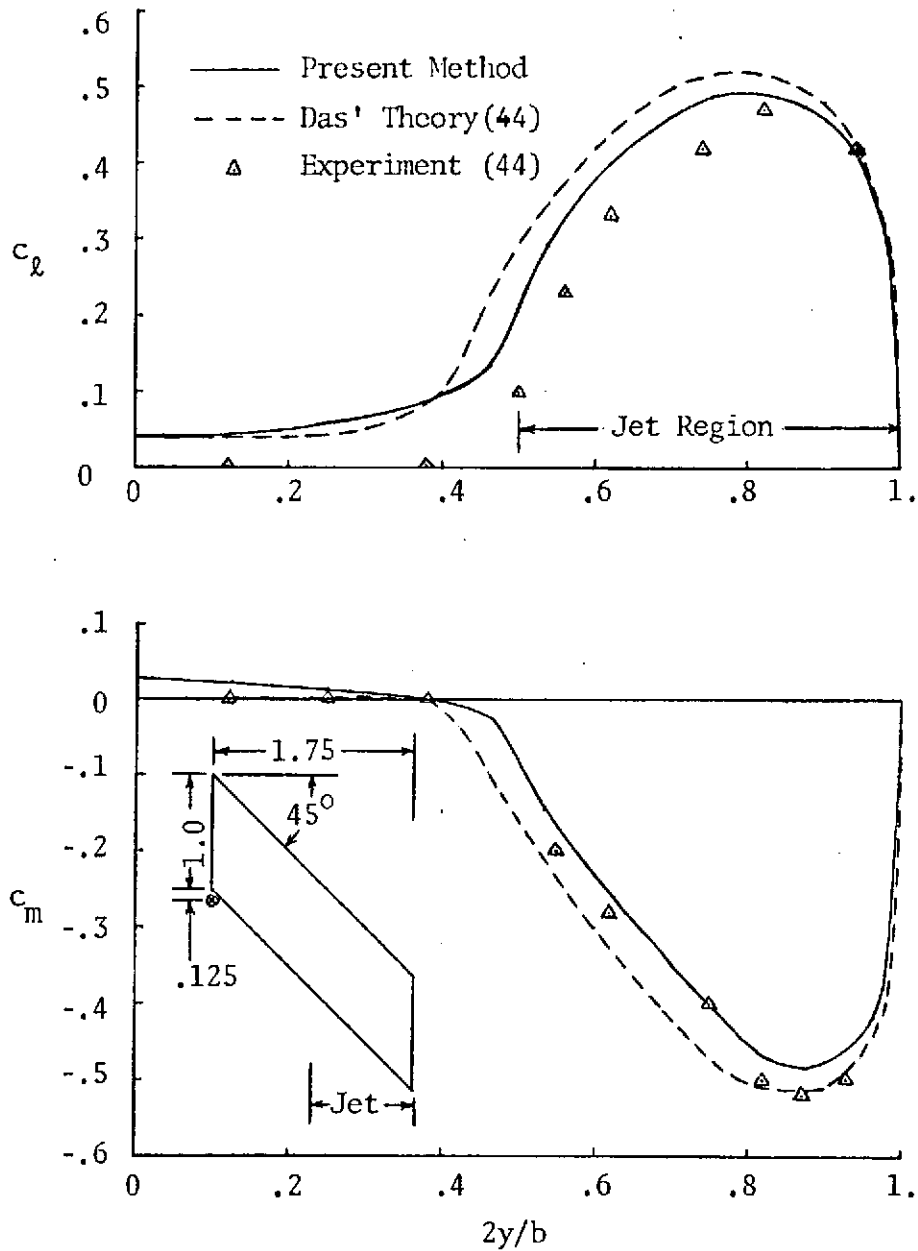
Figure 6.2 Comparison of Aerodynamic Characteristics Predicted by Thin Jet Theories. $\alpha=0^{o}$, $\delta=30^{o}$ and $M_{o}=0$

for the predicted C_L was reached for a given number of streamwise vortices.
It was found that the jet sheet curvature, and therefore the jet vortex
strength, decreases rapidly downstream from the wing trailing edge. The
results for a wing with half semispan blowing with $c_\mu(y) = 1.0$ and $30°$
jet deflection are shown in Figure 6.2. The results indicate the cor-
rectness of the present computer program and the mathematical formulation
for the trailing-edge jet flap.

As the two-dimensional computer program used in Appendix B is
believed to be correct, it is used again here to check the numerical order
of magnitudes of the predicted sectional lift coefficient by the present
3-D program. For this purpose, Phelps' wing planform is used, except
that the leading edge Krueger flap and the trailing edge flap extension
are ignored. This configuration is shown in Figure 6.3. The camber
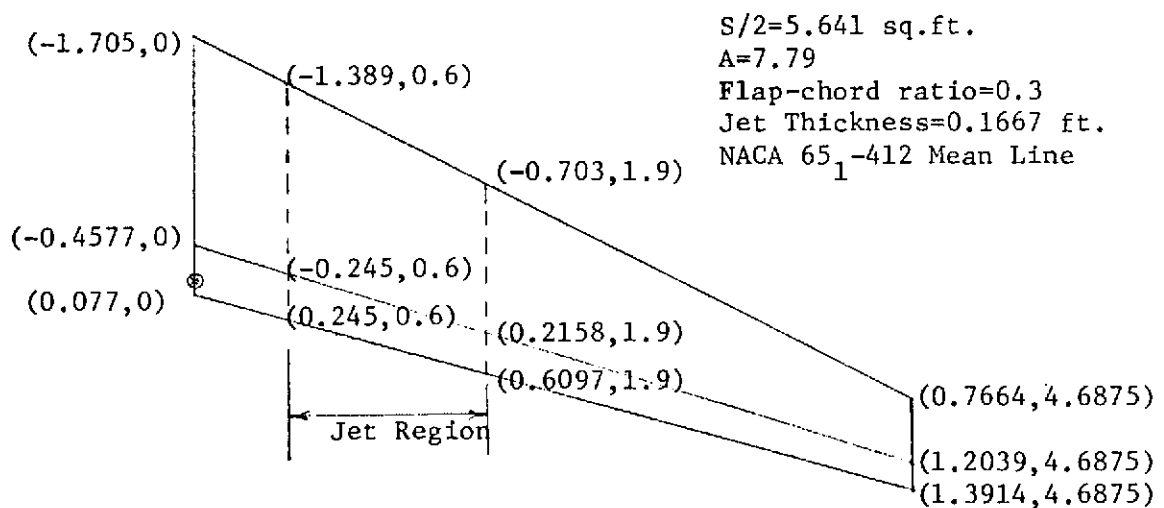
Figure 6.3. Geometry of Wing Planform for Numerical Investigation

and the jet angle of attack are set to zero for the comparison with the 2-D theory. At the spanwise station $2y/b = 0.26667$, the jet thickness ratio t_j/c is 0.1147. For a velocity ratio $V_j/V_o = 5.7314$, the 3-D results show higher lift augmentation(See Table 6.1).Physically, this may be due to the fact that the disturbances diffracted into the jet region have been weakened because of 3-D spreading effect and therefore they become weaker as they are diffracted back to affect the wing flow. According to the 2-D theory (Appendix B), the diffracted disturbances are to decrease the wing lift and therefore, weaker diffracted disturbances would increase the lift.

Table 6.1. Comparison of 2-D and 3-D Jet Lift Augmentation. $\alpha = 10°$, $t_j/c = 0.1147$

	c_ℓ No Jet	c_ℓ With Jet
3-D	0.78876	4.7465
2-D	1.0966	$\{ \begin{matrix} 4.487 \\ 18.5598 \end{matrix}$ (No diffractions)

The experimental results of Ref.7 showed only the total aerodynamic characteristics. To compare with them, the jet velocity would be needed in the present method. This is computed by the momentum theory as follows. The thrust is given by

$$T_r = \rho_j A_j V_j (V_j - V_o)$$ (6.31)

Then,

$$\frac{T_r}{q_e \, S/2} \, \frac{S/2}{A_j} \; = \; 2\left(\frac{\rho_j}{\rho_0}\right)\left(\frac{V_j}{V_0}\right)\left[\left(\frac{V_j}{V_0}\right) - 1\right]$$

or,

$$\frac{C_\mu \, (S/2)}{2 \, A_j \, (\rho_j/\rho_0)} \; = \; \left(\frac{V_j}{V_0}\right)^2 - \left(\frac{V_j}{V_0}\right)$$

Solving for V_j/V_0 , it is found that

$$\frac{V_j}{V_0} \; = \; \frac{1}{2}\left\{ 1 + \left[1 + \frac{2\, C_\mu \, (S/2)}{A_j \, (\rho_j/\rho_0)} \right]^{1/2} \right\} \qquad\qquad (6.32)$$

For the jet thickness of 2 inches (0.1667 ft), A_j = 0.2167 sq. ft.
The half wing area used by Phelps, et al, in computing the thrust coef-
ficient C_μ was 5.61 sq. ft. Using this information, Eq.(6.32) gives
V_j/V_0 = 5.7314 for C_μ = 2.095 and $\rho_j = \rho_0$.

Another difficulty must be solved before the comparison with experi-
mental results can be made. As the flap is deflected, the jet will
follow the flap surface due to the Coanda effect. The Coanda effect is
due to the high suction on the flap surface to attract the jet downward.
It exists also under wind-off conditions. Since this effect can be explained
only by the viscous theory, its exact prediction is out of scope of the
present investigation. For the present purpose, it will be estimated
in accordance with the momentum theory. As illustrated in Figure 6.4,
when the jet is deflected at the flap knee, a jet reaction F_j equal to
$2\, \rho_j \, A_j \, V_j^2 \, \sin(\delta_f/2)$ on one side of the wing will be produced. Its
lift and drag components are therefore

$$L_r = 2\,\rho_j A_j\,V_j^2 \sin(\delta_f/2)\cos(\delta_f/2 + \alpha) \tag{6.33}$$

$$D_r = 2\,\rho_j A_j V_j^2 \sin(\delta_j/2)\sin(\delta_f/2 + \alpha) \tag{6.34}$$

In coefficient form, they become

$$C_{L_r} = 4\,\frac{\rho_j}{\rho_o}\,\frac{1}{\mu^2}\,\frac{A_j}{S/2}\,\sin(\delta_f/2)\cos(\delta_f/2 + \alpha) \tag{6.35}$$

$$C_{D_r} = 4\,\frac{\rho_j}{\rho_o}\,\frac{1}{\mu^2}\,\frac{A_j}{S/2}\,\sin(\delta_f/2)\sin(\delta_f/2 + \alpha) \tag{6.36}$$

Under wind-off conditions, Eq. (6.33) gives $L_r = T_r \sin \delta_f$ which is consistent with the equation given Glahn [45]. However, the expression for D_r suggested by Glahn is $D_r = T_r \sin \delta_f \tan \delta_f$, while Eq. (6.34) would give $D_r = 2T \sin^2 (\frac{\delta_f}{2})$.
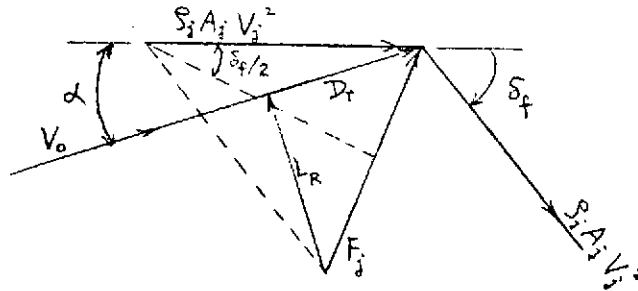
Figure 6.4. Coanda Effect

For $\delta_f = 30°$, $\alpha = 5°$ and $\rho_0 = \rho_j$, Eq.(6.35) gives the Coanda lift coefficient as 1.2277. The aerodynamically induced lift increment $(\Delta C_L)_i$ which is the difference between the augmented lift coefficient without the Coanda effect and the wing alone case, is plotted in Figure 6.5 with respect to the jet leading edge location. The jet exit in Ref. 7 is estimated to be at 1/3 of the wing chord (excluding the flap) from the leading edge. That is, $(x_{j\ell} - x_\ell)/c = 0.7 \times 1/3 = 0.233$. From Figure 6.5, $(\Delta C_L)_i$ is found to be 1.8. Therefore, the total lift incre-ment is $\Delta C_L = 3.0277 (=1.8 + 1.2277)$. This compares favorably with 2.9 from Figure 12 of Ref. 7. From Figure 6.5, it is also seen that the trailing-edge jet alone will not produce enough lift to match the measured value. Since the present method gives only the induced drag, while the experimental results included all drag components, the drag computa-tion is not compared. The experimental pitching moment is directly affected by the thrust effect, because the engines are above the moment center. Besides, the Krueger flap and the flap extension may also affect the change in the pitching moment. Therefore, the pitching moment has not been compared. In Figure 6.5, the predicted span loading has also been shown. The incremental loading is seen to be concentrated in the jet region. The higher c_ℓ near the jet boundary is probably due to the jet sidewall effect which allows the diffracted disturbances in the jet region to leak out through the sidewall so as to reduce their effect on the wing flow and also due to the increase in the jet thickness/chord ratio outboard. In reality, the loading will probably fair more smoothly
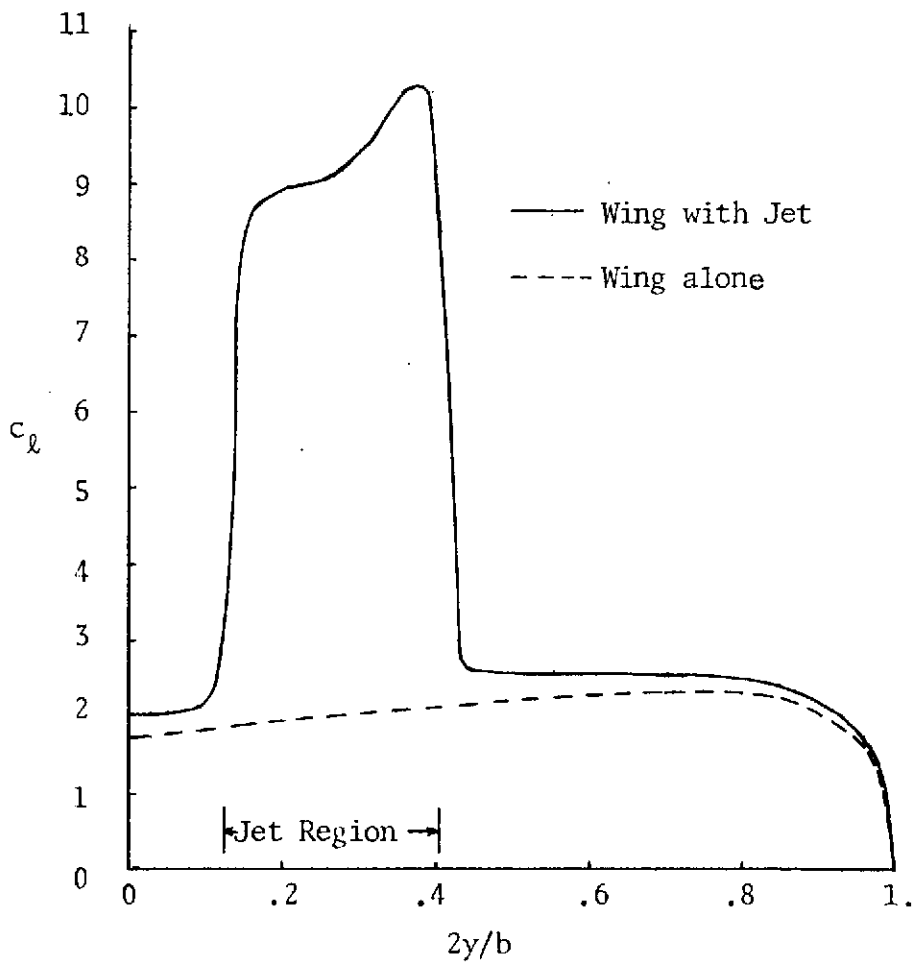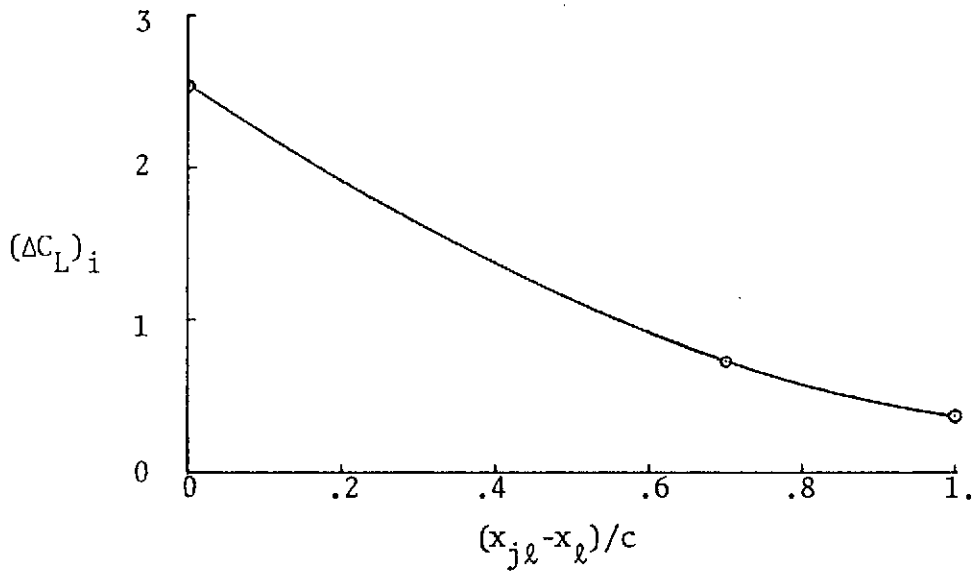
Figure 6.5 Aerodynamic Characteristics for the Configuration
of Figure 6.3. $\delta_f = 30°$, $\alpha = 5°$, $M_o = M_j = 0$

into the outside region because of the jet sideward spreading effect and the turbulent mixing.

Putting $\delta_f = 0$, additional data are generated for the configuration of Figure 6.3 for the effects of the jet vertical location "h" on the aerodynamic characteristics. Table 6.2 shows the change in the total aerodynamic characteristics at three heights. The rapid change in C_L and C_{Di} with jet height seems to confirm the 2-D results of Appendix B.

Table 6.2. Change in Aerodynamic Characteristics
due to Vertical Shift of Jet Location.
$V_j/V_o = 5.7314$, $\alpha = 5°$, $M_o = M_j = 0$

h,ft.	h/t_j	ΔC_L	ΔC_{Di}	$\dfrac{\Delta X_{c.p.}}{\bar{c}}$
0	0	0.7484	0.04715	-0.1417
0.07	0.42	0.1545	0.01357	-0.07298
0.15	0.90	0.0487	0.0057	-0.01156

The appropriate parameter here is the height/thickness ratio, or h/t_j. Large velocity ratio V_j/V_o tends to increase the rate of decrease in ΔC_L with respect to h/t_j. Also, the aerodynamic jet interaction is to shift the center of pressure forward. Note that this does not include the effect of the Coanda jet reaction when $h = 0$. This shift in the center of pressure is also evidenced in the pressure plot of Figure 6.6. The span loading and the induced drag distribution are compared in
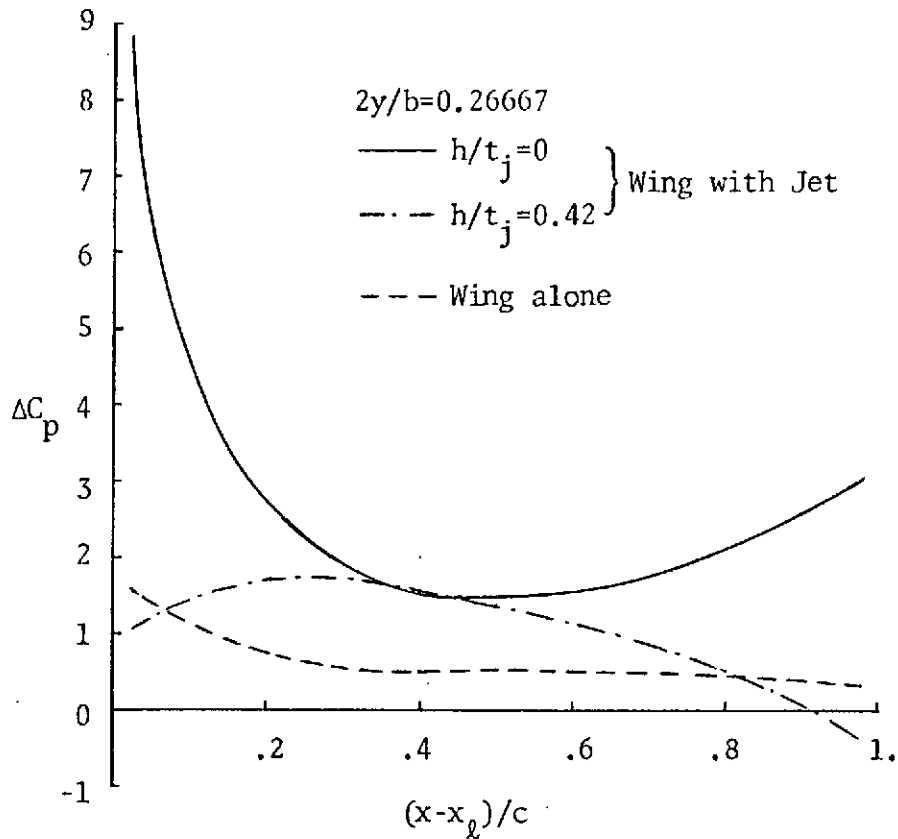
Figure 6.6 Comparison of Pressure Distribution for Different

Jet Heights. $\alpha=5^{\circ}$, $\delta_f=0^{\circ}$, $M_o=M_j=0$
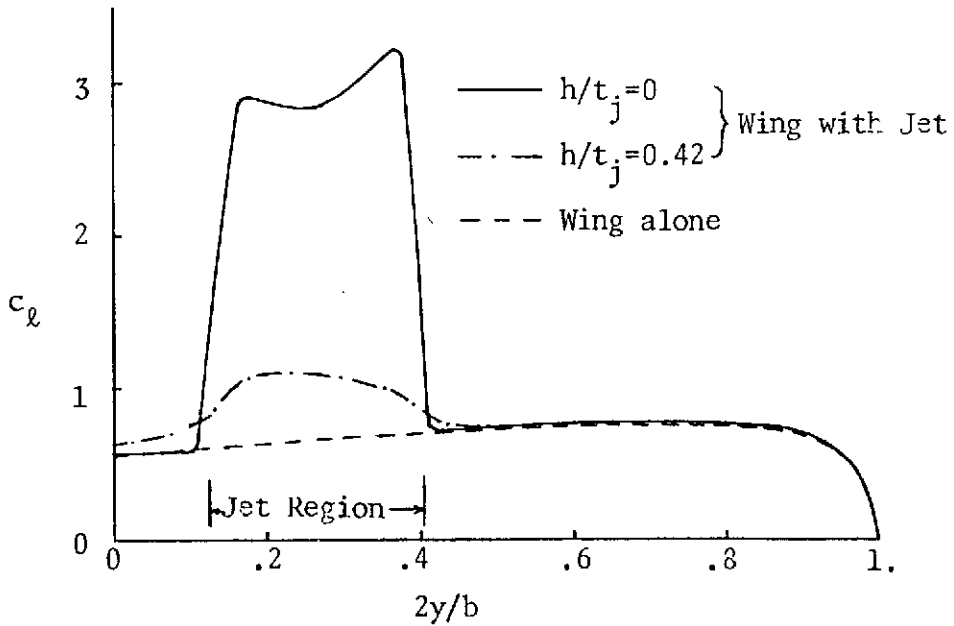
Figure 6.7 Comparison of Aerodynamic Characteristics for

Different Jet Heights. $\alpha=5^{\circ}$, $\delta_f=0$, $M_o=M_j=0$

Figure 6.7. Figure 6.8 shows the effects of mach number nonuniformity

on the span loading. The jet mach number is computed by the relation:

$$M_j^2 = M_o^2 \left(\frac{V_j}{V_o} \right)^2 \left(\frac{S_j}{S_o} \right)$$
(6.37)

and $T = \rho_o/\rho_j$. The general trend is similar to that predicted by the

2-D theory. That is, higher jet mach number produces higher lift and

high jet temperature tend to degrade the lift capability.

As a final item for discussion, it is of interest to note that Eq.(6.1)

shows that when the jet is subject to an angle of attack, a source dis-

tribution would be required on the jet lower surface where $\hat{n} = -\hat{k}$; while

on the upper surface a sink distribution would be needed. Since the

jet lower surface is closer to the wing, the net result is a reduction

in lift because the source distribution produces a net downwash on the

wing. This observation has been checked out numerically on the computer.

This interaction characteristics may have the following effect. As the

wing is subject to a positive roll rate, the right wing will see an

increase in angle of attack, thus increasing the lift. However, the

increase in angle of attack for the jet will reduce the lift as discussed

above. The net effect must be checked to see how the roll damping

derivative C_{ℓ_p} will be affected. Similar remarks are also applicable to

the pitch damping derivative C_{mq}. This effect has not been investigated

in the present study.

In the above numerical investigation, a typical computer run required

33 K (decimal) of memory, 5.5 minutes of processing time (6 min. with Mach

number nonuniformity) with Honeywell 635 computer solving 198 unknowns.

One tape is needed.
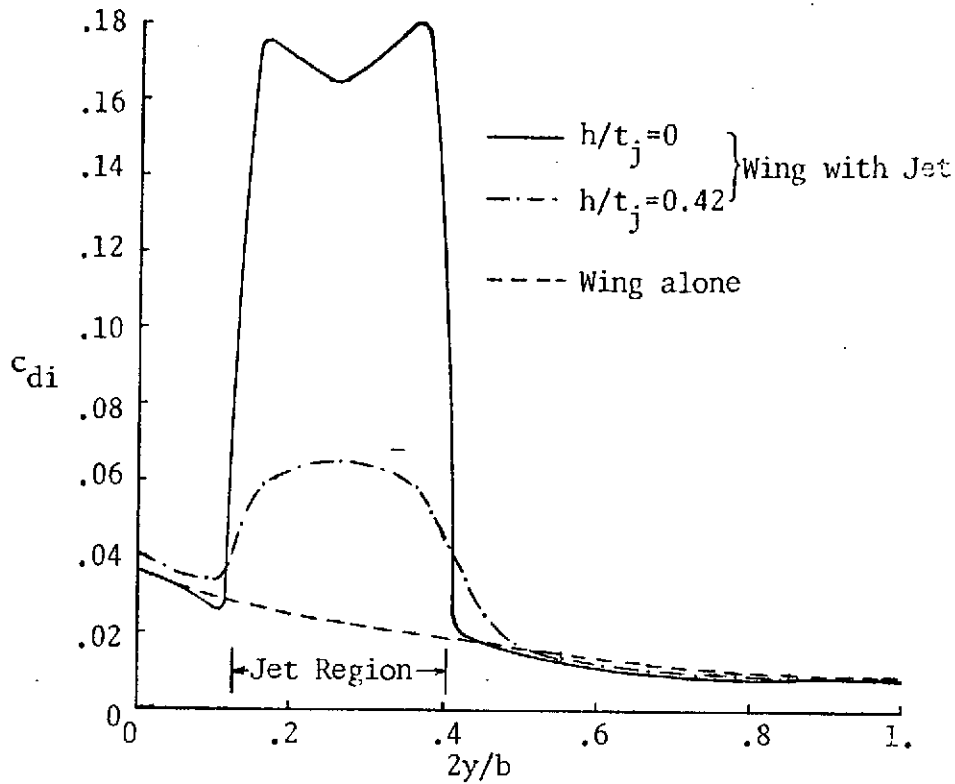
Figure 6.7 Concluded
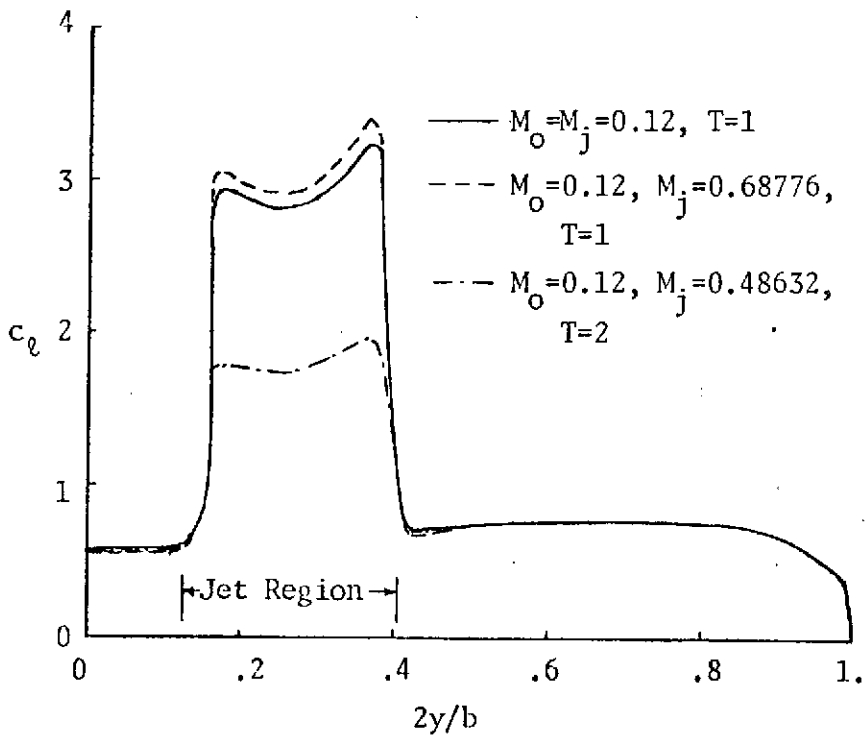
Figure 6.8 Effects of Mach Number Nonuniformity on Span

Loading. $\alpha=5^{\circ}$, $\delta_f=0$

7. References

1. Schumacher, H. E. and Trent, W. C., "Significant Considerations in the Development of Engine/Airframe Systems for High Performance Aircraft," MCAIR 72-042, 1972, McDonnell Aircraft Co.

2. Kutney, J. T., "Airframe/Propulsion System Integration Analysis Using the Propulsion Simulator Technique," Paper No. 16 in "Aerodynamic Interference," AGARD CP-71-71.

3. Aldridge, S. E. and Nye, J. L., "Experimental Results of High Bypass Ratio Turbofan and Wing Aerodynamic Interference," Paper No. 23 in "Aerodynamic Interference," AGARD CP-71-71.

4. Welge, H. R. and Ongarato, J. R., "Powered Engine Simulator Procedures and Experience for the DC-10 Wing Engine," Journal of Aircraft, Vol. 8, No. 7, July 1971, pp. 523-529.

5. Raney, D. J., Kurn, A. G. and Bagley, J. A., "Wind Tunnel Investigation of Jet Interference for Underwing Installation of High Bypass Ratio Engines," Aeronautical Research Council of Great Britain, CP No. 1044, 1968.

6. Bagley, J. A., "Some Experiments on an Engine Installation Above the Wing of a Swept-Winged Aircraft," Paper No. 5 in "Aerodynamic Interference Between Aircraft and Engine Jet," DLR-MITT-70-28, April 1971.

7. Phelps, A. E., Letko, W. and Henderson, R. L., "Preliminary Low-Speed Wind-Tunnel Investigation of a Semispan STOL Jet Transport Wing-Body with an Upper-Surface Blown Jet Flap," NASA TN D-7183, May 1973.

8. Ribner, H. S., "Field of Flow About a Jet and Effect of Jets on Stability of Jet-Propelled Airplanes," NACA Wartime Report ACR No. L6C13, April 1946.

9. Squire, H. B., "Jet Flow and its Effects on Aircraft," Aircraft Engineering, Vol. 22, March 1950, pp. 62-67.

10. Mendenhall, M. R., Dillenius, M. F. E. and Spangler, S. B., "Calculation of Aerodynamic Characteristics of STOL Aircraft with Externally-Blown Jet-Augmented Flaps," AIAA Paper No. 72-63, 1972.

11. (a) Shollenberger, C. A., "Analysis of the Interaction of Jets and Airfoils in Two Dimensions," Journal of Aircraft, Vol. 10, No. 5, May 1973, pp. 267-273.

11. (b) Shollenberger, C. A., "A Three-Dimensional Wing/Jet Interaction
    Analysis Including Jet Distortion Influences," AIAA Paper No.
    73-655.

12. Koning, C., "Influence of the Propeller on Other Parts of the Airplane
    Structure," in Vol. IV of "Aerodynamic Theory," Edited by W. F.
    Durand, Dover Publications.

13. Ferrari, C., "Propeller and Wing Interactions at Subsonic Speeds,"
    p. 364, "Aerodynamic Components of Aircraft at High Speeds,"
    Edited by A. F. Conovan and H. R. Lawrence, Princeton University
    Press, 1957.

14. Rethorst, S., "Aerodynamics of Nonuniform Flows as Related to an
    Airfoil Extending through a Circular Jet," Journal of the Aero-
    nautical Sciences, Vol. 25, No. 1, Jan. 1958, pp. 11-28.

15. Jameson, A., "Analysis of Wing Slipstream Flow Interaction," NASA CR-
    1632, 1970.

16. Ribner, H. S. and Ellis, N. D., "Theory and Computer Study of a Wing
    in a Slipstream," AIAA Paper No. 66-466, 1966.

17. Ellis, N. D., "Aerodynamics of Wing-Slipstream Interaction: A Numerical
    Study," UTIAS Report No. 169, Institute for Aerospace Studies,
    University of Toronto, Oct. 1971. Also, Ribner, H. S. and Ellis,
    N. D., "Aerodynamics of Wing-Slipstream Interaction," CASI Trans-
    actions, Vol. 5, Sept. 1972, pp. 56-63.

18. Levinsky, E. S., Thommen, H. U., Yager, P. M. and Holland, C. H.,
    "Lifting-Surface Theory for V/STOL Aircraft in Transition and
    Cruise,"
    Part I. Journal of Aircraft, Vol 6, No 6, Nov-Dec, 1969, pp.488-495.
    Part II. Journal of Aircraft, Vol 7, No 1, Jan-Feb, 1970, pp. 58-65.

19. Kleinstein, G. and Liu, C. H., "Application of Airfoil Theory for
    Nonuniform Streams to Wing Propeller Interaction," Journal of
    Aircraft, Vol 9, No 2, Feb 1972, pp. 137-142.

20. Ting, L., Liu, C. H. and Kleinstein, G., "Interference of Wing and
    Multipropellers," AIAA Journal, Vol 10, No 7, July 1972, pp.906-914.

21. Purcell, E. W., "The Vector Method of Solving Simultaneous Linear
    Equations," Journal of Math. Physics, Vol 23, 1953, pp. 180-183.

22. Luke, Y. L., "The Special Functions and Their Approximations," Vol II,
    Chapter XV, Acad. Press, 1969.

23. Brenckmann, M. E., "Experimental Investigation of the Aerodynamics of a Wing in a Slipstream," Journal of the Aeronautical Sciences, Vol 25, No 5, May 1958, pp. 324-328.

24. Graham, E. W., et al., "A Preliminary Theoretical Investigation of the Effects of Propeller Slipstream on Wing Lift," Rept. SM-14991, 1953, Douglas Aircraft Co.

25. Nishimura, Y., "An Experimental Investigation by Force and Surface Pressure Measurements of a Wing Immersed in a Propeller Slip-stream," National Aeronautical Establishment, Natl. Research Council of Canada.
    Part I. Force and Moment Measurements, LR-501, March 1968.
    Part II. Surface Pressure Measurements, LR-525, June 1969.

26. Abbott, I. H. and von Doenhoff, A. E., "Theory of Wing Sections," Dover Publications, p. 114.

27. Kálmán, T. P., Giesing, J. P. and Rodden, W. P., "Spanwise Distribution of Induced Drag in Subsonic Flow by the Vortex Lattice Method," Journal of Aircraft, Vol 7, No 6, Nov-Dec., 1970, pp. 574-576.

28. Ward, G. N., "Linearized Theory of Steady High-Speed Flow," Cambridge University Press, 1955.

29. Maskew, B., "Calculation of the Three-Dimensional Potential Flow Around Lifting Non-Planar Wings and Wing-Bodies Using a Surface Distribution of Quadrilateral Vortex-Rings," Report TT 7009, Dept. of Transport Technology, Loughborough Univ. of Technology, U. K., Sept. 1970.

30. Ting, L. and Liu, C. H. "Thin Airfoil in Nonuniform Parallel Streams," Journal of Aircraft, Vol 6, No 2, Mar-Apr 1969, pp. 173-175.

31. Ting, L. and Liu, C. H., "Thin Airfoil in Non-Uniform Parallel Streams," NYU-AA-68-20, Dept. of Aeronautics and Astronautics, New York Univ., July 1968.

32. Margason, R. J. and Lamar, J. E., "Vortex-Lattice Fortran Program for Estimating Subsonic Aerodynamic Characteristics of Complex Planforms," NASA TN D-6142, Feb. 1971.

33. Giesing, J. P., "Lifting Surface Theory for Wing-Fuselage Combinations," Douglas Aircraft Co., Report DAC-67212, Vol 1, Aug 1968.

34. Hancock, G. J., "Comment on 'Spanwise Distribution of Induced Drag in Subsonic Flow by the Vortex Lattice Method'," Journal of Aircraft, Vol 8, No 8, Aug, 1971, p. 681.

35. James, R. M., "On the Remarkable Accuracy of the Vortex Lattice
    Discretization in Thin Wing Theory," Douglas Aircraft Co.,
    Report No DAC-67211, Feb 1969.

36. Lan, C. and Roskam, J., "Leading Edge Force Features of the Aero-
    dynamic Finite Element Method," Journal of Aircraft, Vol 9,
    No 12, Dec 1972, pp. 864-867.

37. Garner, H. C., Hewitt, B. L. and Labrujere, T. E., "Comparison of
    Three Methods for the Evaluation of Subsonic Lifting-Surface
    Theory," Aeronautical Research Council of Great Britain, Reports
    and Memoranda No. 3597, June 1968.

38. Multhopp, H., "Methods for Calculating the Lift Distribution of Wings
    (Subsonic Lifting-Surface Theory)," Aeronautical Research Council
    of Great Britain, Reports and Memoranda No. 2884, Jan 1950.

39. Lamar, J. E., "A Modified Multhopp Approach for Predicting Lifting
    Pressures and Camber Shape for Composite Planforms in Subsonic
    Flow," NASA TN D-4427, July 1968.

40. Wagner, S., "On the Singularity Method of Subsonic Lifting-Surface
    Theory," Journal of Aircraft, Vol 6, No 6, Nov-Dec 1969, pp.
    549-558.

41. Spence, D. A., "The Lift Coefficient of a Thin, Jet-Flapped Wing",
    Proc. Roy. Soc. A., Vol. 238, pp. 46-68, 1956.

42. Spence, D. A., "The Lift on a Thin Aerofoil with a Jet-Augmented
    Flap", Aeronautical Quarterly, Vol. 9, pp. 287-299, August 1958.

43. Phelps, A. E. III, "Aerodynamics of the Upper Surface Blown Flap",
    in "STOL Technology" NASA SP-320, 1972.

44. Das, A., "Theoretische und Experimentelle Untersuchungen an Tragflügeln
    endlicher Spanweite mit Strahlklappen", Abhandlungen der Braun-
    schweigischen Wissenschaftlichen Gesellschaft, Band XVII, 1965.

45. von Glahn, Uwe H., "Use of the Coanda Effect for Obtaining Jet Deflection
    and Lift with a Single Flat-Plate Deflection Surface", NACA TN-
    4272, June 1958.

APPENDIX A

Derivation of Induced Velocities Due To A
General Vortex Segment in Linearized Compressible Flow

The velocity field due to a line segment of vortex of strength Γ

is (p. 43 of Ref. 28)

$$\vec{q}_1(\vec{R}) = \frac{\beta^2 \Gamma}{4\pi} \int_L \frac{(\vec{R}_1 - \vec{R}) \times d\vec{\ell}}{R_\beta^3} \tag{1}$$

where

$$R_\beta^2 = (x - x')^2 + \beta^2 (y - y')^2 + \beta^2 (z - z')^2 \tag{2}$$

Define a parameter τ such that

$$\vec{R}_1 - \vec{R} = \vec{a} + \tau \vec{\ell} \tag{3}$$

For the geometry, see Fig. 4.1. It follows that

$$\begin{aligned}
x' - x &= x_1 - x + \tau(x_2 - x_1) \\
y' - y &= y_1 - y + \tau(y_2 - y_1) \\
z' - z &= z_1 - z + \tau(z_2 - z_1)
\end{aligned} \tag{4}$$

Therefore, R_β^2 can be written as

$$
\begin{aligned}
R_\beta^2 &= (x_1 - x)^2 + \tau^2 (x_2 - x_1)^2 + 2(x_1 - x)(x_2 - x_1)\tau + \\
&\quad \beta^2 \left[(y_1 - y)^2 + \tau^2 (y_2 - y_1)^2 + 2(y_1 - y)(y_2 - y_1)\tau \right] + \\
&\quad \beta^2 \left[(z_1 - z)^2 + \tau^2 (z_2 - z_1)^2 + 2(z_1 - z)(z_2 - z_1)\tau \right] \\
&= \tau^2 \left[(x_2 - x_1)^2 + \beta^2 (y_2 - y_1)^2 + \beta^2 (z_2 - z_1)^2 \right] + \\
&\quad 2\tau \left[(x_1 - x)(x_2 - x_1) + \beta^2 (y_1 - y)(y_2 - y_1) + \beta^2 (z_1 - z) \cdot \right. \\
&\quad \left. (z_2 - z_1) \right] + (x_1 - x)^2 + \beta^2 (y_1 - y)^2 + \beta^2 (z_1 - z)^2 \\
&= \tau^2 \bar{A} + \tau \bar{B} + \bar{C}
\end{aligned} \tag{5}
$$

Substituting Eq.(5) into Eq.(1), it is found that

$$
\begin{aligned}
\vec{q}_1(\vec{R}) &= \frac{\beta^2 \Gamma}{4\pi} \, \vec{a} \times \vec{\ell} \int_0^1 \frac{d\tau}{[\bar{A}\tau^2 + \bar{B}\tau + \bar{C}]^{3/2}} \\
&= \frac{\beta^2 \Gamma}{4\pi} \, \vec{a} \times \vec{\ell} \left\{ -\frac{2(2\bar{A}\tau + \bar{B})}{(\bar{B}^2 - 4\bar{A}\bar{C})[\bar{A}\tau^2 + \bar{B}\tau + \bar{C}]^{1/2}} \right\} \Bigg|_0^1
\end{aligned}
$$

$$= \frac{\beta^2 \Gamma}{4\pi} \vec{a} \times \vec{\ell} \left\{ \frac{2\bar{B}}{(\bar{B}^2 - 4\bar{A}\bar{C})\sqrt{\bar{C}}} - \frac{2(2\bar{A} + \bar{B})}{(\bar{B}^2 - 4\bar{A}\bar{C})\sqrt{\bar{A} + \bar{B} + \bar{C}}} \right\}, \qquad (6)$$

$$\bar{B}^2 - 4\bar{A}\bar{C} \neq 0.$$

Now,

$$\bar{B}^2 - 4\bar{A}\bar{C} = 4\left[(x_1 - x)(x_2 - x_1) + \beta^2(y_1 - y)(y_2 - y_1) + \beta^2(z_1 - z)(z_2 - z_1) \right]^2$$
$$- 4\left[(x_2 - x_1)^2 + \beta^2(y_2 - y_1)^2 + \beta^2(z_2 - z_1)^2 \right]\left[(x_1 - x)^2 + \beta^2(y_1 - y)^2 + \beta^2(z_1 - z)^2 \right]$$

$$= 4\beta^2(x_2 - x_1)(y_1 - y)\left[-(x_2 - x_1)(y_1 - y) + (x_1 - x)(y_2 - y_1) \right] +$$
$$4\beta^2(x_1 - x)(y_2 - y_1)\left[(x_2 - x_1)(y_1 - y) - (x_1 - x)(y_2 - y_1) \right] +$$
$$4\beta^2(x_2 - x_1)(z_1 - z)\left[(x_1 - x)(z_2 - z_1) - (x_2 - x_1)(z_1 - z) \right] +$$
$$4\beta^2(x_1 - x)(z_2 - z_1)\left[(x_2 - x_1)(z_1 - z) - (x_1 - x)(z_2 - z_1) \right] +$$
$$4\beta^2(y_2 - y_1)(z_1 - z)\left[(y_1 - y)(z_2 - z_1) - (y_2 - y_1)(z_1 - z) \right] +$$
$$4\beta^2(z_2 - z_1)(y_1 - y)\left[(y_2 - y_1)(z_1 - z) - (z_2 - z_1)(y_1 - y) \right]$$

$$= -4\beta^2 \left\{ \left[(x_2 - x_1)(y_1 - y) - (x_1 - x)(y_2 - y_1) \right]^2 + \right.$$
$$\left[(x_2 - x_1)(z_1 - z) - (x_1 - x)(z_2 - z_1) \right]^2 +$$
$$\left. \beta^2 \left[(y_2 - y_1)(z_1 - z) - (z_2 - z_1)(y_1 - y) \right]^2 \right\}$$

It follows that

$$\bar{B}^2 - 4\bar{A}\bar{C} = -4 \left| \vec{a}' \times \vec{\ell}' \right|^2 \qquad (7)$$

where

$$\vec{a}' = (x_1 - x)\hat{i} + \beta(y_1 - y)\hat{j} + \beta(z_1 - z)\hat{k} \qquad (8)$$

$$\vec{\ell}' = (x_2 - x_1)\hat{i} + \beta(y_2 - y_1)\hat{j} + \beta(z_2 - z_1)\hat{k} \qquad (9)$$

From Eq.(5),

$$\bar{B} = 2\left[(x_1 - x)(x_2 - x_1) + \beta^2(y_1 - y)(y_2 - y_1) + \beta^2(z_1 - z)(z_2 - z_1) \right]$$
$$= 2\vec{a}' \cdot \vec{\ell}' \qquad (10)$$

$$\bar{C} = (x_1 - x)^2 + \beta^2(y_1 - y)^2 + \beta^2(z_1 - z)^2$$
$$= |\vec{a}'|^2 \qquad (11)$$

$$\bar{A} = (x_2 - x_1)^2 + \beta^2(y_2 - y_1)^2 + \beta^2(z_2 - z_1)^2$$
$$= |\vec{\ell}'|^2 \qquad (12)$$

$$2\bar{A} + \bar{B} = 2\left\{(x_2-x_1)(x_2-x) + \beta^2(y_2-y_1)(y_2-y) + \beta^2(z_2-z_1)(z_2-z)\right\}$$

$$= 2\,\vec{b}' \cdot \vec{\ell}' \tag{13}$$

$$\bar{A} + \bar{B} + \bar{C} = |\vec{\ell}'|^2 + 2\,\vec{a}' \cdot \vec{\ell}' + |\vec{a}'|^2$$

$$= |\vec{\ell}' + \vec{a}'|^2 = |\vec{b}'|^2 \tag{14}$$

Hence, Eq.(6) becomes

$$\vec{q}_1(\vec{R}) = \frac{\beta^2 \Gamma}{4\pi} \frac{\vec{a} \times \vec{\ell}}{|\vec{a}' \times \vec{\ell}'|^2} \left\{ \frac{\vec{b}'}{|\vec{b}'|} - \frac{\vec{a}'}{|\vec{a}'|} \right\} \cdot \vec{\ell}' \tag{15}$$

Eq.(15) can be recast to a different form without involving $\vec{\ell}$ and $\vec{\ell}'$.

Since $\vec{\ell} = \vec{b} - \vec{a}$, and $\vec{\ell}' = \vec{b}' - \vec{a}'$, it can be shown that

$$\frac{\vec{a} \times \vec{\ell}}{|\vec{a}' \times \vec{\ell}'|^2} = \frac{\vec{a} \times \vec{b}}{|\vec{a}' \times \vec{b}'|^2}$$

$$\frac{\vec{b}' \cdot \vec{\ell}'}{|\vec{b}'|} - \frac{\vec{a}' \cdot \vec{\ell}'}{|\vec{a}'|} = \frac{\vec{b}' \cdot (\vec{b}' - \vec{a}')}{|\vec{b}'|} - \frac{\vec{a}' \cdot (\vec{b}' - \vec{a}')}{|\vec{a}'|}$$

$$= |\vec{b}'| + |\vec{a}'| - \vec{a}' \cdot \vec{b}' \left(\frac{|\vec{a}'| + |\vec{b}'|}{|\vec{a}'||\vec{b}'|} \right)$$

$$= \left[|\vec{a}'| + |\vec{b}'| \right] \left[1 - \frac{\vec{a}' \cdot \vec{b}'}{|\vec{a}'||\vec{b}'|} \right]$$

Eq.(15) becomes

$$\vec{q}_1(\vec{R}) = \frac{\beta^2 \Gamma}{4\pi} \frac{\vec{a} \times \vec{b}}{|\vec{a}' \times \vec{b}'|^2} \left[|\vec{a}'| + |\vec{b}'| \right] \left[1 - \frac{\vec{a}' \cdot \vec{b}'}{|\vec{a}'||\vec{b}'|} \right] \tag{16}$$

In incompressible flow, $\beta = 1$. In this special case, Eq.(16) becomes the expression used by Maskew [29].

For the induced flow field due to the trailing vortices, Eq.(1) must be used, where L now starts from the bound vortex position x_s to ∞. Thus, the induced velocity due to one trailing vortex on one side of a bound vortex is given by

$$\vec{q}_2(\vec{R}) = \frac{\beta^2 \Gamma}{4\pi} \int_{x_s}^{\infty} \frac{(\vec{R}_1 - \vec{R}) \times d\vec{\ell}}{R_\beta^3} \tag{17}$$

APPENDIX B

Compressibility Effects on Airfoil-Jet Interaction

1. Mathematical Formulation

Since the general three-dimensional problem is much more dif-
ficult to analyze for the Mach number effect, a two-dimensional an-
alysis for airfoil-jet interaction is first undertaken. A plane jet
with Mach number M_2 is assumed to be imbedded in a freestream of Mach
number M_1. A thin airfoil is placed at a distance Z' below the lower
jet surface, as shown in Figure 1. This may represent an idealized
configuration of upper-surface blown jet flap. A similar configura-
tion has been analyzed in Ref.[11a] for incompressible flow. The
case where the airfoil is in the mid-stream with different velocity
regions above and below in incompressible flow has been treated by
Ting and Liu [30]. Since the thin airfoil in the stream may be re-
presented by a vortex distribution, the expression for the induced
velocity vector due to a two-dimensional vortex in the linearized

(if $Z'=0$.
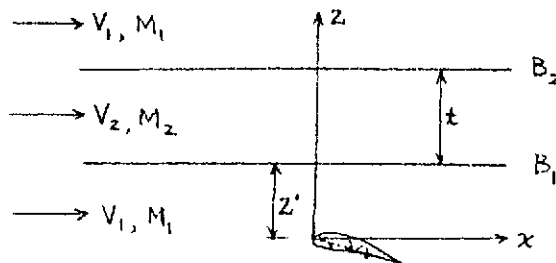
Figure 1. Geometry Definition

compressible flow must be derived. Noting that the vortex axis is in the y-direction, $\vec{\ell} = (Y_2 - Y_1)\hat{j}$ in Eq.(4.28). From Eqs.(4.29) of Section 4, the following relations may be found:

$$\vec{a} \times \vec{\ell} = -(z'-z)(Y_2-Y_1)\hat{i} + (x'-x)(Y_2-Y_1)\hat{k}$$

$$\vec{a'} \times \vec{\ell'} = -\beta^2(z'-z)(Y_2-Y_1)\hat{i} + \beta(x'-x)(Y_2-Y_1)\hat{k}$$

$$\vec{a'} \cdot \vec{\ell'} = \beta^2(Y_1-Y)(Y_2-Y_1)$$

$$\vec{b'} \cdot \vec{\ell'} = \beta^2(Y_2-Y)(Y_2-Y_1)$$

$$|\vec{a'}| = \left[(x-x')^2 + \beta^2(Y_1-y)^2 + \beta^2(z-z')^2\right]^{1/2}$$

$$|\vec{b'}| = \left[(x-x')^2 + \beta^2(Y_2-y)^2 + \beta^2(z-z')^2\right]^{1/2}$$

It follows that if $\gamma\,dx_s = \Gamma$, Eq.(4.28) gives, for a two-dimensional vortex,

$$\vec{q} = \frac{\Gamma\beta^2}{4\pi} \frac{\hat{i}(z-z')(Y_2-Y_1) - \hat{k}(x-x')(Y_2-Y_1)}{\beta^2(Y_2-Y_1)^2\left[(x-x')^2+\beta^2(z-z')^2\right]} \lim_{\substack{Y_1\to-\infty \\ Y_2\to+\infty}} \left\{ \frac{\beta^2(Y_2-y)(Y_2-Y_1)}{\left[(x-x')^2+\beta^2(Y_2-y)^2+\beta^2(z-z')^2\right]^{\frac{1}{2}}} \right.$$

$$\left. - \frac{\beta^2(Y_1-y)(Y_2-Y_1)}{\left[(x-x')^2+\beta^2(Y_1-y)^2+\beta^2(z-z')^2\right]^{\frac{1}{2}}} \right\}$$

$$= \frac{\Gamma\beta^2}{4\pi} \frac{\hat{i}(z-z') - \hat{k}(x-x')}{(x-x')^2+\beta^2(z-z')^2} \cdot \frac{2}{\beta} = \frac{\Gamma\beta}{2\pi} \frac{\hat{i}(z-z') - \hat{k}(x-x')}{(x-x')^2 + \beta^2(z-z')^2} \qquad (1)$$

To examine how disturbances reflect and diffract at the inter-face of two flows of different energy levels, consider a vortex of Γ_1 at $z' = -h$ in region 1. See Fig. 2. The boundary conditions at $z = 0$ are

$$\frac{w_1}{V_1} = \frac{w_2}{V_2} \qquad \text{(Flow tangency)} \qquad (2)$$

$$S_1 V_1 u_1 = S_2 V_2 u_2 \qquad \text{(Pressure continuity)} \qquad (3)$$

Due to the presence of the vortex Γ_1 at $(x', -h)$, the flow

field in region 2 will be disturbed. According to Koning's concept

[12] for incompressible flow, the disturbed flow field in region 2

due to the vortex can be represented by an additional vortex which

must be situated outside the region. In the present case, a vortex

of strength b at $z' = -\beta_1 h/\beta_2$ will be introduced. It follows that the

induced flow in region 2 can be written as
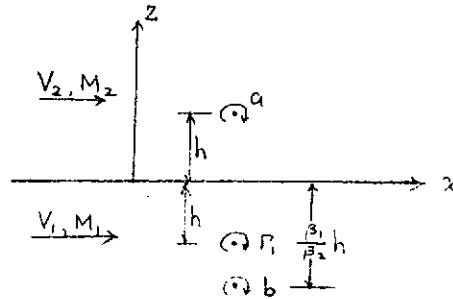
Figure 2. Vortex Images

$$\vec{q}_2 = \frac{b\beta_2}{2\pi} \frac{\hat{\imath}(z + \frac{\beta_1}{\beta_2}h) - \hat{k}(x - x')}{(x - x')^2 + \beta_2^2(z + \beta_1 h/\beta_2)^2} \tag{4}$$

On the other hand, the disturbance due to the vortex Γ_1 will be re-

flected back to region 1 at the interface. This reflected disturbance

can be represented by a vortex of strength "a" at the image point

in region 2. Hence, the total induced flow in region 1 is

$$\vec{q}_1 = \frac{\Gamma_1 \beta_1}{2\pi} \frac{\hat{\imath}(z + h) - \hat{k}(x - x')}{(x - x')^2 + \beta_1^2(z + h)^2} + \frac{a\beta_1}{2\pi} \frac{\hat{\imath}(z - h) - \hat{k}(x - x')}{(x - x')^2 + \beta_1^2(z - h)^2} \tag{5}$$

Using Eqs. (4) and (5), the boundary condition Eq. (2) becomes

$$V_2 \left\{ -\frac{\Gamma_1 \beta_1}{2\pi} - \frac{a\beta_1}{2\pi} \right\} \frac{x - x'}{(x - x')^2 + \beta_1^2 h^2} = V_1 \left\{ -\frac{b\beta_2}{2\pi} \right\} \frac{x - x'}{(x - x')^2 + \beta_1^2 h^2}$$

or,

$$V_2 [\Gamma_1 \beta_1 + a \beta_1] = V_1 b \beta_2 \tag{6}$$

Similarly, the pressure condition becomes

$$S_1 V_1 \left\{ \frac{\Gamma_1 \beta_1}{2\pi} - \frac{a \beta_1}{2\pi} \right\} \frac{h}{(\lambda - x')^2 + \beta_1^2 h^2} = S_2 V_2 \left\{ \frac{b \beta_2}{2\pi} - \frac{\beta_1}{\beta_2} \right\} \frac{h}{(\lambda - x')^2 + \beta_1^2 h^2}$$

or,

$$S_1 V_1 [\Gamma_1 \beta_1 - a \beta_1] = S_2 V_2 b \beta_1 \tag{7}$$

Solving Eqs.(6) and (7) simultaneously for a and b, it is found that

$$a = - \frac{\dfrac{S_2 V_2^2}{S_1 V_1^2} - \dfrac{\beta_2}{\beta_1}}{\dfrac{S_2 V_2^2}{S_1 V_1^2} + \dfrac{\beta_2}{\beta_1}} \Gamma_1 \tag{8}$$

$$b = \frac{2 \dfrac{V_2}{V_1}}{\dfrac{S_2 V_2^2}{S_1 V_1^2} + \dfrac{\beta_2}{\beta_1}} \Gamma_1 \tag{9}$$

Eqs.(8) and (9) show that the parameters determining the additional

vortex strength "a" of the reflected disturbances and the vortex strength

"b" for the diffracted disturbances are the dynamic pressure ratio,

the velocity ratio and the β ratio. It is seen from Eq.(6) that the

ratio of the vortex strengths in the two regions depends not only

on the velocity ratio but also on the β ratio. In incompressible

flow, Eqs.(8) and (9) become

$$a = -\frac{\dfrac{V_2^2}{V_1^2} - 1}{\dfrac{V_2^2}{V_1^2} + 1}\,\Gamma_1 \tag{10}$$

$$b = \frac{2\,\dfrac{V_2}{V_1}}{\dfrac{V_2^2}{V_1^2} + 1}\,\Gamma_1 \tag{11}$$

which can be seen to be the same as those given by Koning [p. 390, Ref. 12].

The above results can be summarized as follows: (1) Reflection is accounted for by putting an additional vortex with strength "a" at a distance equal to that of the originating vortex from the interface and at the opposite side of the interface. (2) Diffraction is accounted for by putting a vortex of strength "b" at a distance equal to that of the originating vortex from the interface multiplied by $\beta_{(\text{incident})} / \beta_{(\text{diffracted})}$ and at the same side as the orginating vortex.

Now apply the above principles to the configuration shown in Fig. 1. Define Z_1 and Z_2 as the distances from the lower and upper jet boundaries, B_1 and B_2, respectively. The distance will be regarded as positive if the vortex is above the boundary. Let the "reflection" and "diffraction" coefficients λ and δ be defined as follows:

$$\lambda_{12} = -\frac{\dfrac{S_2 V_2^2}{S_1 V_1^2} - \dfrac{\beta_2}{\beta_1}}{\dfrac{S_2 V_2^2}{S_1 V_1^2} + \dfrac{\beta_2}{\beta_1}} \tag{12}$$

$$\lambda_{21} = - \frac{\dfrac{S_1 V_1^2}{S_2 V_2^2} - \dfrac{\beta_1}{\beta_2}}{\dfrac{S_1 V_1^2}{S_2 V_2^2} + \dfrac{\beta_1}{\beta_2}} \qquad (13)$$

$$\delta_{12} = \frac{2 \dfrac{V_2}{V_1}}{\dfrac{S_2 V_2^2}{S_1 V_1^2} + \dfrac{\beta_2}{\beta_1}} \qquad (14)$$

$$\delta_{21} = \frac{2 \dfrac{V_1}{V_2}}{\dfrac{S_1 V_1^2}{S_2 V_2^2} + \dfrac{\beta_1}{\beta_2}} \qquad (15)$$

A vortex γ at a distance h from B_1 (or $Z_1 = -h$) is reflected at B_1, with an additional vortex $\lambda_{12}\gamma$ at $Z_1 = +h$ and diffracted into the midstream with a vortex $\delta_{12}\gamma$ at $Z_1 = -\dfrac{\beta_1}{\beta_2}$ h. The diffracted disturbance is then reflected at B_2 to give an additional vortex $\delta_{12}\lambda_{21}\gamma$ at $Z_2 = \dfrac{\beta_1}{\beta_2}$h + t. The reflected disturbances are in turn reflected and diffracted at B_1. The diffracted disturbances into the lower region are due to the vortex $\delta_{12}\lambda_{21}\delta_{21}\gamma$ at $Z_1 = (\beta_1 h/\beta_2 + 2t)\dfrac{\beta_2}{\beta_1} = h + 2t\beta_2/\beta_1$, and so on. These are illustrated in Fig. 3. If $\beta_1 = \beta_2$, the first diffracted image for the lower region would be at $Z_1 = h + 2t$ with strength equal to

$$\delta_{12}\lambda_{21}\delta_{21}\gamma = \left(\frac{V_2^2 - V_1^2}{V_2^2 + V_1^2}\right)\left(\frac{2 V_1 V_2}{V_1^2 + V_2^2}\right)^2 \gamma$$

This last expression agrees with that given in Eq.(10) of Ref. 30. (Eq.(10) of Ref. 30 seems in error in the image locations, as can be easily checked. The originating vortex is in the upper stream

$\delta_{21} \lambda_{21}^{3} \gamma(\cdot) \quad (Z_2 = \frac{\beta_1}{\beta_2} h + 3t)$

$\delta_{12} \lambda_{21}^{3} \delta_{21} \gamma(\cdot) \quad (Z_1 = h + 4t \frac{\beta_2}{\beta_1})$

$\delta_{12} \lambda_{21} \gamma(\cdot) \quad (Z_2 = \frac{\beta_1}{\beta_2} h + t)$

$\delta_{12} \lambda_{21} \delta_{21} \gamma(\cdot) \quad (Z_1 = h + 2t \frac{\beta_2}{\beta_1})$

$V_1 \longrightarrow$

B_2

$V_2 \longrightarrow$

t

$\lambda_{12} \gamma(\cdot) \quad (Z_1 = h)$

B_1

$\gamma(\cdot) \quad (Z_1 = -h)$

$V_1 \longrightarrow$

$\delta_{12} \gamma(\cdot) \quad (Z_1 = -\frac{\beta_1}{\beta_2} h)$
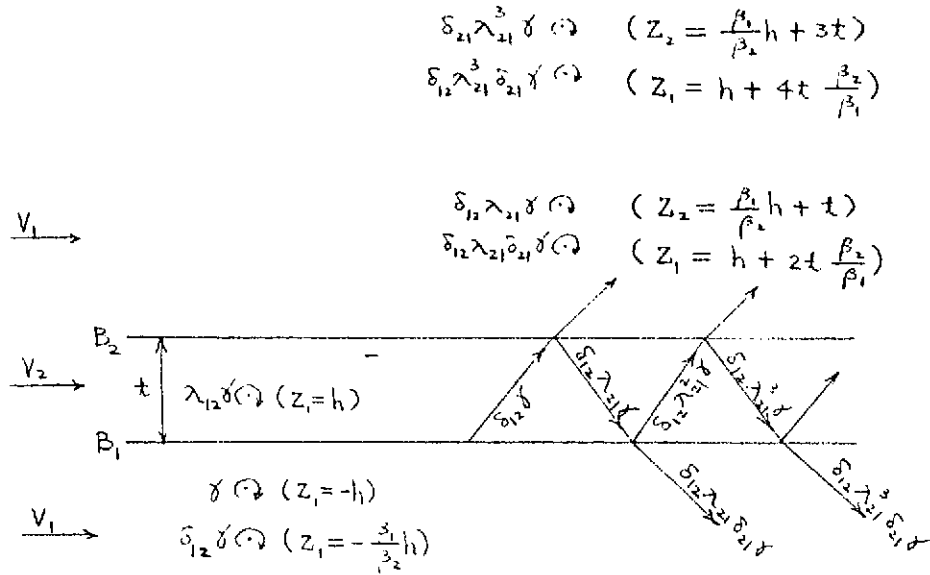
Figure 3. Vortex Image System for Airfoil-Jet Interaction

while the images are also in the upper stream. This violates the principle that no additional flow singularities can be introduced into the region under consideration [12]). Adding the effects of all image vortices in the upper stream gives the total diffracted disturbances in the lower stream. With reference to the airfoil coordinate system, the downwash produced at the airfoil is given by

$$w(x, o) = -\frac{\beta_1}{2\pi} \int_0^1 \left\{ \frac{1}{x-x'} + \frac{\lambda_{12}(x-x')}{(x-x')^2 + \beta_1^2 4h^2} + \right.$$

$$\left. \delta_{12} \delta_{21} \lambda_{21} \sum_{i=1}^{\infty} \frac{\lambda_{21}^{2i-2}(x-x')}{(x-x')^2 + 4\beta_1^2 (h + it \frac{\beta_2}{\beta_1})^2} \right\} \gamma(x')\, dx' \qquad (16)$$

where the downwash is normalized with respect to V_1 and all lengths are based on the chord length. The airfoil integral equation becomes, using Eq.(16),

$$w(x, o) = \frac{dZ_c}{dx} - \alpha \tag{17}$$

Following the classical airfoil theory, Eq.(17) can be solved by assuming

$$\gamma(x') = 2 \left(A_o \cot\frac{\theta}{2} + \sum_{n=1}^{\infty} A_n \sin n\theta \right) \tag{18}$$

$$x' = \frac{1}{2}(1 - \cos\theta) \tag{19}$$

When Eq.(18) is substituted into Eq.(16), some integrals must be evaluated. It is known that

$$\frac{1}{2\pi} \int_0^1 \frac{\gamma(x') dx'}{x - x'} = \frac{1}{\pi} \int_0^\pi \frac{\left(A_o \cot\frac{\theta}{2} + \sum_{n=1}^{\infty} A_n \sin n\theta \right) \sin\theta \, d\theta}{\cos\theta - \cos\phi}$$

$$= A_o - \sum_{n=1}^{\infty} A_n \cos n\phi \tag{20}$$

$$\frac{1}{2\pi} \int_0^1 \frac{\gamma(x')(x-x') \, dx'}{(x-x')^2 + Z^2/4} = \frac{1}{\pi} \int_0^\pi \frac{\left(A_o \cot\frac{\theta}{2} + \sum_{n=1}^{\infty} A_n \sin n\theta \right)\frac{1}{2}(\cos\theta - \cos\phi)\frac{1}{2}\sin\theta \, d\theta}{\frac{1}{4}(\cos\theta - \cos\phi)^2 + \frac{1}{4}Z^2}$$

$$= \frac{1}{\pi} \int_0^\pi \frac{\left(A_o \cot\frac{\theta}{2} + \sum_{n=1}^{\infty} A_n \sin n\theta \right)(\cos\theta - \cos\phi) \sin\theta \, d\theta}{(\cos\theta - \cos\phi)^2 + Z^2} \tag{21}$$

From Ref.(30), it is obtained that

$$J_0(Z, \phi) = \frac{1}{\pi} \int_0^\pi \frac{(\cos\theta - \cos\phi)\sin\theta}{(\cos\theta - \cos\phi)^2 + Z^2} \cot\frac{\theta}{2}\, d\theta$$

$$= 2 \frac{(D - D^{-1})\cos\phi' + D^2 - \cos 2\phi'}{D^2 + D^{-2} - 2\cos 2\phi'} \tag{22}$$

$$J_n(Z, \phi) = \frac{1}{\pi} \int_0^\pi \frac{(\cos\theta - \cos\phi)\sin\theta}{(\cos\theta - \cos\phi)^2 + Z^2} \sin n\theta\, d\theta$$

$$= - D^n \overline{\cos n\phi'} \qquad , \qquad n = 1, 2, \cdots \tag{23}$$

where

$$D(Z, \phi) = \frac{2^{1/2}}{\{2 + Z' + [(Z')^2 + 4Z^2]^{1/2}\}^{1/2} + \{Z' + [(Z')^2 + 4Z^2]^{1/2}\}^{1/2}} \tag{24}$$

$$\phi'(Z, \phi) = \cos^{-1}\left\{ \cos\phi \left[\frac{2}{2 + Z' + (Z'^2 + 4Z^2)^{1/2}}\right]^{1/2} \right\} \tag{25}$$

$$Z'(Z, \phi) = Z^2 - \sin^2\phi \tag{26}$$

With Z_i, J_{oi} and J_{ni} defined as

$$Z_i = 4\beta_1 \left(h + i t \frac{\beta_2}{\beta_1}\right) \tag{27}$$

$$J_{oi} = J_o(Z_i, \phi) \tag{28}$$

$$J_{ni} = J_n(Z_i, \phi) \tag{29}$$

the airfoil integral equation can be reduced to

$$A_o - \sum_{n=1}^\infty A_n \cos n\phi + \lambda_{12}\left[A_o J_{oo} + \sum_{n=1}^\infty A_n J_{no}\right] +$$

$$\delta_{12}\delta_{21}\lambda_{21}\sum_{i=1}^\infty \lambda_{21}^{2i-2}\left[A_o J_{oi} + \sum_{n=1}^\infty A_n J_{ni}\right] = -\frac{1}{\beta_1}\left(\frac{dZ_c}{dx} - \alpha\right) \tag{30}$$

Eq.(30) can be solved by expanding all J_{ni}'s and dz_c/dx in cosine

Fourier series and equating the coefficients of cosine terms on both

sides. For this purpose, the program listed in Ref.(31) was revised

to solve Eq.(30).

2. Numerical Results and Discussions

To check the correctness of the computer program, Shollenberger's

results [11a] for incompressible flow were compared. According to

Figure 10 of Ref.[11a], for an actuator disk thrust coefficient $C_T = 0.5$

with the airfoil just at the lower jet boundary, c_ℓ is found to be

1.44 at $\alpha = 10°$. This is the lift coefficient for the flat-plate

airfoil and simulated nacelle combination with the airfoil one chord

length behind the nacelle. In the present program, no nacelle was

included and the jet was extended to infinite upstream. Furthermore,

no jet boundary displacement was assumed. To use the program, the

velocity ratio was needed. This was computed by the momentum theory

as follows:

$$C_T = \frac{S A_p (V_1 + v_1/2) v_1}{A_p \frac{1}{2} S V_1^2} = 2 \frac{v_1}{V_1} + \left(\frac{v_1}{V_1} \right)^2 \tag{31}$$

or,

$$\frac{1}{2} = 2 \frac{v_1}{V_1} + \left(\frac{v_1}{V_1} \right)^2$$

Hence,

$$\frac{v_1}{V_1} = 0.225$$

$$\frac{V_2}{V_1} = \frac{V_j}{V_1} = 1 + \frac{v_1}{V_1} = 1.225$$

The program gave $c_\ell / 2\pi\alpha = 1.2016$ at V_j/V_1 (or V_2/V_1) = 1.225. There-
fore, c_ℓ may be computed to be 1.3177. This result is seen to have
the same order of magnitude as that given in Ref.[11a].

The results for some incompressible cases for $t/c = 0.5$ are
presented in Fig.4. The variation of the lift and moment coefficients
with the velocity ratio and the vertical distance is typical. As
the airfoil is moved away from the jet, both c_ℓ and $-c_{m\ell}$ are de-
creased. On the other hand, if the velocity ratio is increased, both
c_ℓ and $-c_{m\ell}$ are also increased. The dashed lines represent the
case where all diffracted disturbances are ignored, so that only the
first two terms in Eq.(16) are included in the analysis. The results
show that the reflection represents the primary contribution in the
jet interaction for this jet thickness ratio. Notice also the center
of pressure shift due to the interaction. The interaction tends to
shift the c.p. backward until the airfoil is moved close to the jet
surface. By comparing the two curves in Figure 4c, it may be concluded
that diffracted disturbances tend to move the c.p. forwards and re-
flected disturbances would move the c.p. in the opposite direction.
Since the diffraction terms are more important as the airfoil gets
closer to the jet boundary, this explains why the c.p. will shift
rapidly forwards as the airfoil is moved toward the jet boundary.
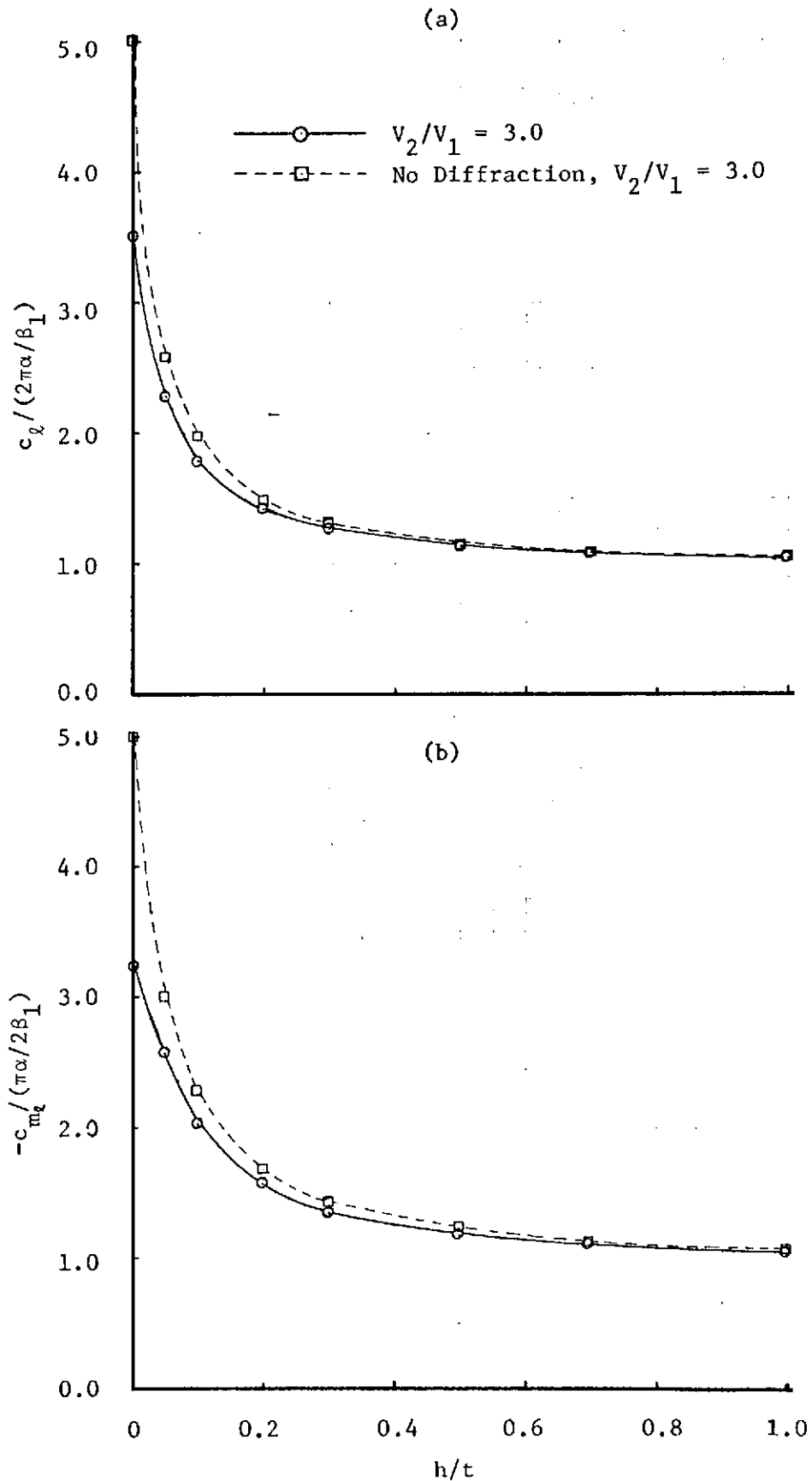
Figure 4 Variation of Aerodynamic Characteristics of a Flat-
Plate Airfoil with Jet Interaction in Incompressible
Flow. t/c=0.5

P.12
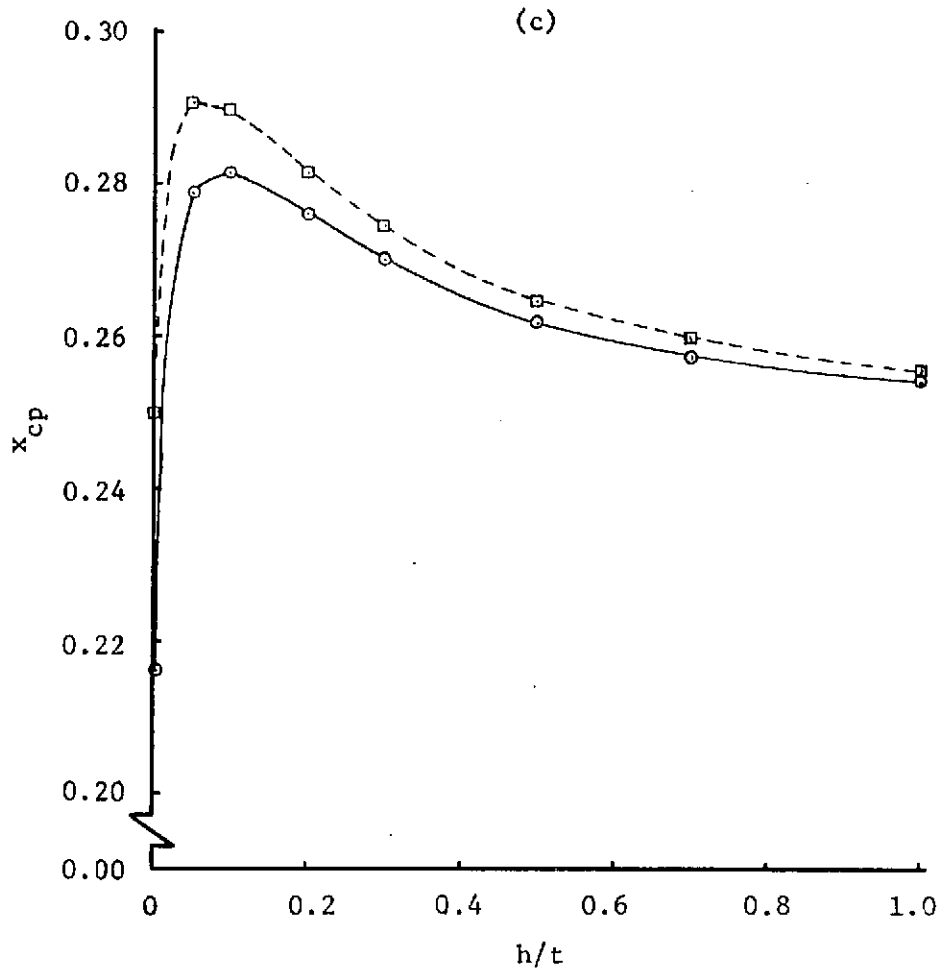
Figure 4 Concluded

The values of the "reflection" and "diffraction" coefficients as defined in Eqs.(12)-(15) are given in Table 1. Notice that the increase in c_ℓ and $-c_{m_\ell}$ is associated with more negative "reflection" coefficient λ_{12}.

In the compressible flow, $T_2/T_1 = 3.0$ and $M_1 = 0.4$ were assumed. The Mach number ratio and the density ratio are computed by the following relations:

$$\left(\frac{M_2}{M_1}\right)^2 = \left(\frac{V_2}{V_1}\right)^2 \left(\frac{T_1}{T_2}\right) \tag{32}$$

$$\frac{\rho_2}{\rho_1} = \frac{T_1}{T_2} \tag{33}$$

Table 1

Reflection and Diffraction Coefficients

V_2/V_1	Case 1 $M_1 = 0$, $T_2/T_1 = 1.0$	Case 2 $M_1 = 0.4$, $T_2/T_1 = 3.0$	
	3.0	1.5	3.0
λ_{12}	-0.8	0.1542	-0.5845
λ_{21}	0.8	-0.1542	0.5845
δ_{12}	0.6	1.6915	1.5845
δ_{21}	0.6	0.5771	0.4155

Eq.(33) implies that $p_1 = p_2$. The results are shown in Figure 5.
The diffraction is seen to be important for $V_2/V_1 = 3.0$ but unimportant for $V_2/V_1 = 1.5$. Figure 6 shows how the nonuniformity in Mach numbers will affect the aerodynamic characteristics. It is seen that the loading is slightly increased for the higher jet Mach number with other parameters remaining unchanged. This fact can be explained by the more negative reflection coefficient. For $T_2/T_1 = 1.0$, $V_2/V_1 = 1.5$ and $M_1 = M_2 = 0.4$, λ_{12} can be computed to be -0.3846. On the other hand, if $M_2 = M_1(V_2/V_1) = 0.6$, then $\lambda_{12} = -0.4410$. More negative reflection coefficient implies more lift. Since λ_{12} remains to be -0.3846 even if $M_1 = M_2 = 0$, the above results indicate that the lift augmentation, expressed as $c_\ell \beta_1 / 2\pi\alpha$, in compressible flow is higher than that in incompressible flow.

Cross examination of Figures 4-6 reveals the following results. Comparing Figures 5 and 6 for $V_2/V_1 = 1.5$, it may be concluded that high jet temperature has detrimental effects on loading and produces less nose-down pitching moment about the leading edge. At $T_2/T_1 = 3.0$ and $V_2/V_1 = 1.5$, c_ℓ is less than the uniform flow value because λ_{12} is now positive. Examining Figures 4 and 5 for $V_2/V_1 = 3.0$, it is also seen that the lift augmentation for $T_2/T_1 = 3.0$ and $M_1 = 0.4$ is much less than that in the incompressible flow when the airfoil is close to the jet boundary. Therefore, wind-tunnel tests of wing-jet interaction with cold jet may overestimate the loading unless the dynamic pressures are correctly simulated.
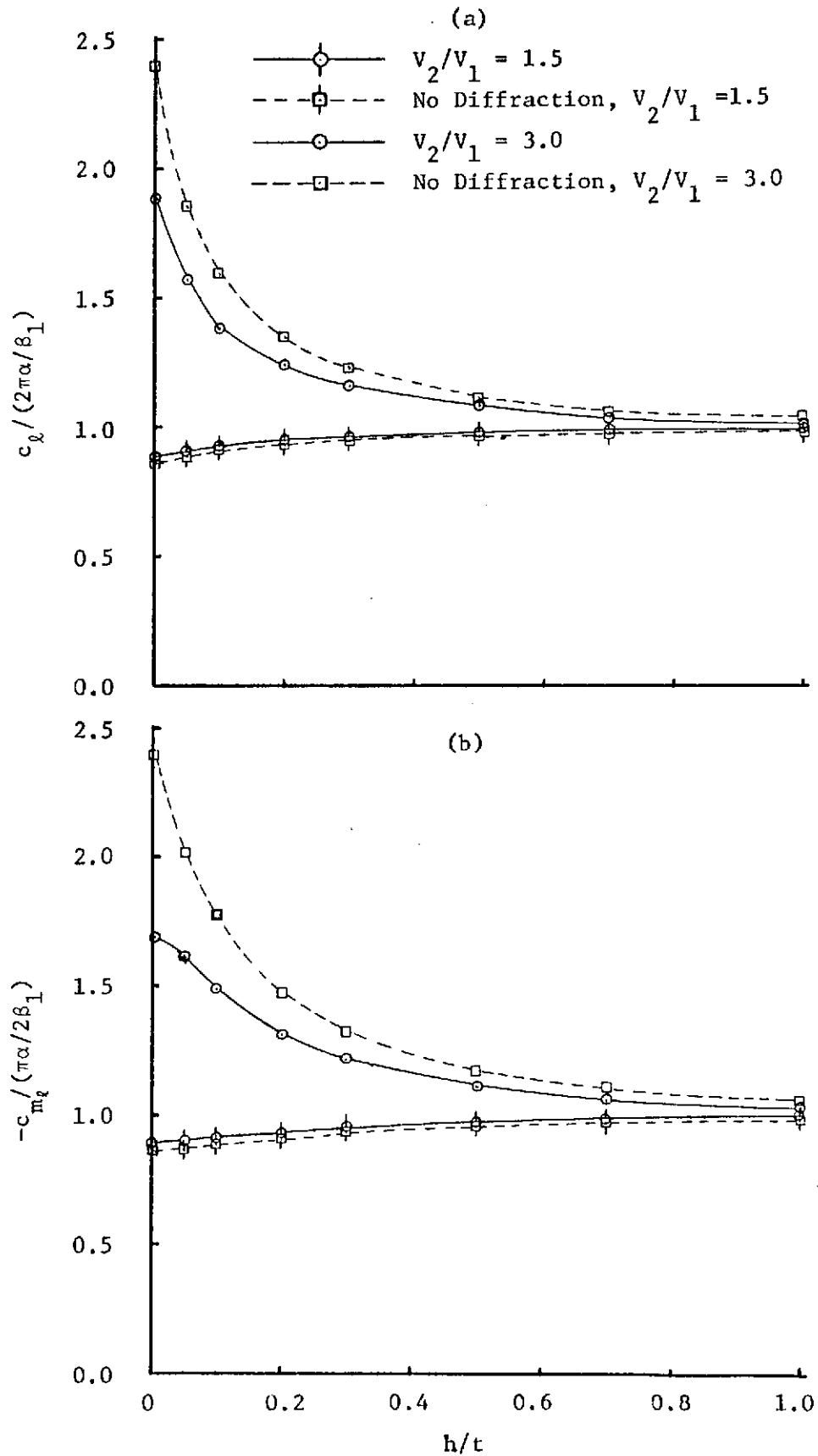
Figure 5 Variation of Aerodynamic Characteristics of a Flat-
Plate Airfoil with Jet Interaction in Linearized
Compressible Flow. $t/c=0.5$, $M_1=0.4$, and $T_2/T_1=3.0$

B.16
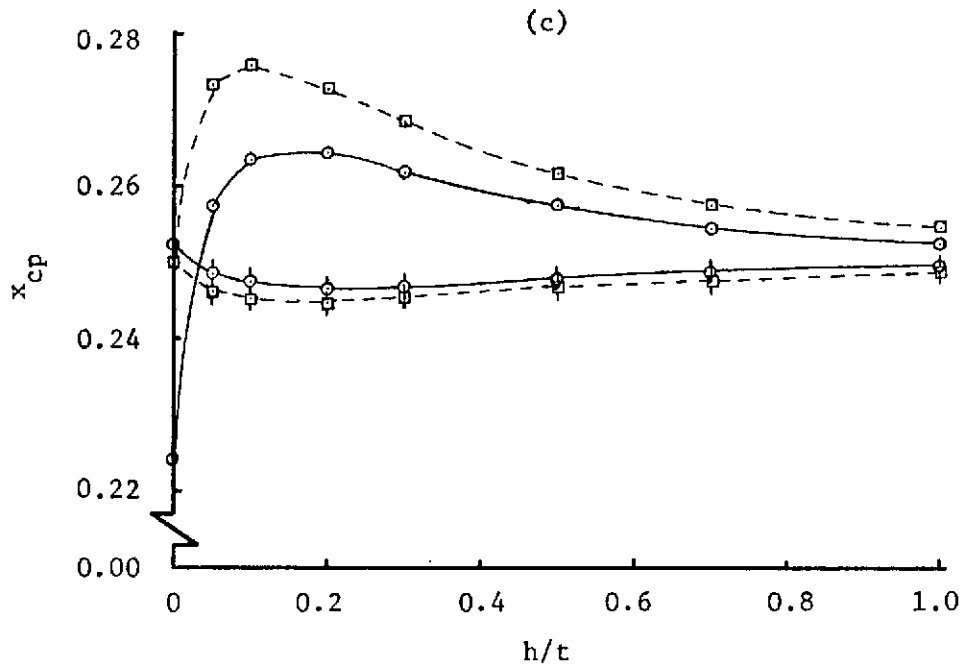
Figure 5   Concluded
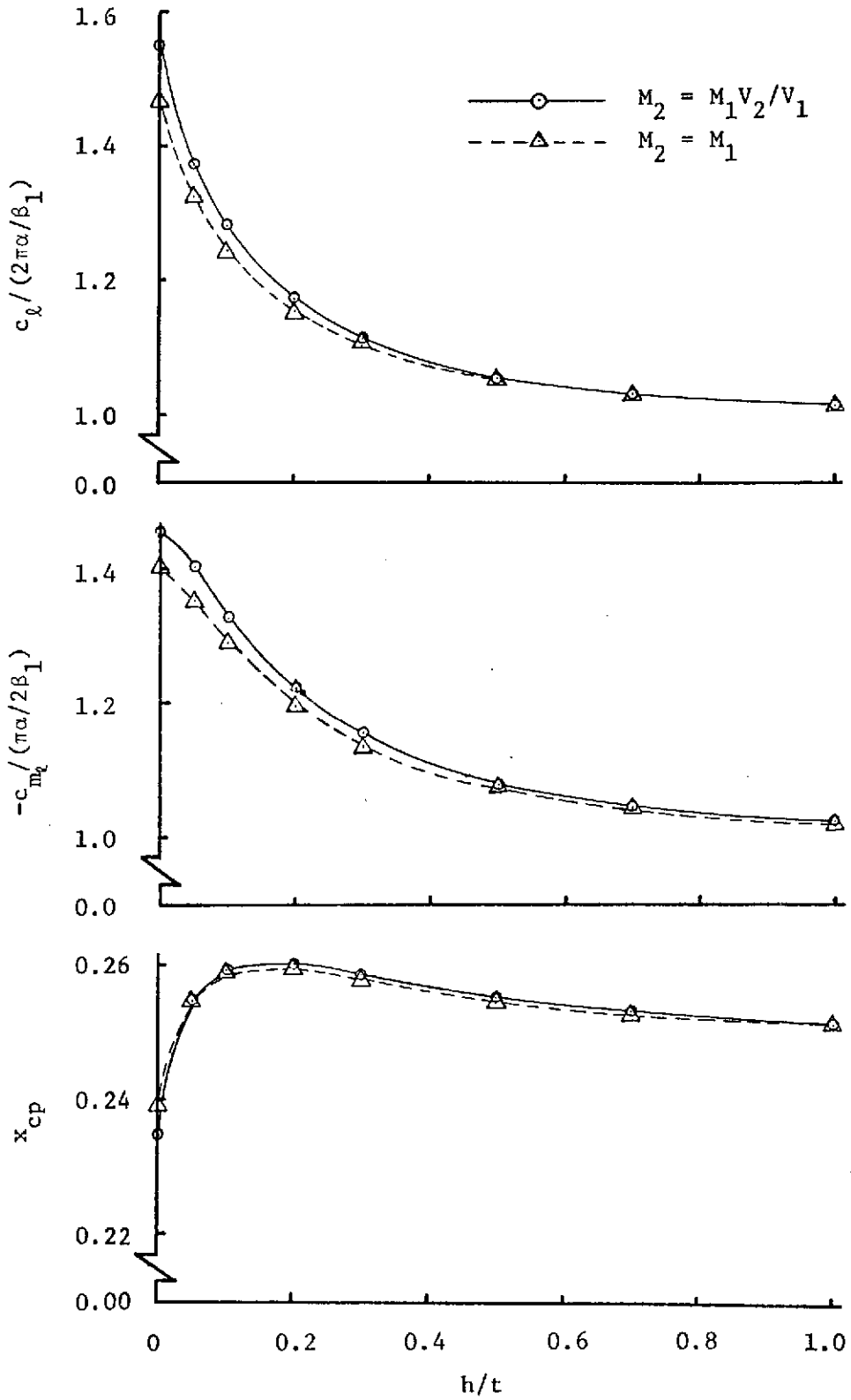
Figure 6 Effect of Mach Number Nonuniformity on Aerodynamic Characteristics of a Flat-Plate Airfoil. $t/c=0.5$, $M_1=0.4$ and $T_2/T_1=1.0$. $V_2/V_1=1.5$

For simplified quantitative estimation of the wing-jet interaction, it has been mentioned above that the reflection accounts for most of the contribution under the specified conditions. In fact, a critical thickness ratio may be defined as that where omission of the diffraction terms would incur less than 1% error. This critical thickness ratio depends on V_2/V_1, T_2/T_1 and M_1. Two typical curves are plotted in Figure 7 for airfoils situated at the lower jet boundary. It is seen that for a hot jet in a compressible external flow, the interaction effect may be estimated quantitatively by accounting only for the reflected disturbances without incurring too much error. Of course, in general, the reflection coefficient is still qualitatively a good measure of how the loading will change with the change in some of the physical parameters.

One interesting result applicable to the upper-surface blowing concept may be mentioned. This is based on the following observations. (1) With negative λ_{12}, i.e., the lift is increased over the uniform flow value, diffraction terms in Eq.(16) are to decrease the loading. These diffraction terms become unimportant as the jet thickness is increased. (2) The loading is always increased when V_2/V_1 is increased. Keeping these two facts in mind, now consider the case with a given amount of thrust. As the jet thickness is increased, the diffraction becomes less important so that the lift is increased, while the decrease in velocity ratio is to decrease the lift. On the other hand, as the jet thickness is decreased, the above two effects reverse the

P. 19
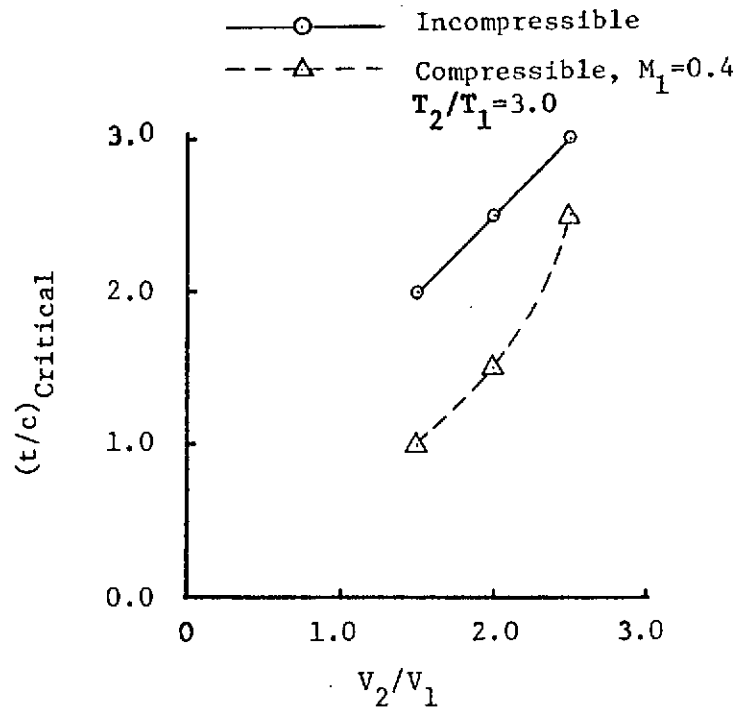
Figure 7 Variation of Critical Jet Thickness with
V_2/V_1

trend. However, for $h = 0$ and $t = 0$, the diffraction terms are so important that they exactly cancel the reflection effect so that the uniform-flow results are obtained. This can be seen by summing the coefficients inside the curly brackets in Eq.(16). This gives

$$f = 1 + \lambda_{12} + \delta_{12}\,\delta_{21}\,\lambda_{21}\,(\,1 + \lambda_{21}^2 + \lambda_{21}^4 + \cdots)$$

$$= 1 + \lambda_{12} + \delta_{12}\,\delta_{21}\,\lambda_{21}\,\frac{1}{1 - \lambda_{21}^2}\quad.$$

But for incompressible case,

$$\lambda_{12} = -\;\frac{\dfrac{V_2^2}{V_1^2} - 1}{\dfrac{V_2^2}{V_1^2} + 1}$$

$$\lambda_{21} = -\,\lambda_{12}$$

$$\delta_{12} = \delta_{21} = \frac{2\,\dfrac{V_2}{V_1}}{\dfrac{V_2^2}{V_1^2} + 1}$$

$$1 - \lambda_{21}^2 = \frac{4\,\left(\dfrac{V_2}{V_1}\right)^2}{\left(\dfrac{V_2^2}{V_1^2} + 1\right)^2}$$

$$\frac{\delta_{12}\,\delta_{21}}{1 - \lambda_{21}^2} = 1$$

It follows that

$$f = 1 + \lambda_{12} + \lambda_{21} = 1\;,$$

independent of the velocity ratio. This result is also true in the compressible flow. Therefore, as the jet thickness is increased from

zero, the lift will be increased. Eventually, the lift will be de-
creased after reaching a maximum value because of the low velocity
ratio associated with the large jet thickness. An optimum jet thick-
ness is seen to exist. For the purpose of numerically computing the
optimum jet thickness, a thrust coefficient C_T of 2.095 per unit
span is assumed, a value taken directly from Ref.[7]. This thrust
coefficient is defined as the amount of thrust divided by the jet
thickness and the freestream dynamic pressure. By the momentum theory,
the velocity ratio then depends on the jet thickness in accordance with
the relation:

$$\frac{V_2}{V_1} = \frac{1}{2}\left[1 + \sqrt{1 + \frac{2\,C_T}{(S_2/S_1)(t/c)}} \right] \tag{34}$$

The results of computation are presented in Figure 8. It is seen
that an optimum jet thickness does exist. For $T_2/T_1 = 1.0$, the op-
timum thickness ratio t/c lies between 0.175 and 0.2, approximately
independent of the Mach number. On the other hand, for $T_2/T_1 = 3.0$,
the optimum t/c becomes 0.1. Some assumptions made in deriving this
result are as follows. (1) The jet has been extended upstream to
infinity, even though in reality the jet may be issued from the air-
foil surface. This fact may affect the results quantitatively. How-
ever, the qualitative conclusion is expected to remain unchanged.
(2) The jet static pressure is assumed to match the ambient static
pressure. (3) No turbulent mixing effect is included. (4) No air-
foil thickness effect has been accounted for in the present linear
theory.
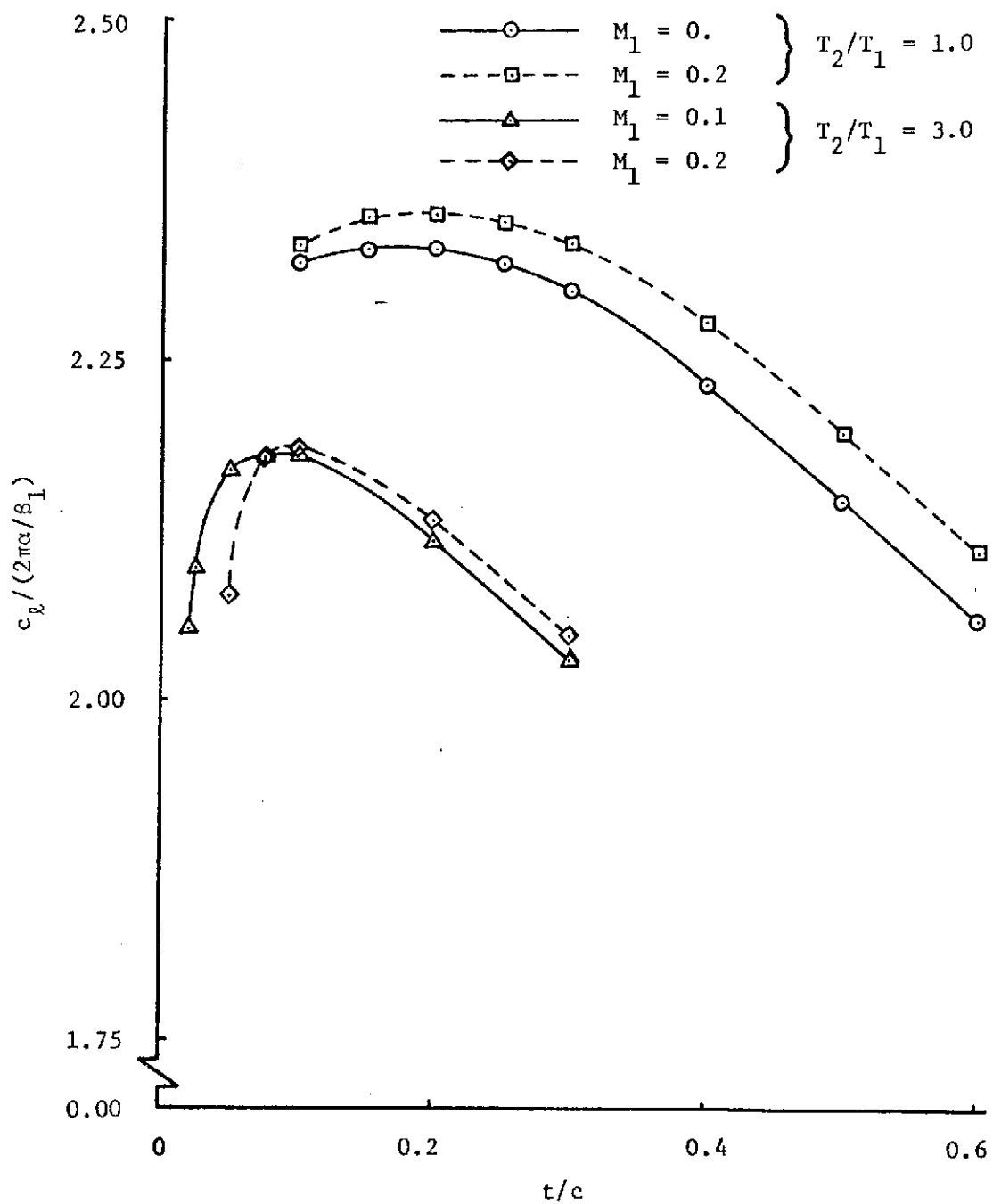
Figure 8 Variation of Optimum Jet Thickness with M_1 and T_2/T_1 for the Upper Surface Blowing Configuration $C_T = 2.095$

Even though the present numerical results and discussions are related to one specific configuration only, the following qualitative generalization is valid. Positive reflection coefficient implies decrease in lift from the uniform flow value. The contrary is true for a negative reflection coefficient. Reflection of airfoil disturbances generated in the high dynamic pressure region from the jet surface into the same region is to decrease the airfoil lift from the uniform flow value. This case is signified by a positive reflection coefficient. For example, if the airfoil in Figure 1 is placed in the jet, the uniform flow conditions are then the jet conditions. The reflection from the jet interface will decrease this uniform-flow loading. On the other hand, reflection of disturbances generated in the low dynamic pressure region from the jet surface into the same region is to increase the loading from the uniform flow value. This last statement applies to the configuration of Figure 1. In general, the diffraction effect is to oppose the reflection one. However, in most applications, the diffraction effect is small. The above generalization is very useful in making interpretation of three-dimensional results in wing-propeller slipstream or wing-jet interaction.

3. Conclusions and Recommendations

The classical formulation of airfoil-jet interaction in inviscid incompressible flow has been extended to the linearized inviscid compressible flow with Mach number nonuniformity. The numerical analysis of this new formulation showed the following results.

(1) The reflection coefficient λ_{12} given in Eq.(12) is the primary parameter which determines the aerodynamic characteristics in the airfoil-jet interaction in either compressible or incompressible flow. A negative value of λ_{12} increases c_ℓ and $-c_{m\ell}$. An equivalent solid body may be used to represent the jet effect only if the flow parameters are such that $\lambda_{12} = -1$. It may be possible to use λ_{12} to correlate the experimental data of wing-jet interaction.

(2) For the upper-surface blowing configuration assumed in the present study, the Mach number nonuniformity with higher jet Mach number increased the lift slightly because the reflection coefficient becomes slightly more negative compared with the uniform Mach number, or the incompressible case.

(3) High jet temperature has detrimental effect on lift as it reduces the jet dynamic pressure, so that λ_{12} increases positively.

(4) For the upper-surface blowing configuration, an optimum jet thickness exists for maximum lift augmentation at a given thrust.

In order to determine the effects of airfoil geometry, turbulent mixing, non-matching of static pressures, etc., on the results obtained in the present study, it is recommended that the finite-difference

method be used to solve the interaction problem. Because of the generality of the finite-difference method, it is expected that the solution technique of such general configurations is also applicable to determining the Coanda jet performance. The two-dimensional general solution, when coupled with a nonlinear lifting line theory, is capable of providing the three-dimensional aerodynamic characteristics for moderate to high aspect-ratio wings.

APPENDIX C

A QUASI VORTEX-LATTICE METHOD IN THIN WING THEORY

1. Introduction

In the conventional vortex lattice method (VLM), the continuous vortex distribution representing the wing in a uniform flow is replaced by a discrete vortex distribution, where a vortex is placed at each elemental quarter chord. Reasonable results have been reported in the past [32 and 33]. However, difficulties exist in the conventional VLM: (1) The convergence of solutions ($C_{L\alpha}$, $C_{m\alpha}$ and C_{Dii}/C_L^2) is slow with respect to the number of elements used, in particular for low aspect-ratio swept wings [32]. (2) The method used to compute the induced drag implies that the leading edge thrust is distributed over the chord, as has been criticized by Hancock [34]. (3) The predicted pressure distribution is reasonably accurate only away from the leading edge. Near the leading edge, the predicted pressure level is always too low, even in the two-dimensional case [35]. It follows that if the leading edge thrust is computed by using the leading-edge pressure distribution, the predicted induced drag would be too high. The purpose of the present investigation is to find ways through theoretical consideration to revise the conventional VLM so that the above-mentioned difficulties can be overcome, yet retaining the simplicity of the VLM.

2. Two-dimensional Theory

In the thin airfoil theory, the downwash on the airfoil is related to the vortex distribution through the following equation:

$$w(x) = \frac{1}{2\pi} \int_0^1 \frac{\gamma(x')dx'}{x-x'} \qquad (1)$$

where the coordinates are referred to the chord length, and w and γ are nondimensionalized with respect to the free stream velocity V_ω. According to the conventional VLM, Eq. (1) is discretized to be [35]

$$2\pi \{w\} = [A] \{\gamma\} \qquad (2)$$

where the elements a_{ij} of the matrix $[A]$ is given by

$$a_{ij} = \frac{\Delta x}{x_i - x_j'} = \frac{1}{1/2 + i - j} \qquad (3)$$

$$x_i = (i-1)\Delta x + 3\Delta x/4$$

$$x_j' = (j-1)\Delta x + \Delta x/4$$

Assuming that $w(x) = 1$, the exact solution of Eq. (1) is then given by

$$\gamma(x) = 2\sqrt{\frac{1-x}{x}} \qquad (4)$$

The exact lift and moment coefficients are

$$c_\ell = \frac{1}{\frac{1}{2}\varsigma V_\omega^2} \cdot \varsigma V_\omega^2 \int_0^1 \gamma(x)dx = 2\int_0^1 2\sqrt{\frac{1-x}{x}}\,dx = 2\pi$$

$$c_{m_{\ell.e.}} = -\frac{c_\ell}{4} = -\frac{\pi}{2}$$

Let $C_s = \lim\limits_{x \to 0} u(x)\sqrt{x}$. Then the suction force can be computed by

$$S = \pi s c_s^2 \tag{5}$$

For a flat plate $C_s = 1$.

To check the accuracy of the VLM, take $i = j = 1$ in Eq. (3). It follows that $a_{ij} = 2$ and hence, $\gamma(x) = \pi$ from Eq. (2) at $x = 1/4$. But from the exact solution, Eq. (4), $\gamma(\frac{1}{4}) = 2\sqrt{3}$, so that the VLM solution is too low. On the other hand, C_ℓ is exact, because

$$c_\ell = \frac{1}{\frac{1}{2} s V_\infty^2} (s V_\infty^2 \pi) = 2\pi$$

It has been shown by James [35] that C_ℓ and $C_{m\ell.e.}$ obtained by VLM are always exact for any number of elements greater than 2. At least two elements are needed to compute $C_{m\ell.e.}$. To examine the accuracy of the predicted $\gamma(x)$ for different number of elements, a few computer runs were made for 2 through 10 elements. Some comparisons are given in Tables 1a and 1b, where N is the number of elements.

Table 1a   Comparison of Vortex Distribution

for N = 3

x	γ by VLM	Exact γ
0.083333	5.890486	6.633250
0.416666	2.356194	2.366432
0.750000	1.178097	1.154701

Table 1b   Comparison of Vortex Distribution

for N = 10

χ	γ by VLM	Exact γ
0.025	11.070787	12.489996
0.125	5.244057	5.291503
0.225	3.701687	3.711843
0.325	— 2.879090	2.882307
0.425	2.325419	2.326320
0.525	1.902616	1.902380
0.625	1.550279	1.549193
0.725	1.233896	1.231764
0.825	0.925422	0.921132
0.925	0.582672	0.569495

From Tables 1a and 1b, it is seen that the primary error in the pre-
dicted $\gamma(\chi)$ occurs near the leading edge and the secondary error
near the trailing edge.

Examination of Eqs. (1) and (2) reveals that the Cauchy singu-
larity and the square-root singularities at the leading and trailing
edges contained in $\gamma(\chi)$ have been completely ignored in the VLM.
The conventional VLM was formulated from the standpoint of computing
the overall aerodynamic characteristics, instead of the local pro-
perties. Therefore, if the VLM is to be improved, the above-mentioned
singularities must be properly accounted for. This is being done in the
following.

Transforming the χ -coordinate to the θ -coordinate through the

following relation

$$\chi = \frac{1}{2}\left(1 - \cos\theta\right),$$ (6)

Eq. (1) can be written as

$$w(\theta) = -\frac{1}{2\pi}\int_0^\pi \frac{\gamma(\theta')\sin\theta'\,d\theta'}{\cos\theta - \cos\theta'}$$ (7)

Let

$$g(\theta) = \gamma(\theta)\sin\theta$$ (8)

Then, to eliminate the Cauchy singularity in the integrand, Eq. (7) is rewritten as

$$w(\theta) = -\frac{1}{2\pi}\int_0^\pi \frac{g(\theta') - g(\theta)}{\cos\theta - \cos\theta'}\,d\theta' - \frac{g(\theta)}{2\pi}\int_0^\pi \frac{d\theta'}{\cos\theta - \cos\theta'}$$

$$= -\frac{1}{2\pi}\int_0^\pi \frac{g(\theta') - g(\theta)}{\cos\theta - \cos\theta'}\,d\theta'$$ (9)

Now, $g(\theta)$ does not contain singularities, because the square-root singularity in $\gamma(\theta)$ has been eliminated by the factor $\sin\theta$. Since the integrand in Eq. (9) is finite everywhere, the integral can be reduced to a finite sum through the modified trapezoidal rule (mid-point rule) [22]. It follows that

$$\int_{0}^{\pi} \frac{g(\theta') - g(\theta)}{\cos\theta - \cos\theta'} d\theta' \cong \Delta\theta' \sum_{k=1}^{N} \frac{g\left(\frac{2k-1}{2}\Delta\theta'\right) - g(\theta)}{\cos\theta - \cos\left(\frac{2k-1}{2}\Delta\theta'\right)}$$

$$= \frac{\pi}{N} \sum_{k=1}^{N} \left[\frac{g\left(\frac{2k-1}{2N}\pi\right)}{\cos\theta - \cos\left(\frac{2k-1}{2N}\pi\right)} - \frac{g(\theta)}{\cos\theta - \cos\left(\frac{2k-1}{2N}\pi\right)} \right] \quad (10)$$

where the last step is allowable if $\theta \neq \theta'$. Now, the primary con-
cern is to eliminate the last term in Eq. (10). This can be done
by choosing a particular set of control points, i.e. θ – values.

Let $\lambda_1, \lambda_2, \cdots, \lambda_N$ be the zeros of $T_N(\lambda)$, the Chebychev
polynomial of the first kind. Then

$$T_N(\lambda) = K (\lambda - \lambda_1)(\lambda - \lambda_2) \cdots\cdots (\lambda - \lambda_N)$$

and by logarithmic differentiation,

$$\sum_{k=1}^{N} \frac{1}{\lambda - \lambda_k} = \frac{T_N'(\lambda)}{T_N(\lambda)} \qquad\qquad (11)$$

Now, if $\lambda = \cos\theta$, it is known that

$$T_N(\cos\theta) = \cos N\theta \quad.$$

The zeros of T_N are therefore $N\theta_k = \frac{2k-1}{2}\pi$, or

$$\theta_k = \frac{2k-1}{2N}\pi$$

$$\lambda_k = \cos\theta_k = \cos\left(\frac{2k-1}{2N}\pi\right), \quad k = 1, 2, \cdots, N \qquad (12)$$

In order that the sum in Eq. (11) be zero, it is required that

$$T_N'(\lambda) = \frac{d}{d\theta}(\cos N\theta)\frac{d\theta}{d\lambda} = N\frac{\sin N\theta}{\sin\theta} \tag{13}$$

must vanish. This is true if $N\theta_i = i\pi$, or

$$\lambda_i = \cos\theta_i = \cos\frac{i\pi}{N} , \quad i = 1, 2, \cdots , N-1 \tag{14}$$

For $i = N$, $T_N'(\lambda_i) \longrightarrow -N^2\cos N\pi$ and $T_N'(\lambda_i)/T_N(\lambda_i) \longrightarrow -N^2$.
This is the situation when $\theta = \pi$ in Eq. (6), or $x = 1$. But at $\theta = \pi$,
$g(\theta) = \gamma(\theta)\sin\theta = 0$. Hence, the control points in Eq. (14) can be
extended to $i = N$, i.e., the trailing edge. On the other hand, if
$i = 0$, i.e., at the leading edge, it can be shown from Eq. (13) that
$T_N'/T_N \longrightarrow N^2$. Since the unknown function $\gamma(\theta)$ is known to possess
a square-root singularity at $\theta = 0$, it follows that

$$\lim_{\theta \to 0} g(\theta) = \lim_{\theta \to 0} \gamma(\theta)\sin\theta = \lim_{x \to 0} C\sqrt{\frac{1-x}{x}} \cdot 2\sqrt{x(1-x)} = 2C \tag{15}$$

Hence, if the control points are chosen at N + 1 points, i.e., $i = 0$,
1, . . . N, in Eq. (14), (N + 1) unknowns, $\gamma_1, \gamma_2, \cdots, \gamma_N, C$ can be
computed. Note that the parameter C in Eq. (15) is related to the
leading-edge suction parameter C_s, because $u(x) = \gamma(x)/2$. Hence,

$$C_s = \lim_{x \to 0} u(x)\sqrt{x} = \lim_{x \to 0} \frac{\gamma(x)}{2}\sqrt{x} = \frac{1}{2}C \tag{16}$$

If the singularity in γ is weaker than the square root singularity,
then $C = 0$, as in the case of parabolic camber. It follows that the

above-described procedures not only predict γ-values, but also the leading-edge suction directly.

Using the concept just described, Eq. (9) can now be reduced to

$$w(\theta_i) = -\frac{1}{2\pi} \frac{\pi}{N} \sum_{k=1}^{N} \frac{\gamma_k \sin\theta_k}{\cos\theta_i - \cos\theta_k} + \begin{cases} \frac{1}{2\pi} \frac{\pi}{N} (2c) N^2 , & i=0 \\ 0 & , & i \neq 0 \end{cases}$$

$$= \frac{1}{2N} \sum_{k=1}^{N} \frac{\gamma_k \sqrt{x_k(1-x_k)}}{x_i - x_k} + \begin{cases} Nc , & i=0 \\ 0 , & i \neq 0 \end{cases} \qquad (17)$$

where

$$\gamma_k = \gamma(\theta_k)$$

$$x_k = \frac{1}{2}\left[1 - \cos\left(\frac{2k-1}{2N}\pi\right)\right] , \quad k = 1, 2, \cdots, N$$

$$x_i = \frac{1}{2}\left[1 - \cos\frac{i\pi}{N}\right] , \quad i = 0, 1, \cdots, N \qquad (18)$$

$$\theta_k = \frac{2k-1}{2N}\pi$$

Eq. (17) can be written in a matrix form for the solution of γ as follows:

$$\{w\} = [A]\{\gamma\} \qquad (19)$$

where

$$a_{ik} = \frac{1}{2N} \frac{\sqrt{x_k(1-x_k)}}{x_i - x_k}$$

$$x_i = \frac{1}{2}\left[1 - \cos\frac{i\pi}{N}\right] , \quad i = 1, \cdots, N$$

$$x_k = \frac{1}{2}\left[1 - \cos\left(\frac{2k-1}{2N}\pi\right)\right] , \quad k = 1, 2, \cdots, N$$

C.8

Once $\{\gamma\}$ is obtained, C can be computed as

$$C = \frac{1}{N} w(\theta_o) + \frac{1}{2N^2} \sum_{k=1}^{N} \gamma_k \sqrt{\frac{1-x_k}{x_k}} \qquad (20)$$

The lift coefficient is given by

$$c_\ell = \frac{L}{\frac{1}{2} S V_\infty^2} = 2 \int_0^1 \gamma(x) \, dx = \int_0^\pi \gamma(\theta) \sin\theta \, d\theta$$

$$= \frac{\pi}{N} \sum_{k=1}^{N} \gamma_k \sin\theta_k \qquad (21)$$

where θ_k is given in Eq. (18). Similarly, the pitching moment co-efficient about the leading edge can be shown to be

$$c_{m_\ell} = \frac{M}{\frac{1}{2} S V_\infty^2} = -2 \int_0^1 \gamma(x) \, x \, dx = \frac{-1}{2} \int_0^\pi \gamma(\theta) (1 - \cos\theta) \sin\theta \, d\theta$$

$$= -\frac{\pi}{2N} \sum_{k=1}^{N} \gamma_k (1 - \cos\theta_k) \sin\theta_k \qquad (22)$$

To show the remarkable accuracy of the above formulation, take $N = 1$. Then $x_i = 1$, $x_k = \frac{1}{2}$ and $a_{ik} = 1/2$. It follows that for $w = 1$, $\gamma(x=\frac{1}{2}) = 2$. This solution is exact, as can be seen from Eq. (4) by putting $x = \frac{1}{2}$. The lift coefficient is

$$c_\ell = \frac{\pi}{1} \times 2 \times 1 = 2\pi$$

and the leading edge suction parameter C is

$$C = \frac{1}{1} + \frac{1}{2} \wedge 2 = 2$$

Both are exact. $C_{m_{\ell}}$ can not be correctly predicted when $N = 1$.

For $N = 2$, the matrix $[A]$ in Eq. (19) can be shown to be

$$[A] = \begin{pmatrix} \frac{1}{4} & -\frac{1}{4} \\ \frac{1}{4(\sqrt{2}+1)} & \frac{1}{4(\sqrt{2}-1)} \end{pmatrix}$$

The solution for $\{\gamma\}$ can be easily obtained to be

$$\gamma_1 = 2(1+\sqrt{2})$$

$$\gamma_2 = 2(\sqrt{2}-1)$$

It follows from Eq. (20) that the suction parameter C is

$$C = \frac{1}{2} + \frac{1}{8}\left[2(1+\sqrt{2})^2 + 2(\sqrt{2}-1)^2\right] = 2$$

The lift and pitching moment coefficients are

$$C_\ell = \frac{\pi}{2}\left[2(1+\sqrt{2})\frac{\sqrt{2}}{2} + 2(\sqrt{2}-1)\frac{\sqrt{2}}{2}\right] = 2\pi$$

$$C_{m_\ell} = -\frac{\pi}{4}\left[2(1+\sqrt{2})\frac{\sqrt{2}}{2}\left(1-\frac{\sqrt{2}}{2}\right) + 2(\sqrt{2}-1)\frac{\sqrt{2}}{2}\left(1+\frac{\sqrt{2}}{2}\right)\right]$$

$$= -\frac{\pi}{2}$$

It can be easily checked that the results for $\{\gamma\}$, C, C_ℓ, and

C_{m_ℓ} are all exact.

For $N > 2$, computer runs were made for N up to 10. Again, all

aerodynamic characteristics of interest are reproduced exactly.

To check whether the present method will work with the same accuracy for cases with camber, consider the case of parabolic camber. For

$$\gamma(x) = 2\sqrt{x(1-x)} \quad ,$$

it can be shown that

$$w(x) = \frac{1}{2\pi} \int_0^1 \frac{2\sqrt{x'(1-x')}}{x-x'} \, dx' = x - \frac{1}{2}$$

C_ℓ and $C_{m_{\ell.e.}}$ are

$$C_\ell = 2\int_0^1 \gamma(x)\,dx = 4\int_0^1 \sqrt{x(1-x)}\,dx = \frac{\pi}{2}$$

$$C_{m_\ell} = -2\int_0^1 \gamma(x)x\,dx = -4\int_0^1 \sqrt{x(1-x)}\,x\,dx = -\frac{\pi}{4} \quad .$$

Of course, the suction parameter C is zero for this case. Computer runs with N = 5 and 10 again reproduced the above results exactly.

3. Three-dimensional Theory.

To apply the above theory to a thin wing of finite aspect ratio , the expressions for the induced velocity due to vortex segments in space are needed. According to p. 43 of Ref.28, the needed expressions are

$$d\vec{q}_1(\vec{R}) = \frac{\beta^2 \gamma(s)ds}{4\pi} \int_L \frac{(\vec{R}_1 - \vec{R}) \times d\vec{\ell}}{R_\beta^3} \tag{23}$$

for a bounded vortex segment of strength $\gamma(s)ds$ of length L , and

$$d\vec{q}_2(\vec{R}) = \frac{\beta^2 \gamma(s)ds}{4\pi} \int_{x_i}^{\infty} \frac{(\vec{R}_1 - \vec{R}) \times d\vec{\ell}}{R_\beta^3} \tag{24}$$

for the corresponding trailing vortices. The notations are (refer-
ring to Fig. 1)

$$\beta^2 = 1 - M_\infty^2$$

$$\gamma(s) = \text{vortex density}$$

$$\vec{R}_1 - \vec{R} = (x'-x)\,\hat{i} + (y'-y)\,\hat{j} + (z'-z)\,\hat{k}$$

$$\dot{R}_\beta^2 = (x-\bar{x}')^2 + \beta^2(y-y')^2 + \beta^2(z-z')^2$$

$$X_i = \text{the } x \text{-coordinate of one end point of the}$$
bounded vortex element
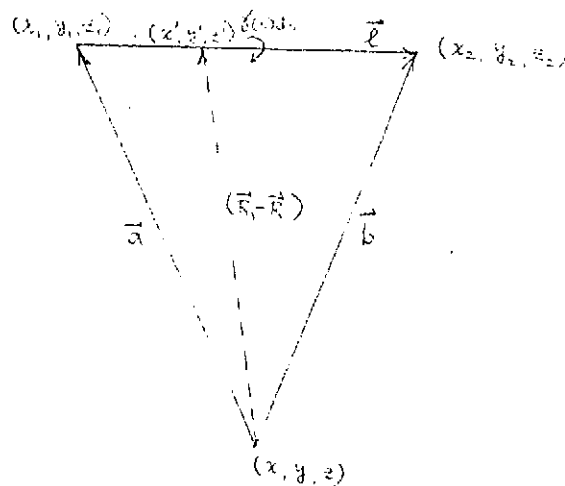
Fig. 1   Vortex Segment Geometry

Eq. (23) can be integrated over the bounded vortex segment L to give
(See Appendix A)

$$d\vec{q}_1(\vec{R}) = \frac{\beta^2}{4\pi}\,\gamma_{(s)}ds\,\frac{\vec{a}\times\vec{\ell}}{|\vec{a}'\times\vec{\ell}'|^2}\left\{\frac{\vec{b}'}{|\vec{b}'|} - \frac{\vec{a}'}{|\vec{a}'|}\right\}\cdot\vec{\ell}' \qquad (25)$$

where

$$\vec{a}' = (x_1-x)\,\hat{\imath} + \beta(y_1-y)\,\hat{\jmath} + \beta(z_1-z)\,\hat{k}$$

$$\vec{b}' = (x_2-x)\,\hat{\imath} + \beta(y_2-y)\,\hat{\jmath} + \beta(z_2-z)\,\hat{k} \qquad (26)$$

For the application in thin wing theory, it can be shown that

$$\vec{a}'\times\vec{\ell}' = \beta\,\hat{k}\left\{(x_1-x)(y_2-y_1) - (x_2-x_1)(y_1-y)\right\}$$

$$\vec{b}'\cdot\vec{\ell}' = (x_2-x_1)(x_2-x) + \beta^2(y_2-y_1)(y_2-y)$$

$$\vec{a}'\cdot\vec{\ell}' = (x_2-x_1)(x_1-x) + \beta^2(y_2-y_1)(y_1-y)$$

It follows that Eq. (25) becomes

$$w_1 = \vec{q}_1\cdot\hat{k} = \frac{1}{4\pi}\int_{x_\ell}^{x_t}\frac{\gamma(x')}{(x_1-x)(y_2-y_1)-(x_2-x_1)(y_1-y)}\left\{\frac{(x_2-x_1)(x_2-x)+\beta^2(y_2-y_1)(y_2-y)}{\sqrt{(x_2-x)^2+\beta^2(y_2-y)^2}}\right.$$

$$\left. - \frac{(x_2-x_1)(x_1-x)+\beta^2(y_2-y_1)(y_1-y)}{\sqrt{(x_1-x)^2+\beta^2(y_1-y)^2}}\right\}\,dx' \qquad (27)$$

Assuming straight trailing vortices on the wing plane, the integral
in Eq. (24) can be reduced to

$$\int_{x_1}^{\infty}\frac{(\vec{R}_1-\vec{R})\times d\vec{\ell}}{R_\beta^3} = \int_{x_1}^{\infty}\frac{\left[(x_s-x)\hat{\imath}+(y_1-y)\hat{\jmath}\right]\times(-\hat{\imath}\,dx_s)}{\left[(x_s-x)^2+\beta^2(y_1-y)^2\right]^{3/2}}$$

$$= \frac{\hat{k}}{\beta^2(y_1-y)}\left[1 - \frac{x_1-x}{\sqrt{(x_1-x)^2+\beta^2(y_1-y)^2}}\right] \qquad (28)$$

Hence, the downwash due to the trailing vortex from the first end

point (x_1 , y_1) of the bounded vortex segment is

$$W_{2(1)} (x, y) = \frac{1}{4\pi} \int_{x_\ell}^{x_t} \frac{\delta(x')}{y_1 - y} \left[1 - \frac{x_1 - x}{\sqrt{(x_1 - x)^2 + \beta^2 (y_1 - y)^2}} \right] dx' \qquad (29)$$

In the same manner, the downwash due to the trailing vortex from the

second end point (x_2, y_2) of the bounded vortex segment is (noting

that $d\vec{\ell} = \hat{\imath} \, dx_3$)

$$W_{2(2)}(x, y) = -\frac{1}{4\pi} \int_{x_\ell}^{x_t} \frac{\delta(x')}{y_2 - y} \left[1 - \frac{x_2 - x}{\sqrt{(x_2 - x)^2 + \beta^2 (y_2 - y)^2}} \right] dx' \qquad (30)$$

Thus, the total downwash produced by a skewed horseshoe vortex element

is the sum of W_1 , $W_{2(1)}$ and $W_{2(2)}$.

For a rectangular horseshoe vortex element, $x_1 = x_2$ and Eq. (27)

shows the usual Cauchy singularity in the x direction. For skewed

elements, with y inside the element under consideration, and if y

(the y-coordinate of a control point) is chosen so that

$$y_1 - y = K'(y_1 - y_2)$$

where K' is some constant less than one, the expression in the denomi-

nator of Eq. (27) can be written

$$(x_1 - x)(y_2 - y_1) - (x_2 - x_1)(y_1 - y) = (y_2 - y_1) \left[(x_1 - x) + K'(x_2 - x_1) \right]$$

$$= (y_2 - y_1) \left[x_1 + K'(x_2 - x_1) - x \right]$$

$$= (y_2 - y_1) \left[x_1 + \frac{x_2 - x_1}{y_2 - y_1}(y - y_1) - x \right] \qquad (31)$$

which vanishes on the vortex segment at the chosen y-coordinate. Thus, the Cauchy singularity exists and the method of integration described in the two-dimensional theory is applicable.

For notational convenience, let

$$u_1(x', x, y) = \frac{(x_2-x_1)(x_2-x) + \beta^2(y_2-y_1)(y_2-y)}{\sqrt{(x_2-x)^2 + \beta^2(y_2-y)^2}} -$$

$$\frac{(x_2-x_1)(x_1-x) + \beta^2(y_2-y_1)(y_1-y)}{\sqrt{(x_1-x)^2 + \beta^2(y_1-y)^2}} \tag{32}$$

$$u_2(x', x, y) = \frac{1}{y_1-y}\left[1 - \frac{x_1-x}{\sqrt{(x_1-x)^2 + \beta^2(y_1-y)^2}}\right] \tag{33}$$

$$u_3(x', x, y) = \frac{1}{y_2-y}\left[1 - \frac{x_2-x}{\sqrt{(x_2-x)^2 + \beta^2(y_2-y)^2}}\right] \tag{34}$$

The total downwash due to a strip of vortex distribution is therefore given by

$$w(x, y) = \frac{1}{4\pi}\int_{x_\ell}^{x_t} \frac{u_1(x', x, y)\,\gamma(x')\,dx'}{(x_1-x)(y_2-y_1) - (x_2-x_1)(y_1-y)} + \frac{1}{4\pi}\int_{x_\ell}^{x_t} u_2(x', x, y)\,\gamma(x')\,dx'$$

$$- \frac{1}{4\pi}\int_{x_\ell}^{x_t} u_3(x', x, y)\,\gamma(x')\,dx' \tag{35}$$

Transforming the integration variable to a non-dimensional one based on the local chord and then to the θ-coordinate, Eq. (35) can be

reduced to a finite sum as follows:

$$w(x,y) = \frac{1}{4\pi} \frac{\pi c}{N} \sum_{k=1}^{N} \frac{u_1(\theta_k)\, \gamma(\theta_k)\, \frac{1}{2}\sin\theta_k}{(x_{1k}-x)(y_2-y_1)-(x_{2k}-x_{1k})(y_1-y)}$$

$$+ \frac{1}{4\pi} \frac{\pi c}{N} \sum_{k=1}^{N} u_2(\theta_k)\, \gamma(\theta_k)\, \frac{1}{2}\sin\theta_k$$

$$- \frac{1}{4\pi} \frac{\pi c}{N} \sum_{k=1}^{N} u_3(\theta_k)\, \gamma(\theta_k)\, \frac{1}{2}\sin\theta_k \qquad (36)$$

where

$$x_{1k} = x_{\ell_1} + c_1\, \xi_k$$

$$x_{2k} = x_{\ell_2} + c_2\, \xi_k$$

$$\xi_k = \frac{1}{2}\left[1 - \cos\left(\frac{2k-1}{2N}\pi\right)\right] \quad , \quad k = 1, 2, \cdots, N \qquad (37)$$

$x_{\ell_1} =$ the leading edge x-coordinat at y_1

$x_{\ell_2} =$ the leading edge x-coordinate at y_2

$c_1 =$ chord length at y_1

$c_2 =$ chord length at y_2

So far, the control-point locations have not been chosen yet. In accordance with the consideration in the two-dimensional theory, the x-coordinates of the control points should be chosen so that

$$x_i = x_\ell + \frac{c}{2}\left[1 - \cos\left(\frac{i\pi}{N}\right)\right], \quad i = 1, \cdots, N \qquad (38)$$

where x_ℓ is the leading edge x-coordinate on the chord c through
the control point. To choose the y control location, it should be
noted that both Eqs. (33) and (34) involve the Cauchy-type singular-
ity in the y-coordinate. Since the downwash expression given in
Eq. (35) is to be summed over the spanwise strips and the summation
is equivalent to integration in some sense, the spanwise summation
can be more accurately performed if the singularity can be removed.
For example, the summation

$$Sum = \sum_j \frac{h(x, y, y_j) - h(x, y, y)}{y_j - y} \qquad (39)$$

can be accurately performed, where $h(x, y, y_j)$ is either of the
expressions in the brackets in Eqs. (33) and (34). Now, if $y \neq y_j$,

$$Sum = \sum_j \frac{h(x, y, y_j)}{y_j - y} - h(x, y, y) \sum_j \frac{1}{y_j - y},$$

and the last term can be eliminated if

$$y_j = -\frac{b}{2} \cos\left(\frac{2j-1}{2M}\pi\right), \quad j = 1, 2, \cdots, M$$

$$y = y_i = -\frac{b}{2} \cos\left(\frac{i\pi}{M}\right), \quad i = 1, 2, \cdots, M-1$$

$$(40)$$

The choice of the control points and the spanwise strips is illustrated in Fig. 2 for M = 5. Admittedly, this choice does not eliminate the effect of Cauchy singularity, because both trailing legs y_1 and y_2 do not occupy the left side of the first strip and the right side of the last strip simultaneously. However, it should reduce the error, as has been proved in the numerical study.
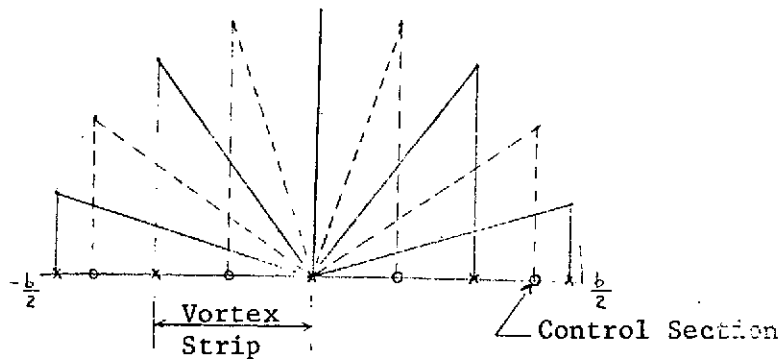
Fig. 2   Illustration of Control Points and Spanwise Strips

To find the leading edge suction parameter, note that the leading edge suction term comes only from the bounded vortex distribution, and hence, from Eq. (27). Transforming Eq. (27) to the θ -coordinate, and noting that Eq. (31) can be written

$$(x_1 - x)(y_2 - y_1) - (x_2 - x_1)(y_1 - y) = (y_2 - y_1)\frac{c}{2}\left[\cos\theta - \cos\theta'\right],$$

since

$$x_1 + K'(x_2 - x_1) = x_1 + \frac{x_2 - x_1}{y_2 - y_1}(y - y_1) = x_\ell + \frac{c}{2}\left(1 - \cos\theta'\right)$$

$$x = x_\ell + \frac{c}{2}\left(1 - \cos\theta\right) ,$$

it is found that

$$W_1(x, y) = \frac{1}{4\pi} \int_0^\pi \frac{u_1(\theta')\, \gamma(\theta')\, \frac{c}{2}\sin\theta'\, d\theta'}{(y_2 - y_1)\frac{c}{2}(\cos\theta - \cos\theta')}$$

$$= \frac{1}{4\pi} \frac{\pi}{N} \sum_{k=1}^{N} \left\{ \frac{u_1(\theta_k)\,\gamma(\theta_k)\sin\theta_k - u_1(\theta)\,\gamma(\theta)\sin\theta}{(y_2 - y_1)(\cos\theta - \cos\theta_k)} \right\} \qquad (4)$$

in accordance with the concept discussed previously in relation to Eqs. (9) and (10).

As shown before,

$$\sum_{k=1}^{N} \frac{1}{\cos\theta - \cos\theta_k} = N^2 \quad \text{if} \quad \theta = 0 ;$$

$$\qquad (42)$$

$$\lim_{\theta \to 0} \gamma(\theta)\sin\theta = 2c$$

Now,

$$\lim_{\theta \to 0} \frac{u_1(\theta)}{(y_2 - y_1)} = \frac{1}{y_2 - y_1}\left\{ \frac{(x_{\ell_2} - x_{\ell_1})(x_{\ell_2} - x_\ell) + \beta^2(y_2 - y_1)(y_2 - y_\ell)}{\sqrt{(x_{\ell_2} - x_\ell)^2 + \beta^2(y_2 - y_\ell)^2}} - \right.$$

$$\left. \frac{(x_{\ell_2} - x_{\ell_1})(x_{\ell_1} - x_\ell) + \beta^2(y_2 - y_1)(y_1 - y_\ell)}{\sqrt{(x_{\ell_1} - x_\ell)^2 + \beta^2(y_1 - y_\ell)^2}} \right\}$$

Since

$$\frac{x_{\ell_2} - x_\ell}{y_2 - y_\ell} = \frac{x_{\ell_2} - x_{\ell_1}}{y_2 - y_1} = \tan \Lambda_\ell ,$$

$$\frac{x_\ell - x_{\ell_1}}{y_\ell - y_1} = \frac{x_{\ell_2} - x_{\ell_1}}{y_2 - y_1} = \tan \Lambda_\ell ,$$

(43)

it follows that

$$\lim_{\theta \to 0} \frac{u_1(\theta)}{(y_2 - y_1)} = \frac{\tan^2 \Lambda_\ell + \beta^2}{\sqrt{\tan^2 \Lambda_\ell + \beta^2}} + \frac{\tan^2 \Lambda_\ell + \beta^2}{\sqrt{\tan^2 \Lambda_\ell + \beta^2}}$$

$$= 2\sqrt{\tan^2 \Lambda_\ell + \beta^2}$$

(44)

Thus, the second term in Eq. (41) becomes

$$\lim_{\theta \to 0} -\frac{1}{4N} \sum_{k=1}^{N} \frac{u_1(\theta)\, \gamma(\theta) \sin\theta}{(y_2 - y_1)(\cos\theta - \cos\theta_k)} = -\frac{1}{4N} \times 2\sqrt{\tan^2 \Lambda_\ell + \beta^2} \times 2 C \times N^2$$

$$= -NC\sqrt{\tan^2 \Lambda_\ell + \beta^2}$$

(45)

If Eq. (45) is used in Eq. (36) which must be summed spanwise, it is found that

$$NC\sqrt{\tan^2 \Lambda_\ell + \beta^2} = \sum \frac{c}{4N} \sum_{k=1}^{N} \frac{u_1(\theta_k)\, \gamma(\theta_k) \frac{1}{2} \sin\theta_k}{(x_{1_k} - x)(y_2 - y_1) - (x_{2_k} - x_{1_k})(y - y_1)}$$

$$+ \sum \frac{c}{4N} \sum_{k=1}^{N} u_2(\theta_k)\, \gamma(\theta_k) \frac{1}{2} \sin\theta_k$$

$$- \sum \frac{c}{4N} \sum_{k=1}^{N} u_3(\theta_k)\, \gamma(\theta_k) \frac{1}{2} \sin\theta_k$$

$$- \left(\frac{dz_c}{dx} - \alpha \right) \qquad , \qquad \text{at } x = x_\ell$$

(46)

C. 20

where the unmarked summation is to be performed in the spanwise direction. Once the parameter C for each strip has been obtained, the magnitude of the sectional leading-edge thrust coefficient c_t can be computed [36]:

$$c_t = \frac{\pi}{8c} \frac{1}{\cos \Lambda_\ell} \sqrt{1 - M_\infty^2 \cos^2 \Lambda_\ell} \left[\lim_{x \to x_\ell} \Delta C_p (x - x_\ell)^{\frac{1}{2}} \right]^2$$

where

$$\lim_{x \to x_\ell} \Delta C_p (x - x_\ell)^{\frac{1}{2}} = \lim_{x \to x_\ell} 2 \gamma(x) (x - x_\ell)^{\frac{1}{2}} = 2 C \sqrt{c}$$

Hence,

$$c_t = \frac{\pi}{2} \frac{1}{\cos \Lambda_\ell} \sqrt{1 - M_\infty^2 \cos^2 \Lambda_\ell} \; C^2 \tag{47}$$

For a skewed bounded element, the total vortex density of the element is $\gamma \Delta y / \cos \psi$, where Δy is the strip width and ψ is the element sweep angle. Its lift-producing component is obtained by multiplying by $\cos \psi$. It follows that the lift-producing vortex density per unit span is γ. The sectional lift coefficient is therefore

$$c_\ell = \frac{1}{\frac{1}{2} \rho V_\infty^2 \cdot 1} \rho V_\infty^2 \int_0^1 \gamma(\xi) d\xi$$

$$= 2 \int_0^{\pi} \frac{1}{2} \gamma(\theta) \sin \theta \, d\theta = \frac{\pi}{N} \sum_{k=1}^{N} \gamma_k \sin \theta_k \tag{48}$$

Similarly, the sectional pitching moment coefficient referred to the y-axis is

$$C_m = -\frac{2}{\bar{c}} \int_0^1 \gamma(\xi)(x_\ell + c\,\xi)\,d\xi = -\frac{\pi}{N\,\bar{c}} \sum_{k=1}^{N} \gamma_k \sin\theta_k\,(x_\ell + c\,\xi_k) \quad (49)$$

where ξ_k was given in Eq. (37). The sectional drag coefficient is

$$c_{d_i} = c_\ell \cdot \alpha - \overline{c_t} \quad (50)$$

To compute the total thrust coefficient, it is assumed that the predicted c_t represents the local value, instead of the average strip property. The total value will be computed by integration:

$$T = \int_{-b/2}^{b/2} c_t \cdot c \cdot q_\alpha\,dy = q_\infty \int_0^\pi c_t \cdot c \cdot \frac{b}{2}\sin\phi\,d\phi = \frac{b}{2}\,q_\infty \frac{\pi}{M} \sum_{i=1}^{M-1} c_{t_i}\,c_i\,\sin\phi_i \quad (51)$$

where the integration has been reduced to a finite sum by the conventional trapezoidal rule and

$$\phi_i = \frac{i\pi}{M} \quad, \quad i = 1, 2, \cdots, M-1 \quad (52)$$

Note that in the conventional trapezoidal rule, the values of the integrand at both integration limits appear in the finite sum. In the present case, both values are zero, because $\sin\phi = 0$ at $\phi = 0$ and π. The values of ϕ_i in Eq. (52) coincide with the y-control locations given in Eq. (40). It follows that the total thrust coefficient is given by

$$C_T = \frac{T}{q_\infty S_w} = \frac{b}{2\,S_w} \frac{\pi}{M} \sum_{i=1}^{M-1} c_{t_i}\,c_i\,\sin\phi_i \quad (53)$$

C.22

Similarly, the total lift and pitching moment coefficients are

$$C_L = \frac{b}{2 S_w} \frac{\pi}{M} \sum_{i=1}^{M-1} c_{\ell_i} c_i \sin\phi_i \qquad (54)$$

$$C_{m(1)} = \frac{b}{2 S_w} \frac{\pi}{M} \sum_{i=1}^{M-1} c_{m_i} c_i \sin\phi_i \qquad (55)$$

To check the accuracy of the above formulation, four planforms were chosen. The convergence of solutions for the rectangular planform of aspect ratio 2 is illustrated in Fig. 3. It can be seen that results with 3-digit accuracy can be easily obtained with the present method. Comparison of aerodynamic characteristics predicted by some analytical methods is made in Table 2. The values of $C_{L\alpha}$ and $C_{m\alpha}$ given by the $------$ $>$

Table 2   Comparison of Aerodynamic Characteristics
of Rectangular Wing of A = 2 by Different Methods at $M_\infty = 0$

	C_{L_α}, rad^{-1}	C_{m_α}, rad^{-1}	C_{Dii}/C_L^2 (Near Field)
Present $N_c = 6$, $N_s = 15$	2.4751	−0.5185	0.1591
Present $N_c = 5$, $N_s = 20$	2.4744	−0.5185	0.1589
VLM $N_c = 6$, $N_s = 20$ (Ref.32)	2.5239	−0.5334	0.1554
NLR Method (Ref.37)	2.4744	−0.5182	0.1609

Note: N_c = chordwise number of vortices. N_s = number of spanwise vortex strips. $1/(\pi A) = 0.15915$.
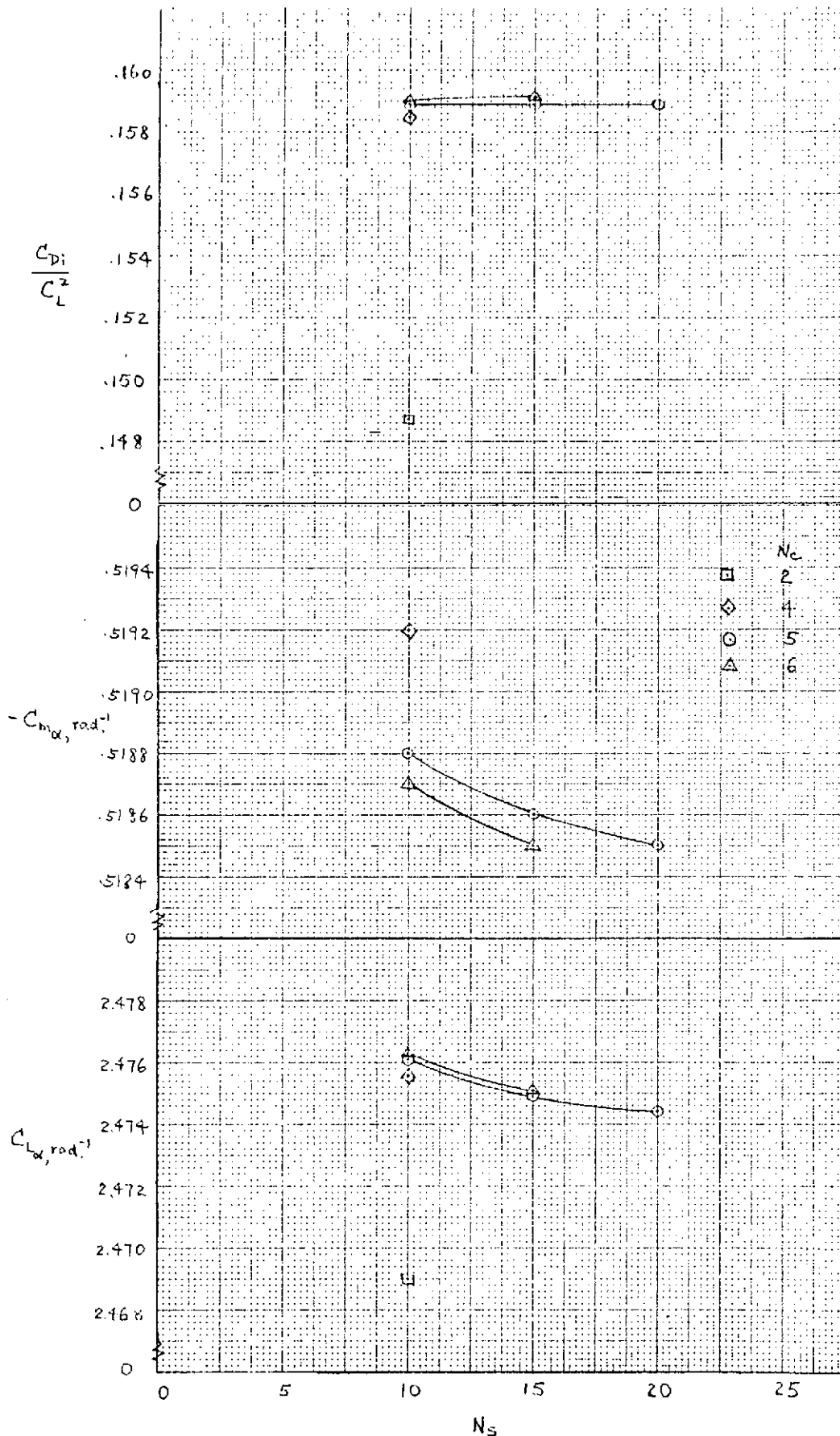
Figure 3. Effect of Vortex Arrangement on Computed Aerodynamic
Characteristics of Rectangular Wing of A=2 at $M_\infty = 0$

NLR method are regarded to be reliable, because the methods of BAC
and NPL produced the same values [37]. It is seen from Table 2 that
the present method gives more accurate results than the conventional
VLM.

The second planform is the Warren 12 planform which was also
evaluated in Ref.[37] (see Table 10 of this reference). Table 3 shows
the results. Again, the present method seems to give results closer

Table 3   Comparison of Aerodynamic Characteristics
of Warren 12 planform of A = $2\sqrt{2}$ by Different
Methods at $M_\infty = 0$

	C_{L_α} , rad^{-1}	C_{m_α} ,rad^{-1}	C_{Dii}/C_L^2 (Near Field)
Present $N_c = 5$, $N_s = 10$	2.7515	-3.0936	
Present $N_c = 5$, $N_s = 15$	2.7468	-3.0898	
VLM $N_c = 5$, $N_s = 15$ (Ref.32)	2.7944	-3.1775	0.1055
NLR Method (m = 15) (Ref.37)	2.7373	-3.1074	0.1201
NLR Method (m = 31) (Ref.37)	2.7576	-3.1155	0.1135
NPL Method (m = 15) (Ref.37)	2.7270	-3.1038	0.1227

Note: m = number of collocation sections over the whole wing.

$1/(\pi A) = 0.1125$

to those given by the NLR method.

Another low aspect-ratio planform evaluated is the 45°-sweep constant-chord wing of A = 2. This planform has also been investigated in Ref.32. The characteristics of solution convergence are illustrated in Table 4.

Table 4   Aerodynamic Characteristics of 45°-sweep
Constant-Chord Wing of A = 2 at $M_\infty = 0$. $N_c = 4$

Present Method					VLM (Ref.32)
N_s	10	15	20	25	25
C_{L_α}, rad^{-1}	2.2658	2.2604	2.2583	2.2573	2.2924
C_{m_α}, rad^{-1}	−1.5136	−1.5106	−1.5096	−1.5090	−1.5468
C_{Dii}/C_L^2 (Near Field)	0.1525	0.1556	0.1573	0.1583	0.1520

Note: $1/(\pi A) = 0.15915$

Again, 3-digit accuracy for C_{L_α} and C_{m_α} is easily attained. However, the convergence of the near-field C_{Dii}/C_L^2 seems to be slower than the other planforms evaluated.

To assess the accuracy of the method for high aspect-ratio wings, the rectangular wing of A = 7 is chosen. The aerodynamic characteristics of such a wing are shown in Table 5. It is seen that the results change little when the number of strips is increased from 10 to 15 with $N_c = 5$.

Table 5   Aerodynamic Characteristics of

Rectangular Wing of $A = 7$ at $M_\infty = 0$. $N_c = 5$

	Present Method		VLM (Ref.32)
N_s	10	15	15
C_{L_α}, rad $^{-1}$	4.4235	4.4215	4.5103
C_{m_α}, rad $^{-1}$	-1.0647	-1.0642	-1.0888
C_{Di}/C_L^2 (Near Field)	0.04647	0.04646	0.045

Note: $1/(\pi A) = 0.0455$

From the above evaluation, it may be concluded that the present method seems to yield consistently the results accurate to 3 digits for C_{L_α} and C_{m_α} , within the range of number of strips used in the investigation. For low aspect-ratio wings, in particular with sweep, the convergence characteristics for the near-field C_{Di}/C_L^2 with respect to the number of elements have been improved over the conventional VLM. However, higher accuracy seems not easy to attain with reasonable number of elements. It is thought that this may be due to the highly three-dimensional nature of the flow field associated with swept low aspect-ratio wings, so that the assumption of constant vortex strength over a strip is less applicable.

In order to treat complex planforms, such as variable-sweep wings, and wings with rapid variation in section properties, such as wings immersed in propeller slipstreams, it is convenient to introduce the following scheme of spanwise vortex strip distribution. Any spanwise interval on a semi-span may be divided into vortex strips by the semi-circle method described above. This has the advantage that the region of rapid variation of section properties can be covered with finer vortex strips. This is illustrated in Figure 4. Gaps between spanwise sections resulted from this procedure must be eliminated.
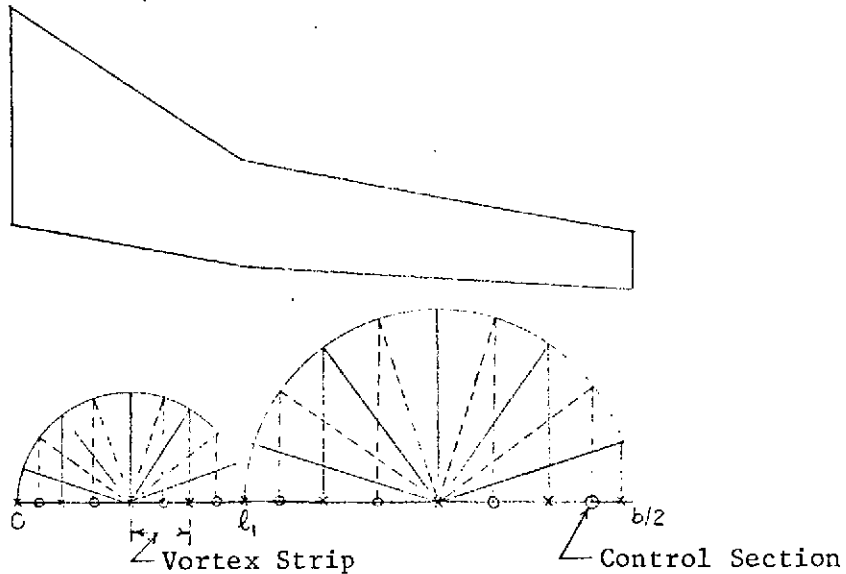
Figure 4.   Second Scheme of Spanwise Vortex Strip Distribution

Any interval can be transformed into $[o, \pi]$ on the ϕ-plane. For example, any station y in the interval $[\ell_1, \frac{b}{2}]$ can be expressed in terms of ϕ through the relation:

$$y = \frac{b/2 + \ell_1}{2} - \frac{b/2 - \ell_1}{2} \cos \phi \qquad (56)$$

Thus $[\ell_1, \frac{b}{2}]$ is transformed into $[o, \pi]$.   Let the vortex strips be

chosen so that

$$\frac{Y_j - \ell_1}{b/2 - \ell_1} = \frac{1}{2}\left[1 - \cos\left(\frac{2j-1}{2M_2}\pi\right)\right], \quad j = 1, \cdots, M_2 \qquad (57)$$

and the control points given by

$$\frac{Y_i - \ell_1}{b/2 - \ell_1} = \frac{1}{2}\left[1 - \cos\frac{i\pi}{M_2}\right], \quad i = 1, \cdots, M_2 - 1 \qquad (58)$$

Similar consideration is also applicable to the interval $[0, \ell_1]$ with M_2 replaced by M_1. It follows that the total lift coefficient can be computed as follows:

$$C_L = \frac{1}{S_w}\int_{-b/2}^{b/2} c_\ell c \, dy = \frac{2}{S_w}\left\{\int_0^{\ell_1} c_\ell c \, dy + \int_{\ell_1}^{b/2} c_\ell c \, dy\right\}$$

$$= \frac{2}{S_w}\left\{\frac{\ell_1}{2}\int_i^\pi c_\ell c \sin\phi \, d\phi + \frac{b/2 - \ell_1}{2}\int_0^\pi c_\ell c \sin\phi \, d\phi\right\}$$

$$= \frac{2}{S_w}\left\{\frac{\ell_1}{2}\frac{\pi}{M_1}\sum_{i=1}^{M_1-1} c_{\ell_i} c_i \sin\phi_i + \frac{b/2 - \ell_1}{2}\frac{\pi}{M_2}\sum_{i=1}^{M_2-1} c_{\ell_i} c_i \sin\phi_i\right\} \qquad (59)$$

The total pitching moment coefficient C_m and the total thrust coefficient C_T can be found in a similar manner.

In the thin wing theory, the convergence of solutions is indicated by the agreement of the near-field and the far-dield induced drags. The far-field induced drag is given by [Eq.143 of (38)]:

$$C_{D_i} = \frac{1}{S_w}\int_{-b/2}^{b/2} c_\ell c \, \alpha_i \, dy \qquad (60)$$

C.29

where α_i is the induced angle of attack given by [Eq. 61 of (38)]

$$\alpha_i = - \frac{1}{8\pi} \int_{-b/2}^{b/2} \frac{c_\ell c}{(y-y')^2} \, dy' \tag{61}$$

Let

$$y' = \frac{b}{2} \eta' \quad , \quad \eta' = -\cos\phi' \tag{62}$$

Eq. (61) becomes

$$\alpha_i = - \frac{1}{8\pi} \frac{2}{b} \int_{-1}^{+1} \frac{c_\ell c \, d\eta'}{(\eta - \eta')^2} \tag{63}$$

To integrate Eq. (63), Multhopp's interpolation formula is used for $c_\ell c$ [38].
Thus,

$$c_\ell c = \frac{2}{M} \sum_{n=1}^{M-1} (c_\ell c)_n \sum_{\lambda=1}^{M-1} \sin\lambda\phi_n \sin\lambda\phi \tag{64}$$

where M-1 is the number of interpolation stations over the whole span,
and

$$\phi_n = \frac{n\pi}{M} \quad , \quad n = 1, \cdots, M-1 \tag{65}$$

Substituting Eq. (64) into Eq. (63), it is obtained that

$$\alpha_i = - \frac{1}{4\pi b} \frac{2}{M} \sum_{n=1}^{M-1} (c_\ell c)_n \sum_{\lambda=1}^{M-1} \sin\lambda\phi_n \int_0^\pi \frac{\sin\lambda\phi' \sin\phi' \, d\phi'}{(\cos\phi' - \cos\phi)^2}$$

$$= \frac{1}{2bM} \sum_{n=1}^{M-1} \frac{(c_\ell c)_n}{\sin\phi} \sum_{\lambda=1}^{M-1} \lambda \sin\lambda\phi_n \sin\lambda\phi \tag{66}$$

where the following relation

$$\int_0^\pi \frac{\sin\lambda\phi' \sin\phi' \, d\phi'}{(\cos\phi' - \cos\phi)^2} = -\lambda\pi \frac{\sin\lambda\phi}{\sin\phi} \tag{67}$$

has been used (Appendix IV of Ref.(38)). Now, choose ϕ such that

$$\phi_\nu = \frac{\nu \pi}{M} , \qquad \nu = 1, \cdots , M-1 \qquad (68)$$

It follows that (Appendix IV of Ref.(38))

$$b_{n\nu} = \frac{4}{M \sin \phi_\nu} \sum_{\lambda=1}^{M-1} \lambda \sin \lambda \phi_n \sin \lambda \phi_\nu = \frac{(-1)^{n-\nu}-1}{M} \frac{2 \sin \phi_n}{(\cos \phi_n - \cos \phi_\nu)^2} , \; n \neq \nu \qquad (69a)$$

$$= \frac{M}{\sin \phi_\nu} , \quad n = \nu \qquad (69b)$$

Eq.(66) becomes finally

$$(\alpha_i)_\nu = \frac{1}{8b} \sum_{n=1}^{M-1} (c_\ell c)_n b_{n\nu} \qquad (70)$$

Once α_i's are obtained from Eq.(70), Eq.(60) can be integrated for the induced drag, following the scheme of Eq.(53). Thus,

$$C_{D_i} = \frac{b}{2 S_w} \frac{\pi}{M} \sum_{i=1}^{M-1} (c_\ell c \alpha_i)_i \sin \phi_i \qquad (71)$$

where ϕ_i is given by Eq.(68) with ν replaced by i.

In Eq.(70), c_ℓ's and c's at stations specified by Eq.(65) are required. However, only those at stations given by Eq.(58) are known. Therefore, some interpolation procedure must be used. In the present method, the following Lagrange interpolation formula was used:

$$c_\ell = \frac{(y-y_2)(y-y_3)\cdots(y-y_n)}{(y_1-y_2)(y_1-y_3)\cdots(y_1-y_n)} c_{\ell_1} + \frac{(y-y_1)(y-y_3)\cdots(y-y_n)}{(y_2-y_1)(y_2-y_3)\cdots(y_2-y_n)} c_{\ell_2} +$$

$$- - - - - - - \qquad (72)$$

with similar formula for the local chord c.

In the following illustration of some computed results, M is taken to be 31, except for the variable-sweep wing where M = 41. It

is assumed that the convergence of solutions is achieved if the near-field induced drag differs from the far-field value by less than 1%. The rectangular wing of A = 2 is again employed to make the comparison. This is illustrated in Table 6. The second planform chosen for comparison is that of a delta wing of A = 2 at M_∞ = 0.13. The comparison is made in Table 7 with experimental results and other analytical methods. It should be noted that the vortex arrangement for the VLM is judged, from the study made in Ref.(32), to be the best for a total of 120 vortices. The near-field induced drag parameter by the VLM is 3.45% too low. The present results are comparable in accuracy with Wagner's method. However, Wagner's program requires large ammount of processing time, being about 8 times higher than the present method (71.6 sec. in the Honeywell 635) for this configuration.

The third planform is the sweptback and tapered planform of A = 8.02 given in Ref.(39). The geometry is given in Fig. 5. The results are
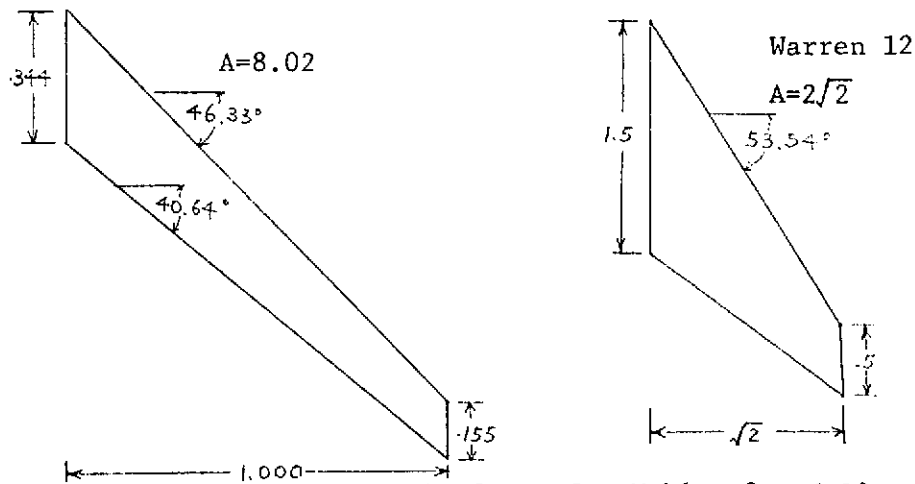
Figure 5. Geometry of Planforms for Tables 8 and 10.

shown in Table 8. Additional results for other planforms are compared in Tables 9, 10 and 11. In all cases, reasonably good results are always

obtained by the present method. One important feature of the present computer program is that Purchell's method [21] has been used for solving the matrix equation, instead of the standard matrix inversion method. This requires only 17K (decimal) memory and 95.8 sec. for execution in the Honeywell 635 for a total of 120 vortices, compared with 26K (decimal) memory with overlays and 350 sec. processing time for the VLM of Ref. 32. A fraction of the latter processing time may be due to the computation of additional quantities, such as the side-wash, etc.

The spanwise distribution of the sectional lift coefficient and the sectional induced drag coefficient is illustrated in Fig. 6 for the variable-sweep wing.

Table 6. Aerodynamic Characteristics of a
Rectangular Wing of A = 2 at $M_\infty = 0$

Method	$C_{L_\alpha}, \text{rad}^{-1}$	$C_{m_\alpha}, \text{rad}^{-1}$	$C_{D_{ii}}/C_L^2$	$C_{D_{ii}}/C_{D_i}$
Present $N_c=8, N_s=15$	2.4707	-0.5173	0.1595	0.9972
VLM $N_c=6, N_s=20$ (Ref.32)	2.5239	-0.5334	0.1554	0.9747
NLR (Ref.37)	2.4744	-0.5182	0.1609	1.0101
Wagner (Ref.40)	2.4778	-0.5180	0.1619	1.0167

Table 7. Aerodynamic Characteristics of a
Delta Wing of A = 2 at $M_\infty = 0.13$ and $\alpha = 4.3°$

Method	C_L	a.c.*	$C_{D_{ii}}/C_L^2$	$C_{D_{ii}}/C_{D_i}$
Present $N_c=3, N_s=35$	0.1649	0.3767	0.1625	1.0078
Lamar (Ref.39)	0.168	0.363		
VLM $N_c=6, N_s=20$ ($M_\infty = 0.1$) (Ref.32)	0.1654	0.3823	0.1549	0.9655
Wagner (Ref.40)	0.1663	0.3783	0.1576	0.9795
Experiment (Ref.39)	0.159	0.396		

*measured from the leading edge of the mean geometric chord as defined
in Ref. 39 and referenced to the mean geometric chord.

<div align="center">

Table 8. Aerodynamic Characteristics of a Sweptback and
Tapered Wing of A = 8.02 at M_∞ = 0.19 and α = 4.7°

</div>

Method	C_L	a.c.*	$C_{D_{ii}}/C_L^2$	$C_{D_{ii}}/C_{D_i}$
Present $N_c=4, N_s=25$	0.3074	0.3253	0.04235	1.014
Lamar (Ref.39)	0.312	0.317		
VLM $N_c=4, N_s=30$	0.3105	0.3365	0.03951	0.9356
Experiment (Ref.39)	0.315	0.328		

*See the footnote in Table 7.

<div align="center">

Table 9. Aerodynamic Characteristics of a
Rectangular Wing of A = 7 at M_∞ = 0.0

</div>

Method	C_{L_α}, rad^{-1}	C_{m_α}, rad^{-1}	$C_{D_{ii}}/C_L^2$	$C_{D_{ii}}/C_{D_i}$
Present $N_c=5, N_s=15$	4.4142	-1.0624	0.04658	0.9972
VLM $N_c=5, N_s=15$ (Ref.32)	4.5103	-1.0888	0.0450	0.9597
Wagner (Ref.40)	4.4300	-1.0680	0.04888	1.05159
Lamar (Ref.39)	4.40	-1.047		

Table 10. Aerodynamic Characteristics of
Warren 12 Planform of $\Lambda = 2\sqrt{2}$ at $M_\infty = 0$

Method	C_{L_α}, rad^{-1}	C_{m_α}, rad^{-1}	$C_{D_{ii}}/C_L^2$	$C_{D_{ii}}/C_{D_i}$
Present $N_c=5, N_s=20$	2.7382	−3.0844	0.11428	1.0054
VLM $N_c=5, N_s=15$ (Ref.32)	2.7944	−3.1775	0.1055	0.9275
NLR (m = 15) (Ref.37)	2.7373	−3.1074	0.1201	1.0564
NLR (m = 31) (Ref.37)	2.7576	−3.1155	0.1135	0.9921

Table 11. Aerodynamic Characteristics of a
Variable-Sweep Wing of $A = 4.303$ at $M_\infty = 0.23$

Method	C_{L_α}, rad^{-1}	a.c.[*]	$C_{D_{ii}}/C_L^2$	$C_{D_{ii}}/C_{D_i}$
Present $N_c=4, N_s=28$	3.0070	−0.1378	0.0760	0.9989
VLM $N_c=5, N_s=32$ (Ref.27)	3.02485		0.07465	0.9815
Wagner (Ref.40)	2.844		0.075	1.0
Lamar (Ref.39)	3.057	−0.175		
Experiment (Ref.39)	2.75	−0.106		

[*]See the footnote in Table 7.
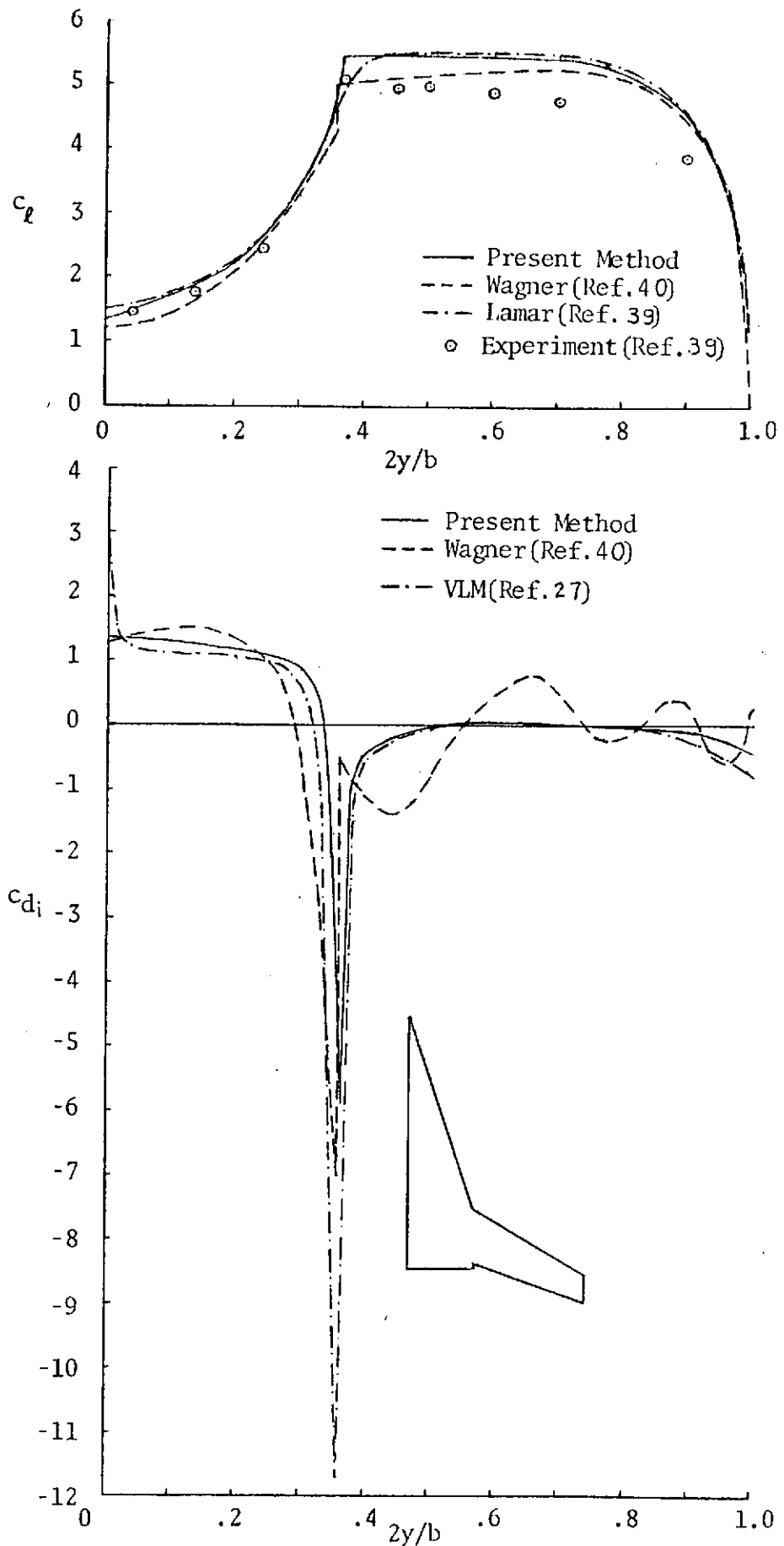
Figure 6. Comparison of Aerodynamic Characteristics for a Variable-
Sweep Wing of A=4.303 at M = 0.23

APPENDIX D

Expressions for $\vec{M}_\ell$ and $\vec{G}_\ell$

1. Wing-Slipstream Interaction

According to Eq.(4.33), $\vec{M}_\ell$ is given by

$$\vec{M}_\ell = \frac{\vec{a} \times \vec{\ell}}{|\vec{a}' \times \vec{\ell}'|^2} \left\{ \frac{\vec{b}' \cdot \vec{\ell}'}{|\vec{b}'|} - \frac{\vec{a}' \cdot \vec{\ell}'}{|\vec{a}'|} \right\} \qquad (1)$$

The circumference of the circular slipstream is divided into a number of equal straight line segments, so that the circular slipstream is approximated by an inscribed polygon. The control points (x, y, z) are chosen at the midpoints of the elements. In terms of the cylindrical polar coordinate system, as shown in Figure 1, the endpoints of any element, (x_1, y_1, z_1) and (x_2, y_2, z_2), can be expressed as follows:

$$
\begin{aligned}
x_1 &= x_s \\
y_1 &= y_s + r\cos\phi_1 \\
z_1 &= z_s + r\sin\phi_1
\end{aligned}
\qquad (2a)
$$

$$
\begin{aligned}
x_2 &= x_s \\
y_2 &= y_s + r\cos\phi_2 \\
z_2 &= z_s + r\sin\phi_2
\end{aligned}
\qquad (2b)
$$

where (x_s, y_s, z_s) is the center of the circular slipstream at the section under consideration. With the geometry of the vortex elements defined, the various terms in Eq.(1) can be computed in the rectangular coordinate system as follows:

$$\vec{a} \times \vec{\ell} = \hat{i}\left[(y_1 - y)(z_2 - z_1) - (z_1 - z)(y_2 - y_1)\right] - \hat{j}\left[(x_1 - x)(z_2 - z_1)\right.$$

$$\left. - (z_1 - z)(x_2 - x_1)\right] + \hat{k}\left[(x_1 - x)(y_2 - y_1) - (y_1 - y)(x_2 - x_1)\right] \tag{3a}$$

$$|\vec{a} \times \vec{\ell}'|^2 = \beta^2 \left\{ \left[(x_2 - x_1)(y_1 - y) - (x_1 - x)(y_2 - y_1)\right]^2 + \left[(x_2 - x_1)(z_1 - z)\right.\right.$$

$$\left.\left. - (x_1 - x)(z_2 - z_1)\right]^2 + \beta^2\left[(y_2 - y_1)(z_1 - z) - (z_2 - z_1)(y_1 - y)\right]^2 \right\} \tag{3b}$$

$$\vec{b}' \cdot \vec{\ell}' = (x_2 - x)(x_2 - x_1) + \beta^2(y_2 - y)(y_2 - y_1) + \beta^2(z_2 - z)(z_2 - z_1) \tag{3c}$$

$$\vec{a}' \cdot \vec{\ell}' = (x_1 - x)(x_2 - x_1) + \beta^2(y_1 - y)(y_2 - y_1) + \beta^2(z_1 - z)(z_2 - z_1) \tag{3d}$$

$$|\vec{b}'| = \left[(x_2 - x)^2 + \beta^2(y_2 - y)^2 + \beta^2(z_2 - z)^2\right]^{1/2} \tag{3e}$$

$$|\vec{a}'| = \left[(x_1 - x)^2 + \beta^2(y_1 - y)^2 + \beta^2(z_1 - z)^2\right]^{1/2} \tag{3f}$$
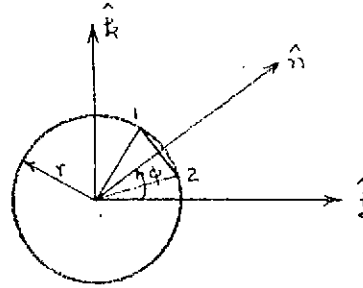
Figure 1. Jet Polar Coordinate System

According the Figure 1, the unit normal vector is

$$\hat{n} = \hat{j}\cos\phi + \hat{k}\sin\phi \tag{4}$$

It follows that

$$\vec{M}_\ell \cdot \hat{n} = \left\{ -\left[(x_1 - x)(z_2 - z_1) - (z_1 - z)(x_2 - x_1)\right]\cos\phi + \left[(x_1 - x)(y_2 - y_1) - \right.\right.$$

$$\left.\left. - (y_1 - y)(x_2 - x_1)\right]\sin\phi\right\}\left\{ \frac{\vec{b}' \cdot \vec{\ell}'}{|\vec{b}'|} - \frac{\vec{a}' \cdot \vec{\ell}'}{|\vec{a}'|} \right\} \Big/ |\vec{a}' \times \vec{\ell}'|^2 \tag{5}$$

In the present linear theory, the slipstream axis is assumed to lie along the x-axis. Therefore, $\hat{e}_s = \hat{i}$. It follows that

$$\vec{M}_2 \cdot \hat{e}_s = \frac{(y_1 - y)(z_2 - z_1) - (x_1 - x)(y_2 - y_1)}{|\vec{a}' \times \vec{x}'|^2} \left\{ \frac{\vec{b}' \cdot \vec{\ell}'}{|\vec{b}'|} - \frac{\vec{a}' \cdot \vec{\ell}'}{|\vec{a}'|} \right\} \tag{6}$$

To evaluate $\vec{G}_\ell$, it is assumed that the trailing vortices are straight lines along the x-dirction. It follows from Eq.(4.34) that, for trailing vortices emanating from the second endpoints,

$$\vec{G}_{\ell(2)} = \int_2 \frac{(\vec{R}_1 - \vec{R}) \times d\vec{\ell}}{R_\beta^3}$$

$$= \hat{i} \int_2 \frac{(y' - y)\,dz' - (z' - z)\,dy'}{R_\beta^3} + \hat{j} \int_2 \frac{(z' - z)\,dx' - (x' - x)\,dz'}{R_\beta^3}$$

$$+ \hat{k} \int_2 \frac{(x' - x)\,dy' - (y' - y)\,dx'}{R_\beta^3}$$

$$= \hat{j}\,(z_2 - z) \int_2 \frac{dx'}{R_\beta^3} - \hat{k}\,(y_2 - y) \int_2 \frac{dx'}{R_\beta^3} \tag{7}$$

where it has been assumed that each trailing vortex line is parallel to the x-axis at a constant y. The integral in the last expression can be integrated as follows:

$$\int_2 \frac{dx'}{R_\beta^3} = \int_2^\infty \frac{dx'}{\left[(x - x')^2 + \beta^2(y - y_2)^2 + \beta^2(z - z_2)^2\right]^{3/2}}$$

$$= \frac{1}{\beta^2\left[(y - y_2)^2 + (z - z_2)^2\right]} \left\{ 1 - \frac{x_2 - x}{\left[(x - x_2)^2 + \beta^2(y - y_2)^2 + \beta^2(z - z_2)^2\right]^{1/2}} \right\} \tag{8}$$

Hence,

$$\vec{G}_{\ell(2)} = \hat{j}\, \frac{z_2 - z}{\beta^2\left[(y-y_2)^2 + (z-z_2)^2\right]}\left\{1 - \frac{x_2 - x}{\left[(x-x_2)^2 + \beta^2(y-y_2)^2 + \beta^2(z-z_2)^2\right]^{1/2}}\right\}$$

$$-\hat{k}\, \frac{y_2 - y}{\beta^2\left[(y-y_2)^2 + (z-z_2)^2\right]}\left\{1 - \frac{x_2 - x}{\left[(x-x_2)^2 + \beta^2(y-y_2)^2 + \beta^2(z-z_2)^2\right]^{1/2}}\right\} \tag{9}$$

For trailing vortices from the first endpoints, it should be noted that $d\vec{\ell}_1 = -d\vec{\ell}_2$. It follows that Eq.(9) is still applicable in this case except that the subscript 2 is to be replaced by 1 and there is a sign change.

$$\vec{G}_{\ell(1)} = -\hat{j}\, \frac{z_1 - z}{\beta^2\left[(y-y_1)^2 + (z-z_1)^2\right]}\left\{1 - \frac{x_1 - x}{\left[(x-x_1)^2 + \beta^2(y-y_1)^2 + \beta^2(z-z_1)^2\right]^{1/2}}\right\}$$

$$+\hat{k}\, \frac{y_1 - y}{\beta^2\left[(y-y_1)^2 + (z-z_1)^2\right]}\left\{1 - \frac{x_1 - x}{\left[(x-x_1)^2 + \beta^2(y-y_1)^2 + \beta^2(z-z_1)^2\right]^{1/2}}\right\} \tag{10}$$

Adding Eq.(9) and (10) gives the final results for $\vec{G}_\ell$:

$$\vec{G}_\ell = \vec{G}_{\ell(1)} + \vec{G}_{\ell(2)} \tag{11}$$

$\vec{G}_\ell \cdot \hat{n}$ and $\vec{G}_\ell \cdot \hat{e}_s$ can be obtained by simply taking dot products of (11) with Eq.(4) and $\hat{i}$, respectively. Since $\hat{e}_s = \hat{i}$, obviously $\vec{G}_\ell \cdot \hat{e}_s = 0$.

To evaluate the downwash on the wing surface, note that $\hat{n}_w = \hat{k}$.

Hence,

$$\vec{M}_\ell \cdot \hat{n}_w = \frac{(x_1-x)(y_2-y_1)-(y_1-y)(x_2-x_1)}{|\vec{a}' \times \vec{\ell}'|^2}\left\{\frac{\vec{b}' \cdot \vec{\ell}'}{|\vec{b}'|} - \frac{\vec{a}' \cdot \vec{\ell}'}{|\vec{a}'|}\right\} \tag{12}$$

$$\vec{G}_\ell \cdot \hat{n}_w = -\frac{y_2 - y}{\beta^2\left[(y-y_2)^2 + (z-z_2)^2\right]}\left\{1 - \frac{x_2 - x}{\left[(x-x_2)^2 + \beta^2(y-y_2)^2 + \beta^2(z-z_2)^2\right]^{1/2}}\right\}$$

$$+\frac{y_1 - y}{\beta^2\left[(y-y_1)^2 + (z-z_1)^2\right]}\left\{1 - \frac{x_1 - x}{\left[(x-x_1)^2 + \beta^2(y-y_1)^2 + \beta^2(z-z_1)^2\right]^{1/2}}\right\} \tag{13}$$

D.4

2. Upper Surface Blowing Jet-Wing Interaction

Eqs.(12) and (13) are still applicable in this application, because the jet has been assumed to be flat with constant thickness. However, for a rectangular jet with the control points on the sidewalls, $\hat{n}$ would be $\hat{j}$ on the outboard sidewall and $-\hat{j}$ on the inboard sidewall. It follows that on the sidewalls

$$\vec{M}_\ell \cdot \hat{n} = \mp \frac{(x_1-x)(z_2-z_1)-(z_1-z)(x_2-x_1)}{|\vec{a}' \times \hat{\ell}'|^2} \left\{ \frac{\vec{b}' \cdot \vec{\ell}'}{|\vec{b}'|} - \frac{\vec{a}' \cdot \vec{\ell}'}{|\vec{a}'|} \right\} \tag{14}$$

$$\vec{G}_\ell \cdot \hat{n} = \pm \frac{z_2-z}{\beta^2[(y-y_2)^2+(z-z_2)^2]} \left\{ 1 - \frac{x_2-x}{[(x-x_2)^2+\beta^2(y-y_2)^2+\beta^2(z-z_2)^2]^{1/2}} \right\}$$

$$\mp \frac{z_1-z}{\beta^2[(y-y_1)^2+(z-z_1)^2]} \left\{ 1 - \frac{x_1-x}{[(x-x_1)^2+\beta^2(y-y_1)^2+\beta^2(z-z_1)^2]^{1/2}} \right\} \tag{15}$$

where the upper sign is for the outboard sidewall. $\vec{M}_\ell \cdot \hat{e}_s$ is still given by Eq.(6) and $\vec{G}_\ell \cdot \hat{e}_s = 0$.

APPENDIX E

Numerical Accuracy for Evaluating
the u-Induced Velocity

According to Eq. (6.28), the u-induced velocity due to a particular strip of vortex distribution can be accurately evaluated by rewriting the expression as

$$\Delta u = \frac{\beta^2}{4\pi} \int_{x_\ell}^{x_t} [\gamma(x') - \gamma(x)] \vec{M}_\ell \cdot \hat{\imath} \, dx' + \frac{\beta^2 \gamma(x)}{4\pi} \int_{x_\ell}^{x_t} \vec{M}_\ell \cdot \hat{\imath} \, dx' \qquad (1)$$

There is no difficulty in evaluating the first integral numerically because the integrand is at most Cauchy singular. In the present computer program, the second integral is approximated by a finite sum as follows by setting $x' = x_\ell + c(1 - \cos\theta')/2$:

$$F(x, z) = \frac{\beta^2}{4\pi} \int_{x_\ell}^{x_t} \vec{M}_\ell \cdot \hat{\imath} \, dx' \cong \frac{\beta^2}{8} c \frac{1}{N} \sum_{k=1}^{N} \vec{M}_\ell \cdot \hat{\imath} \, \sin\theta_k \qquad (2)$$

To check the accuracy of Eq. (2), consider a rectangular wing with unit chord length. In this case, the bound vortex is unswept so that $x_1 = x_2 = x'$. According to Appendix D, it can be shown that

$$M_u = \vec{M}_\ell \cdot \hat{\imath} = \frac{z \Delta y}{|\vec{a}' \times \vec{\ell}'|^2} \left\{ \frac{\beta^2(y_2 - y)\Delta y}{[(x_2 - x)^2 + \beta^2(y_2 - y)^2 + \beta^2 z^2]^{1/2}} \right.$$

$$\left. - \frac{\beta^2(y_1 - y)\Delta y}{[(x_1 - x)^2 + \beta^2(y_1 - y)^2 + \beta^2 z^2]^{1/2}} \right\}$$

$$|\vec{a}' \times \vec{\ell}'|^2 = \beta^2 \left\{ (x_1 - x)^2 (\Delta y)^2 + \beta^2 (\Delta y)^2 z^2 \right\}$$

$$\Delta y = y_2 - y_1$$

It follows that

$$F(x,z) = \frac{\beta^2}{4\pi} \int_0^1 \vec{M}_\ell \cdot \hat{\imath}\, dx_1 + \frac{\beta^2 z}{4\pi} \int_0^1 \frac{1}{(x'-x)^2+\beta^2 z^2} \left\{ \frac{y_2-y}{\left[(x'-x)^2+\beta^2(y_2-y)^2+\beta^2 z^2\right]^{1/2}} \right.$$

$$\left. - \frac{y_1-y}{\left[(x'-x)^2+\beta^2(y_1-y)^2+\beta^2 z^2\right]^{1/2}} \right\} dx'$$

$$= \frac{1}{4\pi} \left\{ \frac{\beta^2 z\,(y_2-y)}{\beta z\,[\beta^2(y_2-y)^2]^{1/2}}\, \tan^{-1} \frac{(x'-x)|y_2-y|}{z\left[(x'-x)^2+\beta^2(y_2-y)^2+\beta^2 z^2\right]^{1/2}} \Bigg|_0^1 \right.$$

$$\left. - \frac{\beta^2 z\,(y_1-y)}{\beta z\,[\beta^2(y_1-y)^2]^{1/2}}\, \tan^{-1} \frac{(x'-x)|y_1-y|}{z\left[(x'-x)^2+\beta^2(y_1-y)^2+\beta^2 z^2\right]^{1/2}} \Bigg|_0^1 \right\}$$

$$= \frac{1}{4\pi} \left\{ \tan^{-1} \frac{(1-x)(y_2-y)}{z\left[(1-x)^2+\beta^2(y_2-y)^2+\beta^2 z^2\right]^{1/2}} + \tan^{-1} \frac{x(y_2-y)}{z\left[x^2+\beta^2(y_2-y)^2+\beta^2 z^2\right]^{1/2}} \right.$$

$$\left. + \tan^{-1} \frac{(1-x)(y_1-y)}{z\left[(1-x)^2+\beta^2(y_1-y)^2+\beta^2 z^2\right]^{1/2}} + \tan^{-1} \frac{x(y_1-y)}{z\left[x^2+\beta^2(y_1-y)^2+\beta^2 z^2\right]^{1/2}} \right\}$$

$$\tag{3}$$

where the fact that $y_2 - y > 0$ and $y_1 - y < 0$ has been used. To check
the accuracy of the approximation by Eq.(2) against Eq.(3), let $y_1 = 1$,
$y_2 = 1.4$, $y = 1.2$ and $\beta = 1$. For 5 control points (i.e., M = 5) and
40 integration points (i.e., N = 40), the results are generated and
compared in Table 1. It is seen that the present interdigitated integra-
tion scheme is sufficiently accurate.

Table 1. Accuracy of Interdigitated Integration Scheme

$$y_1 = 1, \ y_2 = 1.4, \ y = 1.2, \ \beta = 1$$

x	z	F(x,z) by Eq.(2)	Exact F(x,z) by Eq.(3)
0.09549		0.21551	0.21543
0.34549		0.27348	0.27347
0.65451	0.15	0.27348	0.27347
0.90451		0.21551	0.21543
1.0		0.14537	0.14526
0.09549		0.37473	0.37465
0.34549		0.41389	0.41411
0.65451	0.05	0.41389	0.41411
0.90451		0.37473	0.37465
1.0		0.21062	0.21022
0.09549		0.43349	0.43452
0.34549		0.44171	0.45643
0.65451	0.025	0.44171	0.45643
0.90451		0.43349	0.43452
1.0		0.23063	0.22981

CRINC LABORATORIES

Chemical Engineering Low Temperature Laboratory

Remote Sensing Laboratory

Flight Research Laboratory

Chemical Engineering Heat Transfer Laboratory

Nuclear Engineering Laboratory

Environmental Health Engineering Laboratory

Information Processing Laboratory

Water Resources Institute

Technology Transfer Laboratory